A METHODOLOGY FOR TRIBOLOGICAL EXAMINATION OF THIN FILMS IN THE NANODISPLACEMENT REGIME

By

GERALD R. BOURNE

A DISSERTATION PRESENTED TO THE GRADUATE SCHOOL
OF THE UNIVERSITY OF FLORIDA IN PARTIAL FULFILLMENT
OF THE REQUIREMENTS FOR THE DEGREE OF
DOCTOR OF PHILOSOPHY

UNIVERSITY OF FLORIDA

2006

To Wanda and Gabrielle

ACKNOWLEDGMENTS

First and foremost, I would like to thank my wife, Wanda, for seeing this long journey to the end with unwavering support. Without her encouragement, I would not have embarked on this path, let alone seen it to completion.

I would like to thank Greg Sawyer for his advice and support. His dedication to his students and research is inspiring and unparalleled. Thanks to Carol Sawyer for putting up with Greg. Thanks to Amelia Dempere; I could not ask for a more understanding and flexible boss. Thanks to Mike Kaufman for showing me what fun hovering over a phosphorous screen for several hours could be. I appreciate Kevin Jones accepting a committee position at this late stage in the project. Thanks to Nam-Ho Kim for his contributions in finite element analysis.

I would like to thank Jeff Bardt for his contribution on many levels, from keeping me young with our juvenile banter and back and forth hijinks, to the extensive assistance with my computer incompetence. Thanks to Ben Boesl, Matt Hamilton, Pam Dickrell, Nicole McCook, Kerry Siebein, and Junghun Jang for contributions to and useful discussions about this project. Thanks to the students of the Tribology Lab for support and comic relief.

Thanks to the MAIC facility and its staff for use of the instruments, financial support, and discussions about techniques and analysis. Finally, I would like to thank the faculty at the Materials Science and Engineering Department of the University of Florida. As an undergraduate, I was inspired to pursue research in this field from the knowledge,

enthusiasm, and support from Richard Connell, Robert DeHoff, Mike Kaufman, and Fereshteh Ebrahimi.

TABLE OF CONTENTS

page

ACKNOWLEDGMENTS iv

LIST OF TABLES ix

LIST OF FIGURES x

ABSTRACT xv

CHAPTER

1 INTRODUCTION AND BACKGROUND 1

Introduction 1
Background 3
Early Friction Studies 4
Mechanism for Metallic Friction 5
Sliding Wear 7
Prow Formation 7
Delamination Theory 8
Subsurface Wear 9
Film Thickness Wear and Friction Dependence 9
Modeling 11

2 EXPERIMENTAL MATRIX 13

Sample Preparation 14
Bulk Gold Foil 15
Ion Beam Sputtered Gold on Silicon 16
Electron Beam Evaporated Gold on Silicon 19
Carbon Arc Evaporation 20
Ion Beam Etched Area of Interest 21

3 TEST EQUIPMENT 23

Hysitron Triboindenter 25
CSM Microtribometer 28

4 EXPERIMENTAL PROCEDURES 30

Hysitron Triboindenter Procedures....30
Tip Preparation....30
Sample Mounting....32
Electrostatic Force Constant and Zero Volt Gap Calibration....33
Tip Optics Offset Calibration....33
Standard tip optics offset procedure....33
Modified tip optics offset procedure....35
Quick Approach....43
Tip Area Function Calibration....43
Machine Compliance Calibration....44
Testing Modes....45
Depth sensing indentation....46
Rastering wear test....47
Reciprocating wear test....48
CSM Microtribometer....48
Tip Preparation....48
Sample Mounting....48
Reciprocating Wear Test....49

5 DATA ANALYSIS....50

Indentation Testing....50
Oliver-Pharr Method....50
Compliance Method (Stone's Method)....54
Modified Winkler Method....57
Rastering Wear Test....63
Triboindenter Reciprocating Wear Test....65
CSM Microtribometer....66

6 CHARACTERIZATION....67

Tip Characterization....67
Indentation Method....67
Scanning Method....68
Transmission Electron Microscopy Method....71
X-ray Diffraction....74
Crystallographic Texture....76
Grain Size....78
Scanning Electron Microscopy....79
Focused Ion Beam Milling....80
Transmission Electron Microscopy Sample Thinning....80
Slice and View Serial Sectioning....83
Fixed sample method....84
Rotated sample method....85
Transmission Electron Microscopy Analysis....87

7 RESULTS AND DISCUSSION....89

Static Indentation Testing 89
Oliver and Pharr Analysis Results 89
Stone Analysis Results 92
Modified Winkler Approach 95
Rastering Wear Tests 96
Reciprocating Wear Tests 99
Film Failure 99
Gold on silicon without carbon 101
Carbon on gold on silicon 103
Electron Microscopy Cross Sections of Wear Scars 105
Friction Measurements 110
Hysitron Triboindenter friction measurements 110
CSM microtribometer friction coefficient measurements 114

8 CONCLUSIONS 117

APPENDIX

A SCANNING ELECTRON MICROSCOPY IMAGES 119

B SCANNING ELECTRON MICROSCOPY CROSS SECTIONS 123

LIST OF REFERENCES 127

BIOGRAPHICAL SKETCH 131

LIST OF TABLES

Table page

1-1 Summary of studies of thin metallic films on substrates. 10

2-1 Sample naming designations. 14

7-1 Hardness values calculated for samples from the Hall-Petch equation. 92

7-2 Hardness values calculated for samples from the Stone method. 95

7-3 Results of SEM micrographs from gold on silicon samples with 100 μN normal load. 101

7-4 Results of SEM micrographs from gold on silicon samples with 500 μN normal load.. 102

7-5 Results of SEM micrographs from carbon on gold on silicon samples with 100 μN normal load. 104

7-6 Results of SEM micrographs from carbon on gold on silicon samples with 500 μN normal load. 104

LIST OF FIGURES

Figure page

1-1 Slider and areas from Equation 1-3. 6

1-2 Three slider geometries from Bowden and Tabor's experiment. 6

1-3 Effect of film thickness on friction coefficient of metallic film solid lubricants on harder substrates. 10

2-1 South Bay Technology 8" polishing wheel 16

2-2 Ion beam sputtering process 17

2-3 Gatan Model 681 High Resolution Ion Beam Coater 17

2-4 Electron beam evaporation process 19

2-5 Carbon arc evaporation 20

2-6 Rastering wear test 4 μm x 4 μm with low contact pressure. 21

2-7 Etched grid lines for wear test location 22

3-1 A typical pin-on-disc type tribometer 23

3-2 Linear reciprocating tribometer 24

3-3 Hysitron Triboindenter with upper thermal-acoustic isolation cover removed to show interior details. 25

3-4 Capacitive transducer assembly schematic 26

3-5 Enlarged view of Triboindenter components 27

3-6 CSM® Microtribometer. 28

4-1 Diamond indenter tip and assembly of a large radius sapphire tip 32

4-2 Optical CCD microscope image of H-pattern indents 34

4-3 Spherical indenter on flat surface and cross sectional geometry to solve for depth of indentation....35

4-4 Patterned modified tip optics offset sample....37

4-5 Modified tip optics offset sample centered in the video window....39

4-6 Single indent selected....39

4-7 Manual height adjustment window....40

4-8 Search option window....40

4-9 Imaging window and control panel with image of modified tip optics offset sample....41

4-10 Actual tip optics offset seen in the video window....42

4-11 Triboindenter testing modes....46

4-12 Rastering wear test showing fiducial indentation marks in circles....47

4-13 CSM® Microtribometer....48

5-1 Load versus displacement curve along with a cross section of an indented surface. The range of ε is indicated for various indenter geometries....51

5-2 Measured compliance versus square root of maximum load for a load range of 5mN to 10mN on quartz, Al (001), and Si (001)....55

5-3 Indent cross sections from Oliver-Pharr and Modified Winkler compared to an actual indent....58

5-3 Differential element described with cylindrical coordinates and tip displacement based on a spherical tip geometry....60

5-4 Differential element illustration prior to (left) and after load (right) with variable notation indicated....61

5-5 Loading code flow chart....62

5-6 Unloading code flow chart....63

5-7 Rastering wear test data plot showing a trenched area on the right of the test area and a pile-up area on the left....64

5-8 Reciprocating wear test showing the transient areas near the ends of the reciprocation and the area over which the friction force data is analyzed....66

6-1 Large radius tip scanning a small radius asperity. 68

6-2 Sharp asperity milled on silicon to scan indenter tip. 69

6-3 Scanning image produced with a sharp asperity by rastering first in the x direction, and then in the y direction. 70

6-4 Transmission Electron Microscope 200 CX sample holder with tip holder fixture and indenter tip mounted. 71

6-5 The upper images are taken at 40º CCW, 0º, and 40º CW respectively. The lower image shows data points plotted along the profile. 72

6-6 Kikuchi map observed in diffraction mode. 73

6-7 Top down view of the single crystal diamond indenter tip with crystallographic orientations and sliding direction indicated. 73

6-8 X-ray diffractometer with a representation of Bragg's law. 75

6-9 X-ray scans of the six different gold films shown with indexed peaks. 77

6-10 Grain size and strain versus gold film thickness. 79

6-11 Wear track in center of image to be prepared with cross sectional TEM parallel to the wear direction. 81

6-12 Focused ion beam cross section sample preparation. 82

6-13 Cross section removed from the sample trench with a glass rod. 83

6-14 Trenched area in preparation of fixed sample method slice and view serial sectioning procedure. 84

6-15 Slice and view rotating sample method. 86

6-16 Gold films with wear tracks run for half cycles at 500 μN normal load. Film thicknesses are indicated on each image. 88

7.1 Hardness determined by the Oliver and Pharr method versus maximum tip displacement for five samples of varying thickness. 89

7-2 Stone plot including linear curve fits for sample EBE 20 with a gold film thickness of 27 nm. 92

7-3 Stone plot including linear curve fits for sample IBS 100 with a gold film thickness of 105 nm. 93

7-4 Stone plots including linear curve fits for samples EBE 200, IBS 300, and EBE 500 with a gold film thickness of 180 nm, 315 nm, and 537 nm, repectively. 94

7-5 Hardness determined by four methods plotted versus sample thickness for five samples. 96

7-6 Scanning electron micrographs from a rastering wear test matrix with a 40 μN normal load varying tip geometry and number of cycles as indicated. 97

7-7 Scanning electron micrograph showing a rastering wear anomaly. The wear scar extends outside of the prescribed area especially in the horizontal direction. 98

7-8 Scanning electron micrograph showing a rastering wear anomaly. A trench develops on the right and lower edge of the wear scar.. 98

7-9 Scanning electron micrographs of samples IBS 300 (left) and EBE 200 (right) run for 30 cycles at 500 μN normal loads. 99

7-10 Scanning electron micrographs of sample EBE 200 C run for 3 cycles (left) and 30 cycles (right) at 500 μN normal load.....100

7-11 Scanning electron micrograph of sample IBS 100 after 1 cycle of sliding with 500 μN normal load.....102

7-12. Nominal film thickness versus number of cycles prior to film failure. 103

7-13 Vertical tip displacement versus lateral displacement for a 30-cycle reciprocating test. 105

7-14 Transverse cross section of a wear scar run on sample EBE 500 for 10 cycles with a 500 μN normal load. 106

7-15 Depth of wear scar versus number of cycles for samples run at 500 μN normal load. 108

7-16 Fraction of coating depth penetrated versus number of cycles for samples run at 500 μN normal load. 109

7-17 Friction coefficient versus number of cycles in log scale for gold on silicon samples without carbon run at 500 μN normal load. 111

7-18 Friction coefficient versus number of cycles on a log scale for gold on silicon samples without carbon coating run at 100 uN normal load. 112

7-19 Friction coefficient versus number of cycles for gold on silicon samples with carbon coating run at 500 uN normal load. 113

7-20 Friction coefficient versus number of cycles for gold on silicon samples with carbon coating run at 100 uN normal load. 114

7-21 Friction coefficient versus number of cycles for a contact pressure of 92 MPa run on sample EBE 200.....115

A-1 Wear scar of gold on silicon at 100 μN load normal load.....119

A-2 Wear scar of gold on silicon at 500 μN load normal load.....120

A-3 Wear scar of carbon on gold on silicon at 100 μN load normal load.....121

A-4 Wear scar of carbon on gold on silicon at 500 μN load normal load.....122

B-1 Sample IBS 100 at 500 μN normal loads. A)1 cycle. B) 3 cycles. 123

B-2 Sample EBE 200 at 500 μN normal loads. A)1 cycle. B) 3 cycles. 123

B-3 Sample EBE 200 at 500 μN normal loads and 10 cycles. 124

B-4 Sample IBS 300 at 500 μN normal loads. A)1 cycle. B) 3 cycles. 124

B-5 Sample IBS 300 at 500 μN normal loads. A) 10 cycle. B) 30 cycles. 124

B-6 Sample IBS 300 at 500 μN normal loads. A) 100 cycle. B) 300 cycle 125

B-7 Sample EBE 500 at 500 μN normal loads. A) 1 cycle. B) 3 cycle.....125

B-8 Sample EBE 500 at 500 μN normal loads. A) 10 cycle. B) 30 cycle.....125

B-9 Sample EBE 500 at 500 μN normal loads. A) 100 cycle. B) 300 cycle.....126

Abstract of Dissertation Presented to the Graduate School
of the University of Florida in Partial Fulfillment of the
Requirements for the Degree of Doctor of Philosophy

A METHODOLOGY FOR TRIBOLOGICAL EXAMINATION OF
THIN FILMS IN THE NANODISPLACEMENT REGIME

By

Gerald R. Bourne

August 2006

Chair: Luisa A. Dempere
Cochair: W. Gregory Sawyer
Major Department: Materials Science and Engineering

This research aims to develop a methodology for studying tribology of thin films on the nanodisplacement level for both fundamental and practical wear applications. A Hysitron Triboindenter was chosen to perform the majority of the wear testing of this study.

Thin film gold on silicon is chosen for its applications in micro-electrical mechanical systems (MEMS) devices, electrical switching contacts, low surface roughness, and its thermodynamic stability at ambient temperature and pressure. Samples are prepared with a variety of deposition techniques to vary film thickness. Various techniques are developed to overcome challenges with testing setup. An optics offset procedure solves resolution problems with light optical microscopy. Tip holders are designed to alter contact pressures and wear conditions. Load functions are designed to operate the equipment in a linear reciprocating motion.

Numerous characterization techniques including scanning electron microscopy (SEM), focused ion beam (FIB) transmission electron microscopy (TEM), and x-ray diffraction (XRD) are employed to characterize testing parameters and results. Geometrical and mechanical properties of the tip are characterized using TEM. The sample thickness and microstructure are characterized using XRD, SEM, FIB, and TEM. From the characterization, elastic and plastic properties are approximated using elastic theory and the Hall-Petch relationship. For quantifying wear, SEM and FIB are used for depth measurements.

An indentation model is proposed to include material pile-up exhibited by plastic films on elastic substrates which has been ignored in other models. Results show good agreement with the Hall-Petch relationship. Displacement and friction results show good reproducibility with repeat testing. Friction coefficient proves to be a good indication of film failure.

CHAPTER 1
INTRODUCTION AND BACKGROUND

Introduction

The term 'tribology', coined circa 1965 and defined as, "The branch of science and technology concerned with interacting surfaces in relative motion and with associated matters (as friction, wear, lubrication, and the design of bearings)," by the Oxford English Dictionary, is centuries newer than the study of friction and wear. For much of history up to and including the present day, tribological problems are often handled with an alchemistic approach by choosing a variety of materials and empirically testing. One might wonder if some studies were designed with a periodic table of the elements and a handful of darts. Much of the problem has been the lack of experimental, computational and characterization equipment with the capabilities required to study fundamental tribological interactions. The past decade has seen advances in electron microscopy to sub-nanometer resolutions, computers and software simulation to represent 10^6 atoms, and mechanical testing instrumentation to resolve 10^{-7} N loads and nanometer displacement. Tribological testing on the nanometer displacement level, supported by high resolution characterization is necessary to validate finite element modeling and molecular dynamic (MD) simulations of surface interactions.

In addition to fundamental studies of tribology, wear on the nanodisplacement level has applications in microelectromechanical system (MEMS) power transmission and ohmic contact switching. With steady trend towards miniaturization, MEMS devices have received much attention and interest. Due to the extensive research and

development of fabrication technology for integrated circuit (IC) chips, silicon was a convenient material for pioneering work in MEMS devices. It was quickly discovered that for mechanical sliding as in power transmission devices, silicon components will fail with limited cycles and could not be used outside of laboratory conditions. Wear resistant thin film coatings may provide solutions for silicon MEMS and will require tribology testing equipment and methodologies to support research [1].

Interest in tribological study of thin films extends beyond MEMS devices. Often in successful wear resistant materials combinations, a transfer film from one of the materials develops on the other. The result is a self-mated contact which after an initial run-in period exhibits good wear resistance and low friction. Typically when these transfer films exhibit desirable wear properties, they are thin, on the micron to sub-micron scale, and very adherent. A methodology to study and probe properties of transfer films is useful in the design of contacts that will exhibit them. A set of standards for the mechanical testing of thin film coatings is necessary for future developments in the field [2].

This research aims to develop a methodology for studying tribology on the nanodisplacement level for both fundamental and practical wear applications. A Hysitron Triboindenter was chosen to perform the majority of the wear testing of this study for the following reasons:

- The range of load and displacement. The Triboindenter's practical load range is from 1 μN to 10 mN and displacement is from 1 nm to 5 μm. These ranges cover loads and displacements in MEMS devices, thin film applications, and modeling simulations.
- The flexibility of tip geometry and materials. The tip holder can accept a wide range of materials and geometries. There is no need for elaborate manufacturing techniques to produce tips.

- The accurate stage positioning. Accurate positioning of test areas is possible to sub-micron resolution. This allows for precise location of test area prior to testing, and post-test characterization of the test area.

- The scratch mode. The scratch mode of the Triboindenter can be tailored to reproduce motions expected in MEMS devices and other practical applications. Reciprocating and unidirectional sliding is a fundamental geometry used in tribological applications and computational simulations.

- The experimental reproducibility. Tests on the Triboindenter show good reproducibility.

This study will present a new approach for tribological testing with a characterized standard which will be available for further studies. It will provide a foundation on which to expand research on various materials, geometries, modes of wear, and applications.

Background

Friction and wear are by no means new phenomena. From the earliest times, man has experienced friction and wear. To early man, friction was beneficial in creating fire by frictional heating of wood, and wear was used to sharpen tools for hunting and working. From the early 1700s to the early 1900s, friction and wear are studied mostly as a scientific curiosity. As the industrial revolution progresses friction and wear are seen as engineering problems which lead to energy loss and machine failure. Therefore the interest in studying the phenomena greatly increases. As the resolution of measuring and characterization devices improve and computer simulation power increases, the study of friction and wear progresses from the macro- to micro-, to nano-, and approaching atomic displacement levels. The driving forces for tribological research involve device longevity, energy conservation, economy, and fundamental understanding [3].

Early Friction Studies

The study of friction and wear dates back to the beginnings of the scientific era. Amontons (1699) is credited with the first observation that friction force is proportional to the normal load and independent of the contact area, hence Amontons' Law:

$$F_f = \mu F_n \tag{1-1}$$

where F_f is the frictional force, tangential to the surface, F_n is the force normal to the surface, and μ is the friction coefficient. Actually Amontons concluded that the friction force was always equal to one third of the normal load [4]. He explained this as interlocked asperities on the surfaces which caused a lifting motion to move relative to each other which caused an energy loss and therefore a friction force. This theory became known as the "roughness hypothesis". Subsequent researches found that the friction coefficient did not equal one third for all materials, but agreed that the normal load and friction force were proportional. The roughness theory remained accepted for hundreds of years. Alternate theories involving adhesion were proposed, but could not be validated without relating the friction force dependence on contact area [3]. A significant contribution to the adhesion theory came from Holm (1938) when he showed that the real area of contact is related to the normal load divided by the yield pressure (or hardness) of the material [5]. It was therefore realized that the real area of contact, rather than the apparent area of contact, was responsible for the friction force and since the real area of contact was proportional to the normal load, the friction force is subsequently proportional to the normal load.

Mechanism for Metallic Friction

The discovery by Holm paved the way for Bowden and Tabor's development of the mechanism for metallic friction. Bowden and Tabor showed that the frictional for force to translate a slider along a surface is comprised of two factors: the force required to shear the contact between the two intimate surfaces and the force to plough, or plastically deform the material in front of the slider. Their equation for friction force takes the form:

$$F_f = F_d + F_s \tag{1-2}$$

where F_f is the frictional force, F_s is the interfacial shearing force, and F_d is the force of plastic deformation (or ploughing). They expand this equation by breaking down the interfacial shearing force to an interfacial shear stress times the area it is acting upon, and breaking down the force of plastic deformation to the pressure required to yield the material times the projected area of the slider in contact with the surface in the direction of sliding and Equation 1-2 takes the form:

$$F_f = HA_p + \tau_s A_{real} \tag{1-3}$$

where H is the hardness of the material which is taken as the pressure required to deform the material, A_p is the projected area of the slider in the direction of sliding and in contact with the surface, τ_s is the interfacial shear stress, and A_{real} is the area of the slider in contact with the surface (Figure 1-1).

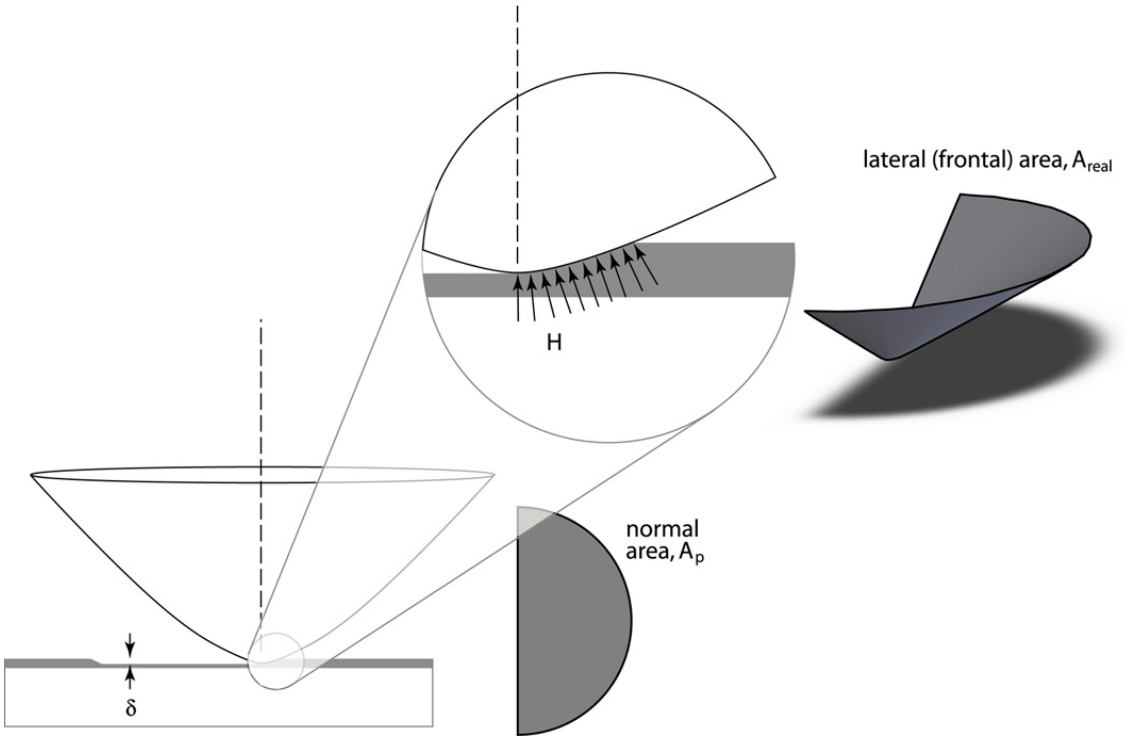

Figure 1-1. A schematic diagram representing the slider and areas from Equation 1-3.

Bowden and Tabor tested this equation with a set of three sliders, one with the geometry of a circular spade, one spherical, and one cylindrical, all three with the same radius (Figure 1-2). The tests were made with steel sliders on an indium surface with a slow sliding speed of 0.1 mm/s to avoid strain rate sensitivity. From the geometry of the sliders, it can be seen that the F_s term from Equation 1-2 or $\tau_s A_{real}$ term from Equation 1-3 will be negligible for the spade slider and will be a maximum for the cylindrical slider.

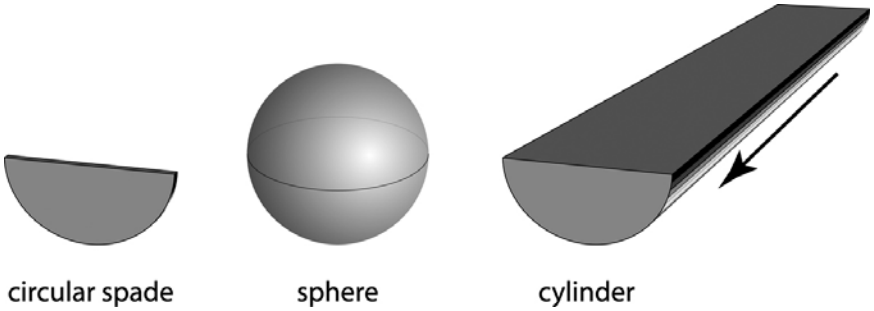

Figure 1-2. Schematic drawing of the three slider geometries from Bowden and Tabor's experiment.

Results from the experiments showed a deformation pressure equal to 1.5 times the material hardness measured by indentation. Bowden and Tabor suggest this result may be due to the fast sliding speed relative to the slow indentation speed, further suggesting some strain hardening effect. The experiment was repeated on four different surfaces, indium, lead, steel, and copper, and the results of the interfacial shear stress were compared with the shear strength of the material. The interfacial shear strength was on the same order of magnitude as the shear strength of the material, but 1.5 to 2 times higher than the bulk shear strength.

Sliding Wear

Prow Formation

A mechanism for wear of a metallic surface by a linear slider is described by Antler as a severe adhesive process called prow formation [6]. A net metal transfer occurs from the surface to the slider. This transferred material is described as a lump of severely work hardened metal (the prow) transferred to the slider which in turn continues to wear the surface by plastic shearing or cutting while the slider remains unworn. Prows are removed from the slider by transferring back to the surface or becoming loose debris. If the slider continues to ride over virgin material, prow formation continues throughout the wear test. With dissimilar materials, friction and contact resistance characteristics of the system are determined by the prow metal, therefore a diamond slider on a gold surface should behave as a self-mated gold contact [7]. Antler found that the size of prows is inversely related to the hardness, and metals that do not work harden, fail to form prows. He attributes this to the prow becoming harder than the surface from the severe deformation and then being able to cut the surface [8].

Cocks proposed the following mechanism [9] for prow formation:

- adhesion occurs between the slider and the surface
- plastic deformation occurs in a volume of metal from the surface
- adhesive forces are sufficient to remove the metal from the surface
- the metal transfers to the slider as a chip
- the process repeats on the chip
- the chip becomes too large and detaches from the slider

Antler found that with a linear reciprocating slider, prows would be deposited at the ends of the tracks and prow formation would eventually stop when the surface material work hardened to a hardness higher than that of the slider in which case would cause the slider to begin wearing. From empirical observations, the following equation was developed:

$$N_{prow} = 1.7 \frac{x(cm)}{F_n(N)} \tag{1-4}$$

where N_{prow} is the number of cycles for which prow formation will continue, x is the track length in centimeters, F_n is the normal load in Newtons [5].

Rabinowicz and co-workers have suggested that materials that show little to no solid solubility and form immiscible liquids would make good candidates for mated materials in adhesive wear sliding applications [3]. Antler challenges this theory based on experiments with gold mated with platinum and gold mated with rhodium [5] that show similar performance to gold on gold. Antler suggestions for adhesive wear contacts are high hardness to limit initial contact area, and low ductility to limit junction growth.

Delamination Theory

Delamination wear occurs in reciprocating sliding when cracks nucleate below the surface and result in liberating sheets of material. Crack nucleation can occur in areas of high plastic deformation at dislocation pile-ups particularly at hard precipitates in a softer

matrix or between material interfaces like a substrate/film interface [10]. Suh discovered delamination wear typically occurs with harder sliders on soft surfaces. Prow formations and delamination wear are different mechanisms and are mutually exclusive [5]. Delamination wear has been reported in reciprocating sliding on gold plated contacts [11].

Subsurface Wear

Gold plated systems have shown subsurface plastic deformation leading to the formation of buckles on the surface layer. With continuous sliding exposure of the sub-layers can occur with or without thinning of the surface layer. Increasing normal load results in less number of cycles to produce buckling and exposure of the sub-layer. It was found that increasing layer thickness can reduce or eliminate the mechanism [12].

Film Thickness Wear and Friction Dependence

Several research groups have investigated thin metallic films as a solid lubricant in sliding contact applications [4, 13-17]. All found that friction and wear were initially high for ultra thin coatings but as coating thickness was increased, both friction and wear went through minima values at some critical coating thickness (Figure 1-3). Table 1-1 summarizes the results from the various research groups. In some studies, tribometer geometries were not well defined and experimental details were not mentioned. Two of the research groups studied sputtered coatings versus evaporated coatings and both found the sputtered coatings exhibited lower friction coefficients and longer life than the evaporated coatings [14, 17]. Both groups attributed this behavior to better film adhesion and finer grain structure, resulting in higher coating hardness, exhibited by sputtered coatings. Antler improved his coating by alloying gold with cobalt [13] The cobalt acts as a solid solution strengthener to harden the gold film.

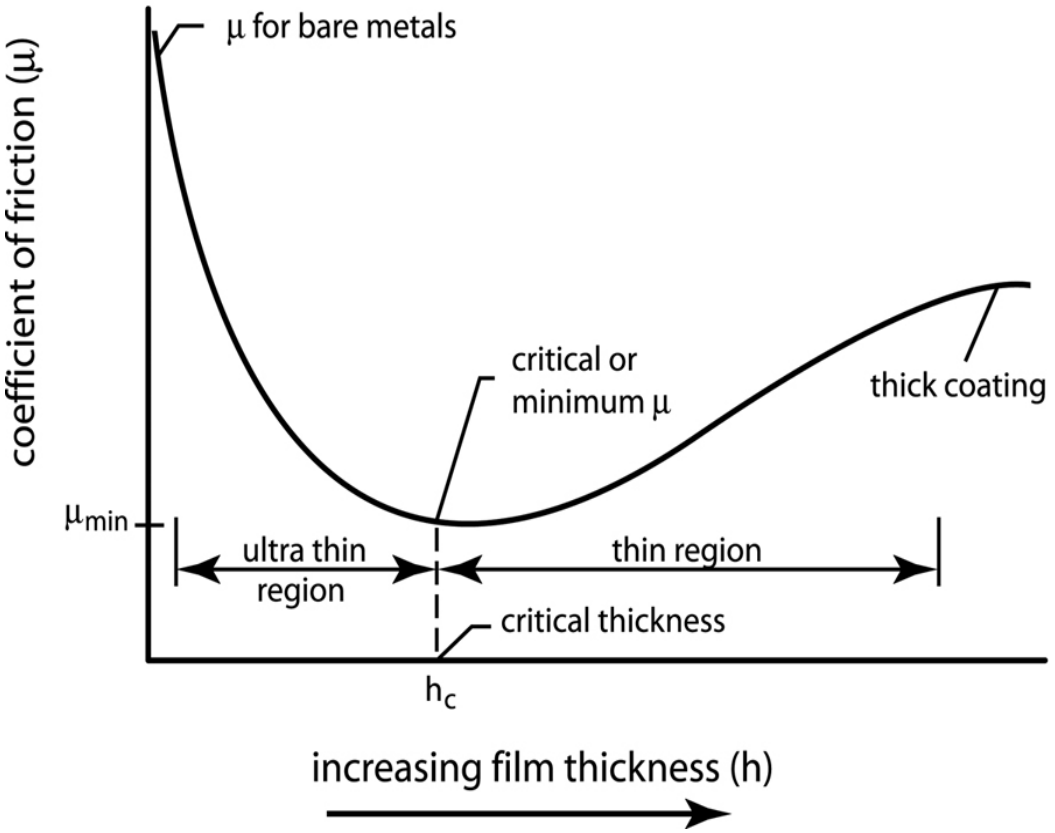

Figure 1-3. Schematic representation of the effect of film thickness on friction coefficient of metallic film solid lubricants on harder substrates (reproduced from [17]). The critical thickness where μ (the friction coefficient) goes through a minimum is denoted as h_c.

Table 1-1. Summary of studies of thin metallic films on substrates.

film/substrate	h_c (μm)	μ	tip radius (μm)	load (N)	reference
In/steel	0.1-1	0.5	3000	39.2	[4]
Pb/steel	0.5	0.05	3175	29	[15]
In/steel	0.5	0.05	3175	29	[15]
Sn/iron/glass	0.1	0.15	3175	2.4	[16]
Au/steel	2.0-3.5	0.1	2375	2.45	[17]
Pb/steel	1.8-2.5	0.1	2375	2.45	[17]
Co-Au/Pd/Ni	0.05	0.4	N/A	1.96	[13]
Au/Si (111)	0.01	0.2	1600	0.001	[14]
Ag/Si (111)	0.007	0.2	1600	0.001	[14]

Modeling

Several attempts have been made to develop models to describe friction and wear phenomena in thin films on substrates. Bowers and Zisman modeled the friction coefficient of a thin gold film on a steel substrate based on a pressure dependent shear strength which showed good agreement with experimental data [18]. They calculated a friction coefficient of 0.1 assuming no plastic deformation of the steel substrate. El-Shafei et. al. investigated thin films of lead on steel with a contact radius larger than the film thickness [19]. They found good agreement with a Hertzian elastic contact model once their contact radius exceeded five times the film thickness. Finkin sought to explain the ultra-thin to thin film transition phenomenon seen in Figure 1-3 [20]. He developed two theories to explain the two regimes. The ultra-thin regime is explained as stiffening due to coupled stresses with a quantitative expression verified by data from literature. The coefficient of friction in thin film regime is shown to be proportional to the square root of the film thickness divided by the normal load based on a thin film with modulus much less than the substrate. Jang and Kim, and Schiffmann and Hieke incorporate a ploughing term in their wear models which takes plastic deformation into account [14, 21]. For these models, tip geometry, contact geometry, and plastic properties of the film and substrate are necessary parameters. Difficulty in measuring these parameters is attributed to discrepancies with the models and experimental results.

The combinations of substrate properties, film properties and thicknesses, sliders, and geometry lead to different modes of wear. Due to the complexity of the problem, no single model or solution is expected to explain all possible wear combinations and geometries. A model that describes the friction coefficient of a thin soft film on an

elastic substrate of significantly higher modulus is not expected to describe a hard elastic film on a soft compliant substrate. A variety of models need to be developed to explain specific cases.

CHAPTER 2
EXPERIMENTAL MATRIX

An experimental matrix was designed to test various microstructures, film thicknesses, number of reciprocations, and normal load effects on wear resistance of gold films on silicon substrates. Gold was chosen for its applications in MEMS devices, electrical switching contacts, and its thermodynamic stability at ambient temperature and pressure. Standard metallographic polishing techniques were initially used to prepare sample surfaces. Wear testing and profilometry revealed surface roughness effects which excluded the use of bulk gold. Polishing media particles were embedded into the surface changing the properties of the material and the roughness produced was on the scale of the measurements taken. Therefore commercially available polished silicon wafer was chosen as a substrate material for its low surface roughness. In addition, silicon has direct applications in MEMS research. A variety of microstructures and sample thicknesses were produced using deposition techniques including ion beam sputtering (IBS) and electron beam evaporation (EBE). An amorphous carbon layer of approximately 60 nm in thickness was deposited on half of the samples to explore an electrically conductive friction modifying substance. The samples with and without carbon will be referred to as coated and uncoated respectively.

Samples were named based on the deposition technique and the targeted approximate film thickness in nanometers (Table 2-1). Normal loads were chosen of 100 μN and 500 μN because the instrument shows good repeatability and low signal to noise ratio at these levels. With the 100 μN normal load setting, number of reciprocations was

varied from one forward pass, referred to as a half cycle, to 300 cycles in the following increments: half cycle, one cycle, three cycles, 10 cycles, 30 cycles, 100 cycles, and 300 cycles. Although the reciprocating tip is diamond and is therefore much harder and more wear resistant than the gold foils, some precautions were taken to avoid possible tip damage. For the 500 μN normal load setting, the 100-cycle and 300-cycle tests were omitted if film failure was detected on samples at 30 cycles to avoid excessive number of reciprocations on the harder silicon substrate. The combination of loads and number of cycles results in 12 different test parameters. Each set of tests was repeated four times on all 12 samples for a total of 576 wear tests.

Table 2-1. Sample naming designations.

Approximate sample thickness	Without amorphous carbon	With amorphous carbon
20 nm	EBE 20	EBE 20C
100 nm	IBS 100	IBS 100C
200 nm	EBE 200	EBE 200C
300 nm	IBS 300	IBS 300C
400 nm	EBE 400	EBE 400C
500 nm	EBE 500	EBE 500C

Sample Preparation

Gold was chosen as the test material for its applications in the electronics industry, and its mechanical and chemical properties described previously. A variety of samples were produced and can be categorized into three basic types including bulk gold foils, ion beam sputtered gold on silicon wafer, and electron beam evaporated gold on silicon wafer. These various techniques were chosen to introduce microstructure, surface roughness, and film thickness variables into the test matrix.

Bulk Gold Foil

Initial experimentation was performed on bulk gold samples. A 100 μm thick 99.9975% gold foil was cut into 10 mm x 10 mm sections and mounted onto steel gauge blocks using a cyanoacrylate based adhesive. Samples were polished using a South Bay Technologies manual polishing wheel (Figure 2-1) beginning with grinding discs of 240 grit silicon carbide rotating at a speed of 200 rpm. After a short time of material removal, the polishing wheel was cleaned and the grinding media was changed to 320 grit and the sample was rotated 90º to the previous polishing direction. The sample was polished until no scratches from the previous step were detectable using an optical stereoscope. This procedure was repeated using 400 and 600 grit respectively. Upon completion of the grinding steps, the media was removed and the wheel was cleaned. Next a billiard cloth was mounted on the polishing wheel and water-based slurry of 15 μm alumina (Al_2O_3) was used as a polishing media. The slurry was used to wet the billiard cloth and samples were polished by rotating the sample manually in the opposite direction of rotation of the polishing wheel. Samples were polished until scratches from the previous steps were not detectable. The wheel was cleaned and the process was repeated with fresh cloth and 5 μm slurry. The process was then continued using 1 μm, 0.3 μm, and 0.05 μm slurries respectively on velvet cloth. Upon completion of the final polishing step, the samples were examined in a Wyko optical profilometer to verify consistent surface roughness.

Figure 2-1. South Bay Technology 8” polishing wheel

Ion Beam Sputtered Gold on Silicon

Ion beam sputter coating is often used to produce thin films for conductivity to aid in imaging in electron microscopy. The advantage to ion beam sputtering versus other techniques is that the samples are not exposed to extreme temperatures. The low temperature deposition is beneficial in producing and retaining a fine grained or amorphous structure. Producing coatings on polished silicon wafers will yield surface roughness values that would be exceptionally challenging to obtain by metallographic polishing techniques.

The ion beam sputtering process is illustrated in the schematic in Figure 2-2. An argon ion beam is produced by dual Penning guns. The guns are aimed to strike the target of desired deposition material. Material from the target is sputtered off, and deposited on the sample substrate. The substrate can be rotated to provide uniform deposition. This system is contained in a chamber that can be evacuated to levels of 10^{-6} Torr.

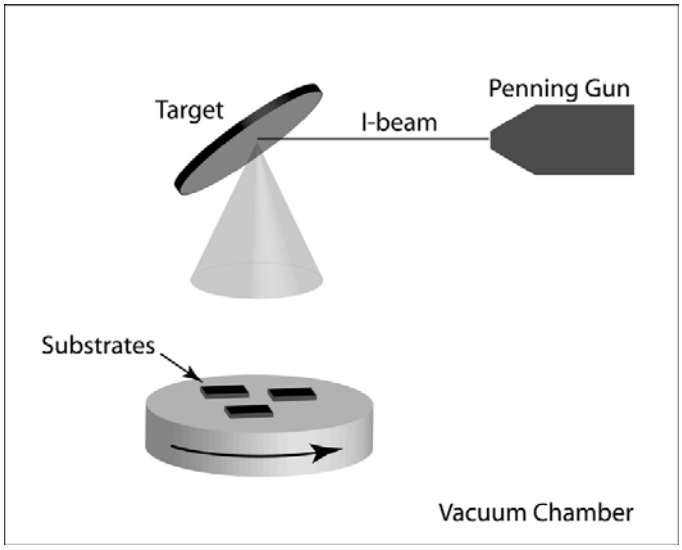

Figure 2-2. Ion beam sputtering process

Commercially available 0.6 mm thick single crystal silicon wafer with (001) plan view orientation was scored and cleaved along <110> directions to produce substrates of approximately 25 mm^2. The substrates were cleaned by sonicating in acetone. This was repeated three times using new acetone each time. The substrates were then sonicated in methanol three times using new methanol each time. Finally the substrates were blown dry using laboratory grade Freon spray. Several substrates were mounted for coating in a Gatan Model 681 High Resolution Ion Beam Coater seen in Figure 2-3.

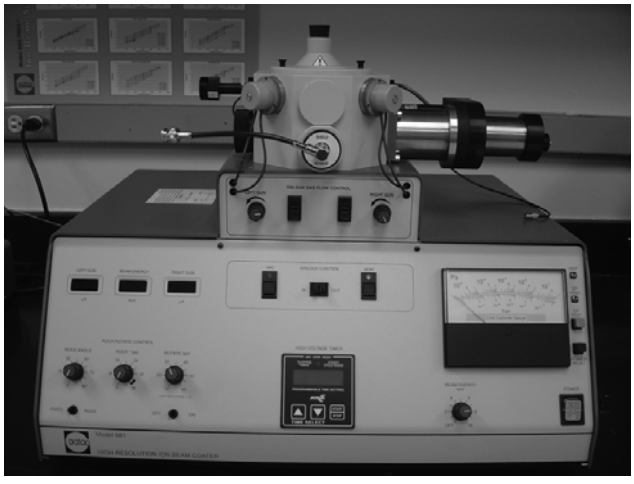

Figure 2-3. Gatan Model 681 High Resolution Ion Beam Coater

It is well known that gold has poor adhesion when deposited on silicon and a thin titanium bond coat will greatly enhance gold film adhesion. A target of 99.99% gold was mounted on one side of the dual target holder using conductive silver epoxy and a target of 99.99% titanium was mounted on the opposite side. After sufficient curing time, the ion beam coater chamber was pumped down to a level of 2×10^{-4} Torr and the ion guns were purged with argon following the instruction manual. After purging, the ion beam was set to 9 keV at 600 μA for 60 minutes with a sample rotation speed of 30 rpm.

Based on a deposition rate of 3.5 Å/s the film thickness should be on the order of 1 μm. The first batch of samples was run without a titanium bonding layer to examine the effect of film/substrate adhesion. A second set of samples were coated by first sputtering titanium with a 9keV ion beam at 300 μA for 15 minutes followed by gold with a 9 keV ion beam at 300 μA for 60 minutes. The lower current was used due to beam stability issues which could not be resolved over several repeated attempts. Once the coating process was complete, the silicon substrates were glued to 15 mm diameter atomic force microscopy (AFM) sample disks using a cyanoacrylate based adhesive. The AFM disks are ferritic steel which causes them to be attracted to magnets embedded in the testing equipment stage. It was discovered early in this project that the magnetic attraction of the stage was not sufficient to rigidly affix the samples to the stage, and an adhesive was needed when mounting samples on the stage of the test equipment. Late in this study it was determined that the AFM disks significantly hindered scanning electron microscope (SEM) examination due to the effect of magnetic fields on the electron beam. In hindsight, the AFM disks should have been eliminated.

Electron Beam Evaporated Gold on Silicon

Electron beam evaporation is another coating technique for producing high quality thin films on substrates. In contrast to ion beam coating, electron beam evaporation exposes the sample high temperatures due to the energy required to evaporate the metal. This leads to grain growth in the film which results in a coarser grained structure. The elevated temperature can also result in diffusion between the film and substrate. Again a bonding layer is used to enhance film adhesion. Titanium and chromium layers are often used for gold deposition on silicon. Since titanium has a lower diffusivity in gold than chromium, titanium was selected.

The electron beam evaporation process is illustrated schematically in Figure 2-4. An electron beam is generated by producing a large electrical bias between the electrode and the crucible. The crucible contained the desired film material. The electron beam heats the material in the crucible to a liquid and then to a gas which fills the chamber. The gas condenses on the substrate thereby producing a thin film on the substrate.

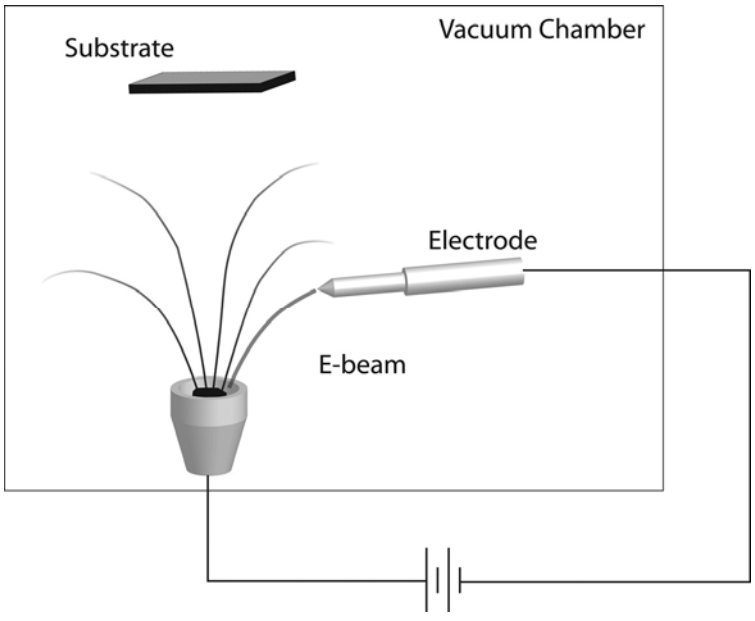

Figure 2-4. Electron beam evaporation process

Attempts were made to use an on-site electron beam evaporation system, but coatings were of a poor quality with many spheres of gold on the sample surface. Fortunately, high quality electron beam evaporated coatings on silicon (001) substrate are available commercially at economical prices. Wafers of 100 mm diameter with gold films of 20 nm and 200 nm were purchased and sectioned into samples as described previously. The sectioned samples were then glued to AFM disks using a cyanoacrylate based adhesive.

Carbon Arc Evaporation

To investigate an electrically conductive friction modifying coating, all samples were duplicated with a thin amorphous carbon layer using a carbon arc evaporation system. This procedure is similar to the electron beam evaporation except that a bias is applied across two carbon rods to evaporate carbon. The resultant condensation yields a thin amorphous carbon film. This process is illustrated schematically in Figure 2-5.

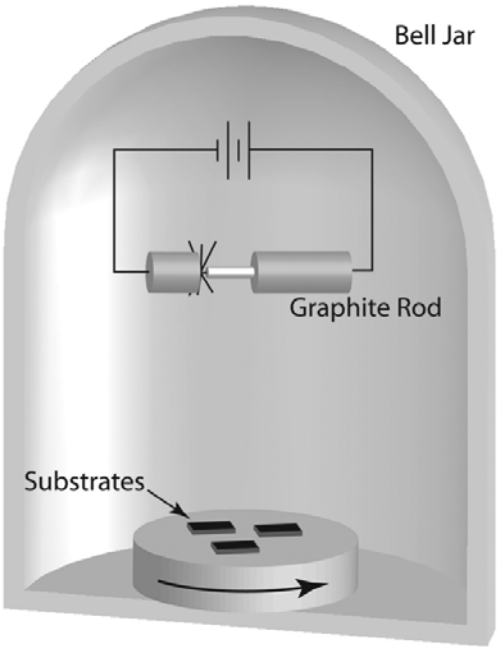

Figure 2-5. Carbon arc evaporation

Ion Beam Etched Area of Interest

Many of the tests conducted in this research leave residual damage smaller than the resolution limits of optical microscopy. Therefore, scanning electron microscopy (SEM) and transmission electron microscopy (TEM) are used to characterize the damage from testing. Even with the resolution obtainable with electron microscopy, locating micron and submicron surface features with displacements on the order of tens of nanometers or less is extremely challenging due to the low amount of contrast they produce, see Figure 2-6. Scanning at a low magnification to locate such features is not possible because the feature will not be visible. Scanning the sample surface at a high magnification without an indication of the approximate area is not practical because the field of view is much smaller than the entire area of the sample. A method to accurately position wear tests and to subsequently locate the tests in an SEM is necessary.

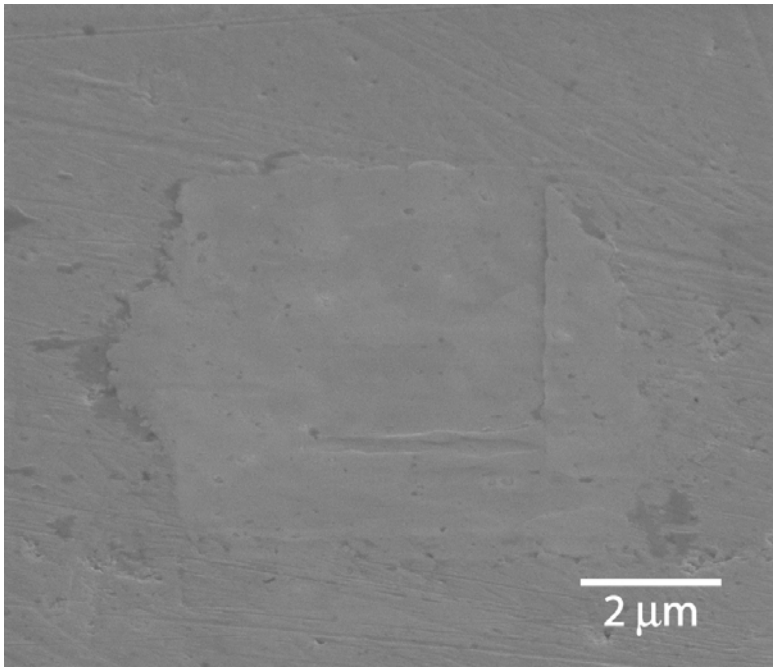

Figure 2-6. SEM image of 4 µm x 4 µm rastering wear test with low contact pressure.

A dual beam focused ion beam SEM was used to layout and etch grids on the samples' surface. Each grid square is 100 μm x 100 μm and the grid lines are approximately 1 μm wide and 1 μm deep, see Figure 2-7.

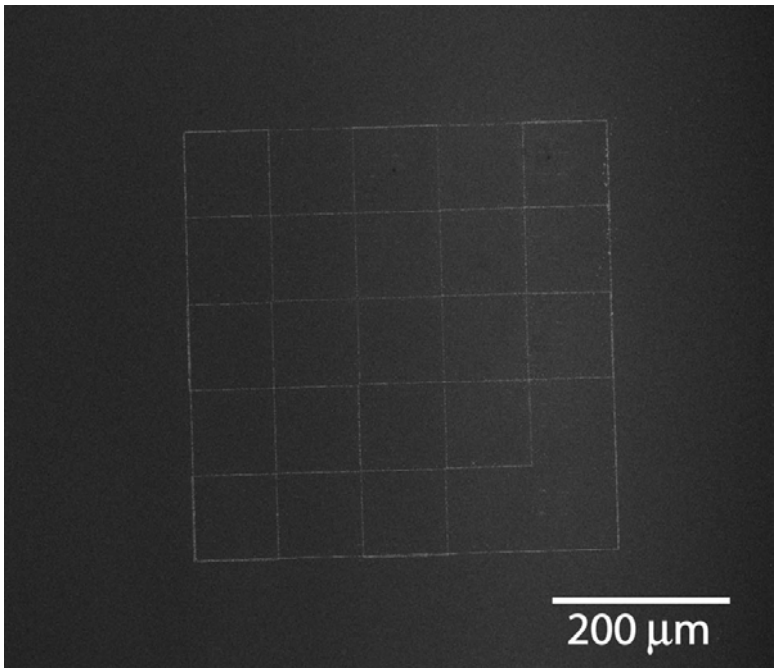

Figure 2-7. SEM image of etched grid lines for wear test location

The grid lines were aligned with <110> directions on the silicon substrate by setting the intersection of the cleavage planes {111} and the plan view plane (001) to be parallel with the x and y axis in the microscope. These markings are easily located in both the SEM and optical microscope and can be used situate the wear test and to identify the area for characterization. The markings allow wear tests to be run approximately parallel to a <110> direction on the substrate which will aid in locating a major zone for high resolution transmission electron microscopy (HRTEM) analysis in the JEOL 2010F which is limited to ~20º tilt.

CHAPTER 3
TEST EQUIPMENT

A wide variety of tribological equipment exists to test various wear conditions and contact geometries. By and large this equipment aims to prescribe specific sliding paths while controlling an applied normal load and measuring the frictional forces generated at the sliding interface. Most of this equipment does not make in situ measurements of wear; rather, wear is measured ex situ using gravimetric, metrological, or microscopy techniques.

The most common sliding motions are unidirectional, with the standard pin-on-disk tribometer being a device that prescribes a continuous rotary motion to a disk while holding a loaded pin stationary on the surface (Figure 3-1).

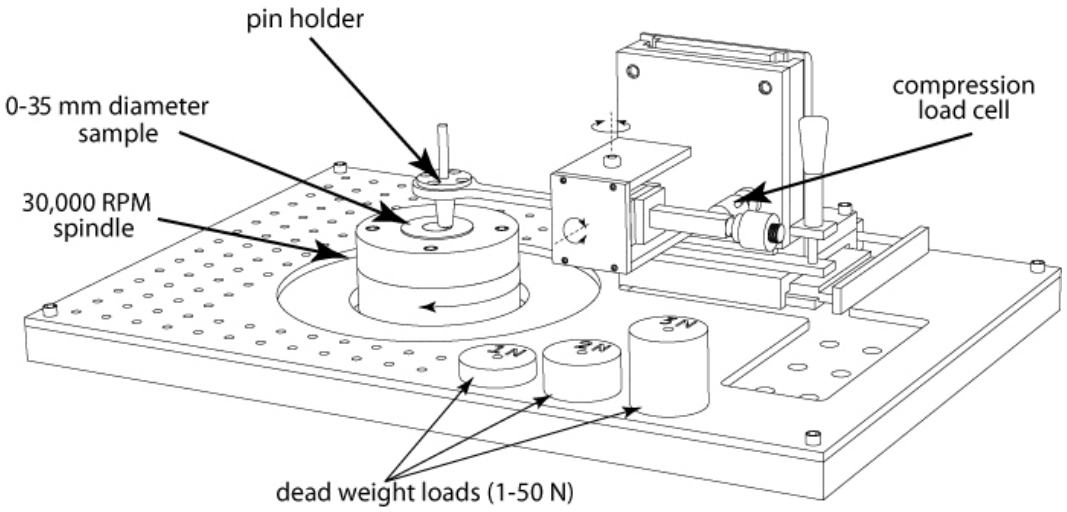

Figure 3-1. A typical pin-on-disc type tribometer

The reciprocating pin-on-flat tribometer is another common tribological testing appartus. In this configuration, the sample reciprocates in a linear direction against a stationary pin through which a normal load is transmitted (Figure 3-2).

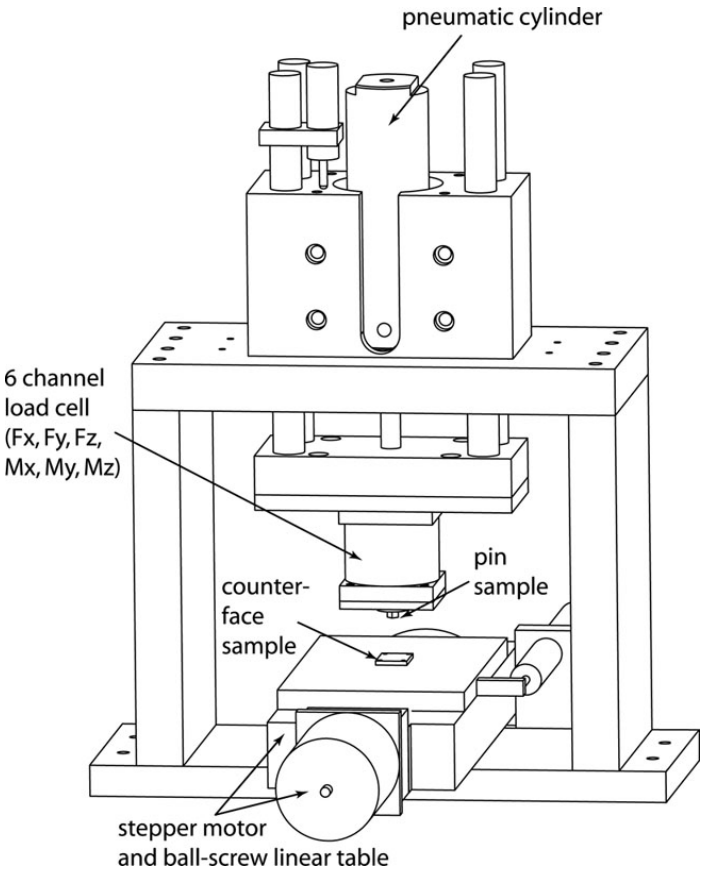

Figure 3-2. Linear reciprocating tribometer

Several researchers have begun to use atomic force microscopes (AFM) to study tribological surface interactions. Normal and lateral forces acting upon an AFM tip are calculated from deflections of the tip cantilever. From these forces, sliding friction is calculated. Accurate measurements of sliding friction from AFMs are exceptionally challenging, requiring well characterized cantilevers with well know material properties. There exists a gap in tribological test equipment from the AFM scale with nanonewton normal loads and nanometer to sub-nanometer normal displacements, to the

microtribometer scale with millinewton normal loads and micrometer displacements. Tribological conditions in MEMS devices and thin films fit in this regime and remain largely unstudied. In this study, the Hysitron Triboindenter is used to mimic a linear reciprocating tribometer and bridge the gap in scale.

Hysitron Triboindenter

The majority of wear testing done in this study was performed on a Hysitron Triboindenter. The Triboindenter is a commercially available nanodisplacement mechanical testing system whose primary function is nanoindentation (Figure 3-3).

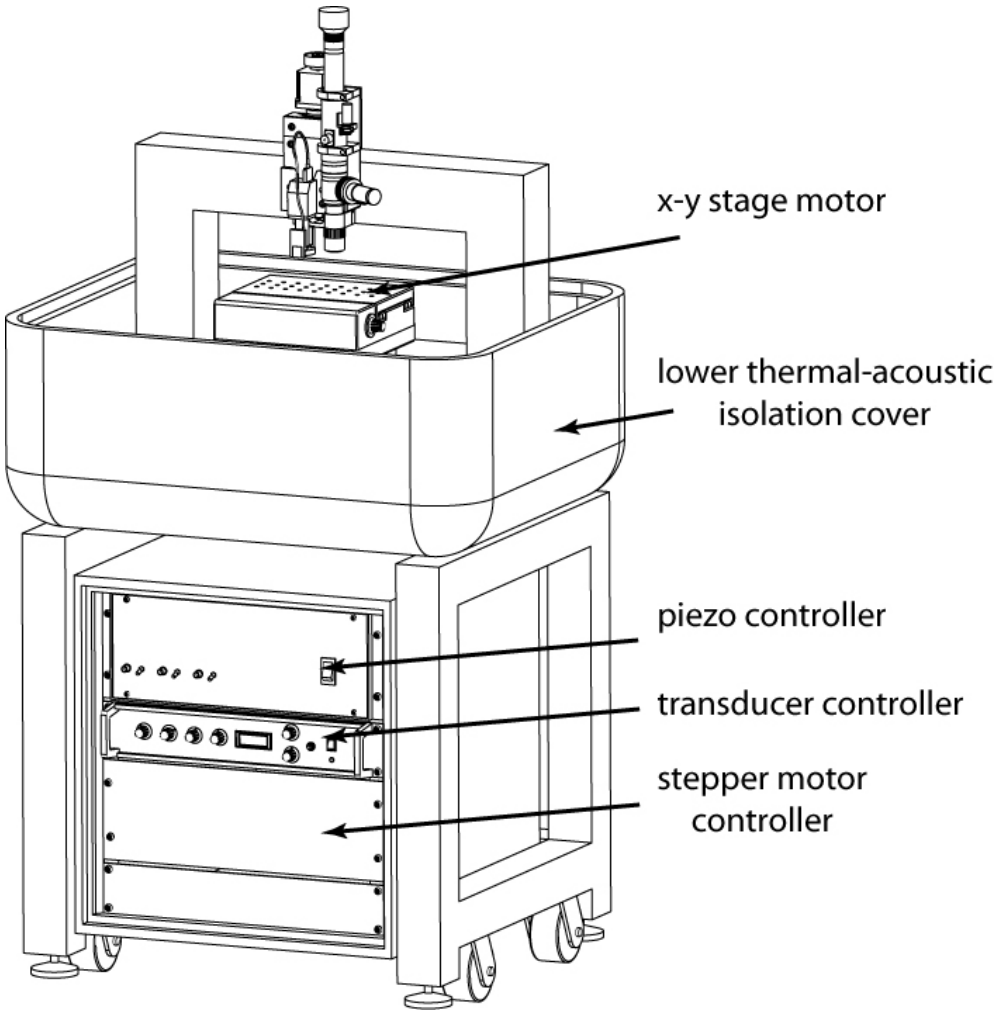

Figure 3-3. Hysitron Triboindenter with upper thermal-acoustic isolation cover removed to show interior details.

Loads, displacements, and measurements are performed by a capacitive transducer (Figure 3-4). The capacitive transducer assembly contains two parallel fixed plates with a parallel center plate supported by springs. An indenter tip is mounted to the center plate. To apply a load a DC potential is applied between the lower plate and the center plate. An electrostatic attraction displaces the center plate towards the bottom plate. Based on the spring constant of the support springs, the voltage can be calibrated to a force. For displacement measurements, an AC signal is applied between the center plate and top plate, and an AC signal of equal magnitude 180º out of phase is applied to the lower plate and the center plate. When the center plate is equidistant from the top and bottom plates, the net signal is zero. When the center plate is displaced a voltage is recorded and calibrated to a distance. A similar transducer is mounted to provide lateral displacements.

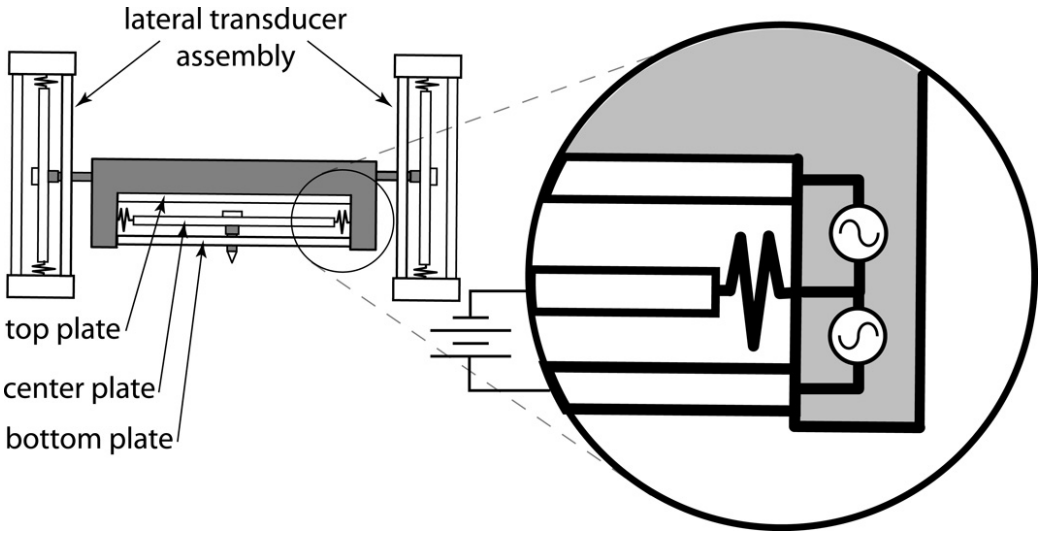

Figure 3-4. Capacitive transducer assembly schematic

The capacitive transducer assembly is mounted to a three axis piezo tube scanner similar to those found in AFMs. The piezo tube scanner allows for precise tip placement and can be used in conjunction with the transducer as a scanning probe microscope.

Using the tube scanner to raster the indenter tip in contact with a surface, the transducer can collect z displacements and produce an AFM-like image. The tube scanner is mounted to a z-axis stepper motor which provides coarse translations for tip approach. An optical CCD microscope is also attached to the z-axis stepper motor. The optical microscope allows for accurate sample location and test placement. The sample stage is attached to x-y stepper motors for translation (Figure 3-5). All systems are computer controlled.

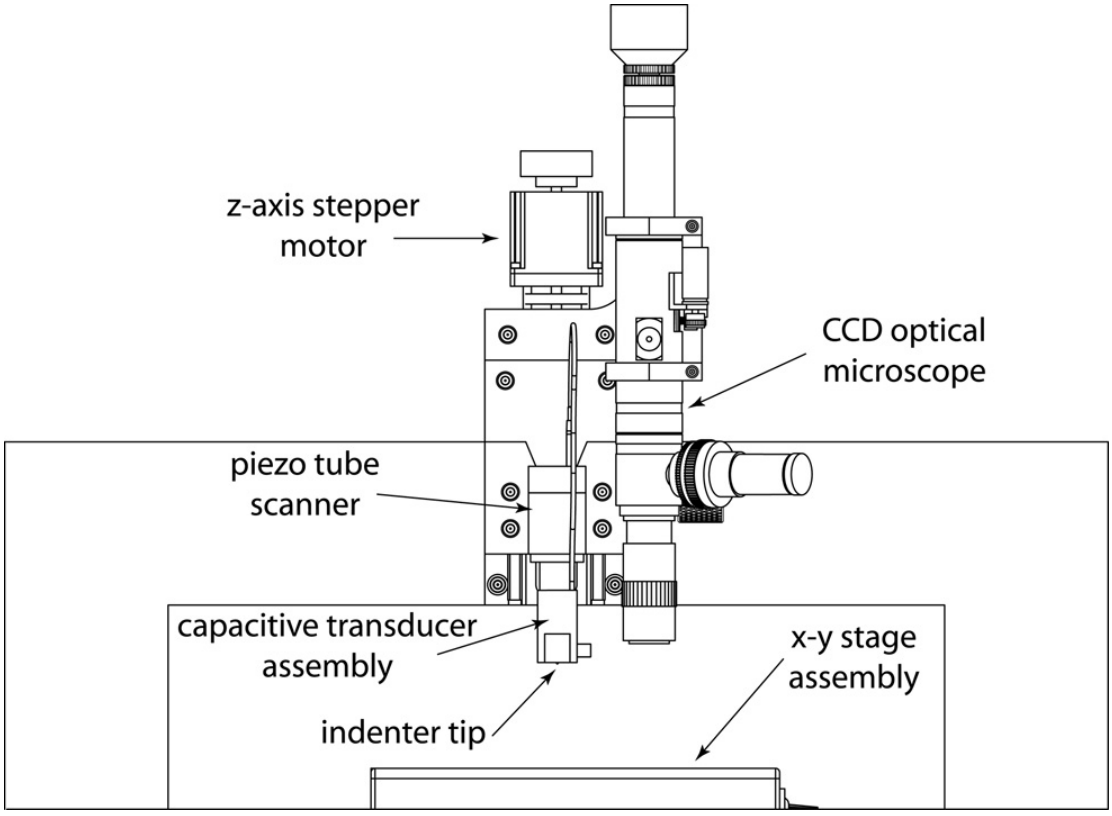

Figure 3-5. Enlarged view of Triboindenter components

The components are mounted on granite to dampen vibrational effects. The equipment frame also contains an active vibration isolation device. The working components of the Triboindenter are enclosed in a thermal-acoustical isolation chamber with provisions for environmental control.

CSM Microtribometer

The CSM Microtribometer is a commercially available tribological testing device that operates on scales orders of magnitude larger than the Triboindenter, but well below those of conventional test equipment (Table 3-1). This tribometer is available with a linear reciprocating stage or an interchangeable rotating stage to mimic both reciprocating and pin-on-disc tribometers. Rough stage translations are handled by stepper motors and fine translations and reciprocations are performed by piezos. A dual flexure both applies normal load and reacts to frictional forces between the pin and the counterface. Mirrors are mounted on this flexure in the horizontal and vertical directions. Optical light intensity sensors are positioned at a distance from the mirrors to read the magnitude of deflection of the flexure in the frictional and normal load directions (Figure 3-6).

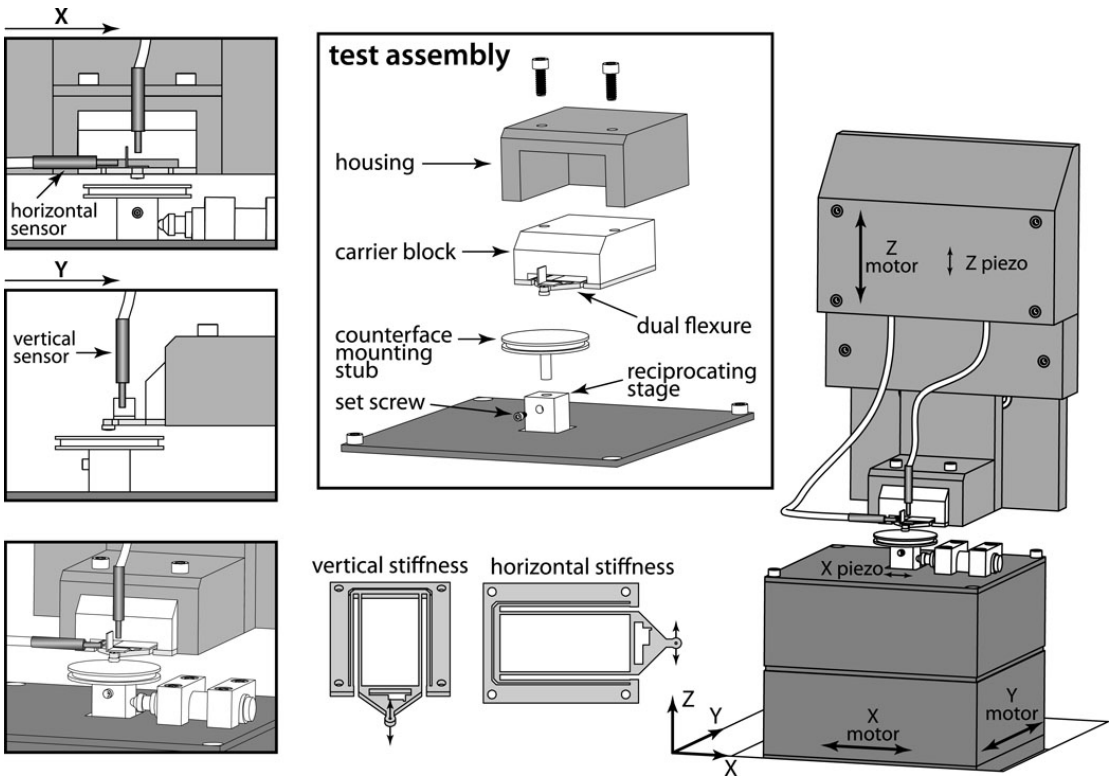

Figure 3-6. Schematic of CSM Microtribometer [22].

Table 3-1. Comparison of equipment loads and displacements

	Conventional Reciprocating Tribometer	Hysitron Triboindenter	CSM Microtribometer
maximum normal load	1.6 kN	10 mN	1 N
maximum lateral load	1.6 kN	2 mN	1 N
maximum normal displacement	50 mm	5 μm	0.1 mm
maximum lateral displacement	0.2 m	15 μm	0.6 mm

CHAPTER 4
EXPERIMENTAL PROCEDURES

Hysitron Triboindenter Procedures

Tip Preparation

For the most part, tips in indentation testing are not considered to be a parameter involved in a test. Typically tips are chosen so that they are significantly harder than the material being tested so that it can be assumed that they experience no plastic deformation. Diamond is the material of choice for indentation testing because it is the hardest material and its elastic properties are well characterized so that any elastic deformation experienced by the tip can be back calculated from the test data. Diamond tips are expensive costing approximately $2000 each. For indentation testing, this cost is not a huge factor because the tips will last for an exceptionally long time. In hardness testing, a sharp tip is often desirable to reach high contact pressures and induce plastic deformation.

In wear testing, the two materials in intimate contact are both considered. Often wear tests consist of self mated materials, gold on gold for example, or materials from a specific application, e.g., a bearing on a race. It is often found that both materials experience some change. In the case of a hard pin (or tip) moving across a softer flat, transfer of the softer material to the hard pin is of interest. Observing this material transfer in cross section is desirable, but would require destruction of the pin. Due to the high cost of diamond tips, it is not practical to section them. It is not uncommon for the pin to experience wear along with the surface. For diamond tips, wear of the tip should

be negligible and no transfer film of gold on to the diamond tip has been observed in the scanning electron microscope (SEM). Self mated materials could be tested by using coating techniques on the tip, but again, the high tip cost makes this prohibitive. An alternative to high cost diamond tips is needed.

A crucial parameter in wear testing is the contact pressure. Contact pressure is used to target desired wear modes, and to replicate applications. The factors involved in contact pressure are normal load and contact area. The normal load can be controlled by the Triboindenter, and the contact area varies with the tip geometry. In contrast to hardness testing, wear tests are often performed with much lower contact pressures requiring a blunt rather than sharp tip. By selecting tips of various radii, a wide range of contact pressure can be achieved.

For the reasons mentioned above, tips of relatively large radii are produced in addition to the sharp tips available from the manufacturer. Sapphire spheres of 100 μm to 1 mm are commercially available for a nominal cost of approximately $10.00 each. The original equipment manufacturer's (OEM) tip holder is machined on a lathe with a conical cut such that when a sapphire sphere is place in the tip holder, it will self-center (Figure 4-1). A small amount of cyanoacrylate based adhesive is used to attach the sapphire sphere to the OEM tip holder. The adhesive is allowed to cure overnight. The transducer piezo assembly is then removed from the Triboindenter for easier access. Once the tip has sufficiently cured, it is threaded on to the capacitive transducer with a special torque limiting wrench.

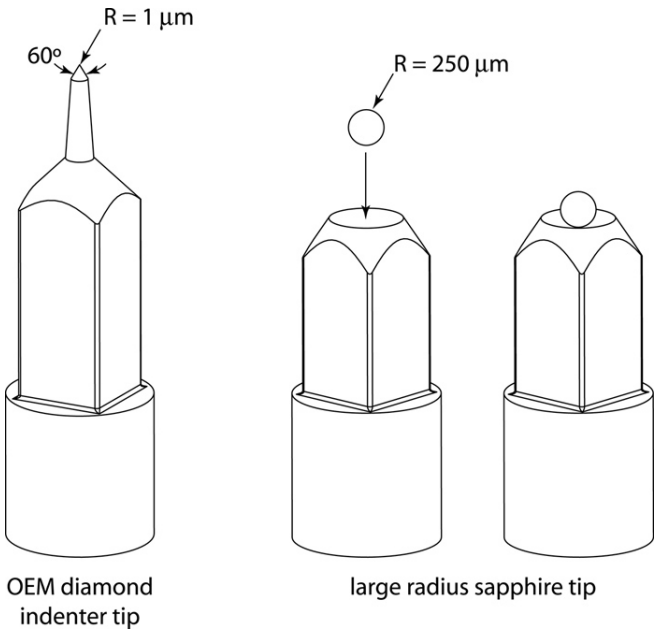

Figure 4-1. Illustration of an OEM diamond indenter tip and assembly of a large radius sapphire tip

Sample Mounting

The Triboindenter has a stage that contains six positions which are magnetized by rare earth magnets. Samples mounted on atomic force microscope (AFM) disks can be placed on the stage and will be sufficiently held in place for indentation testing. In preliminary tests, it was determined that this mounting system may not be effective for tests involving lateral translational forces. Therefore, samples are held in position with an alcohol soluble adhesive in addition to the magnetic forces. Once the samples are mounted and the stage replaced on the stage motor, the machine is powered on. The samples are imaged and focused on using the Triboindenter's optical charge coupled device (CCD) camera, and a safety area is generated by plotting the outline of each sample and recording the points. This will define an area of safe travel for the indenter tip.

Electrostatic Force Constant and Zero Volt Gap Calibration

The electrostatic force constant is a conversion used by the Triboindenter to convert an applied voltage to a force. This constant is determined by the area of the plates and the distance between them squared. Because the center plate is suspended by springs, and different mass tips can be used, the plate gap spacing can change. The calibration procedure is as follows:

- A load of 600 uN is set in the load function editor. This load will displace the tip through a large range of motion.
- Perform advanced z-axis calibration is selected from the drop down menu.
- The plate is moved through its range of motion and a plot is generated of the electrostatic force calibration based on the spring constant and applied voltage versus displacement.
- The curve is fit to a quadratic and the equilibrium position of the plate is recorded and tared to zero and the calibration is complete.

Tip Optics Offset Calibration

All tests on the Triboindenter are set up on the sample using the optical CCD microscope camera. The computer then translates that area to the indenter tip to perform the test. Therefore a calibration procedure is needed to record the differences in the x, y, and z positions of the center of the optical focus and the indenter tip. The standard procedure developed by the OEM relies on residual indents large enough to image optically and works well in indentation applications with sharp, small radius tips. For tribological applications a blunt radius tip is often desired, so an alternate method had to be developed.

Standard tip optics offset procedure

As mentioned above, this optics offset procedure involves optically imaging residual indents. A relatively soft, polished sample is required for this procedure. A single crystal aluminum sample with [001] out-of-plane orientation is included with the

Triboindenter. This sample is mounted on the stage. The open loop load function editor is set with a maximum load of 10 mN. This load with a sharp tip of less than 5 μm radius will leave a residual indent that can be easily imaged with the optical CCD microscope. A safety zone is defined around the aluminum sample, and an area free of indents is chosen to perform the calibration. The optics offset procedure is chosen from the software menu, and the machine automatically translates the tip to the approximate position above the center of the optical focus. The user is prompted to use the z height control to lower the indenter tip to within 1 mm of the sample surface. Once the user does so, an automated pattern of seven indents in the shape of an H is performed on the sample at the prescribed load (Figure 4-2). The machine then translates the sample back to the optical microscope, and the user is prompted to set the microscope reticule over the center indent. The computer then records this difference in the x, y, and z positions of the center of optical focus and the indenter tip. Once this procedure is completed, an eighth indent is added to the pattern so not to confuse it with another pattern in a later tip optics offset calibration.

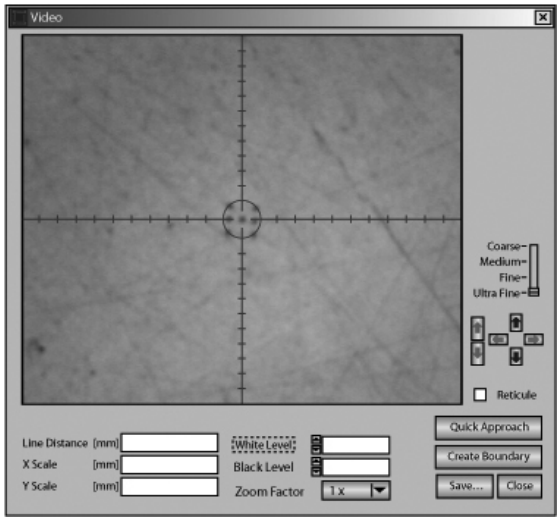

Figure 4-2. Optical CCD microscope image of residual H-pattern indents in Al (001) sample

Modified tip optics offset procedure

This procedure was developed for large radius tips where the residual indentation left by the maximum load would not be resolvable in the optical microscope. By calculating the depth δ of a residual impression left by a spherical indenter of radius R, one can see how indenters of sharp radii less than 5 μm leaves an impression that is resolvable by optical microscopy, but impressions from indenters of blunt radii greater than 100 μm cannot be resolved optically. Hardness was defined earlier as the normal load divided by the projected area of the residual impression. Figure 4-3 shows a schematic of a spherical indenter on a flat surface and the cross sectional geometry to solve for δ, the depth of impression, where F_n is the normal load, 2a is the diameter of the residual impression, 'a' is the radius of residual impression, and R is the radius of the indenter tip.

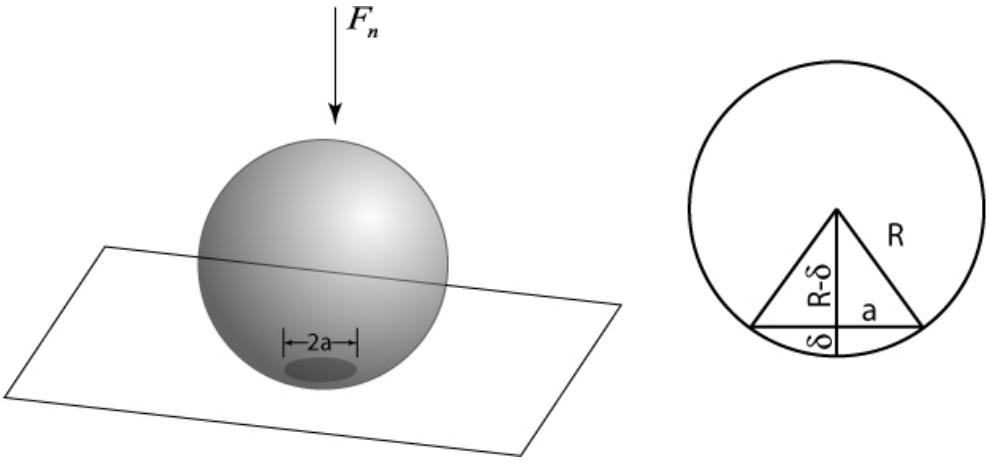

Figure 4-3. Representation of spherical indenter on flat surface and cross sectional geometry to solve for depth of indentation

The hardness equation can be rearranged as follows:

$$H = \frac{F_n}{A} = \frac{F_n}{\pi a^2} \rightarrow a = \sqrt{\frac{F_n}{H\pi}} \tag{4-1}$$

For the relatively soft aluminum sample, H = 500 MPa. With the machine set at the maximum load of 10 mN, solving for 'a' yields a = 2.5 μm. Using geometry from Figure 4-3, the following can be written:

$$\delta = R - \sqrt{R - a^2} \tag{4-2}$$

For tips of radius R = 5 μm, the depth of residual impression is 670 nm, which is within the limits of resolution in the optical microscope. Considering a tip of radius R = 100 μm, the depth of the residual impression is 30 nm which cannot be resolved in an optical microscope.

Fortunately, the Triboindenter has a scanning probe imaging feature which works much like an AFM in that the tip can be held in contact with a surface at a low load and the piezo tube scanner can raster the tip over the surface. At each point, or pixel, a z-height is recorded along with the x and y position of the tip. This data is used to generate an image by applying contrast values to the z-height values. This scanning feature has a resolution limit below 1 nm in the z direction because the capacitive transducer is used to record the z-height.

The following method was developed to work around the resolution limits of the optical microscope. This method uses a low load which can be beneficial in fields outside of tribology. If one were to design a delicate functional tip that could not survive the high load used in the standard optic offset procedure, yet still needed accurate tip positioning, the modified tip optics offset method could be employed.

Since a scanning probe technique would be used to calibrate the tip optics offset, a sample was designed and produced to contain features that would be easily imaged and located in both the optical CCD microscope and the scanning probe microscope feature

of the Triboindenter. A silicon wafer was chosen because of its highly polished surface, and its compatibility with the focused ion beam milling technique. The wafer was cleaved into a 5 mm x 5 mm section and mounted on a 12 mm AFM disk with a cyanoacrylate based adhesive. This specimen will now be referred to as the modified tip optics offset sample and is shown in Figure 4-4. The following features were carefully chosen and patterned on the wafer using an FEI DB-235 focused ion beam (FIB) SEM.

- series of concentric circles
- 200 μm outer diameter
- 20 μm radial spacing
- 40 μm inner diameter
- two sets of orthogonal crosshairs rotated 45º from each other
- 1 μm patterned line width

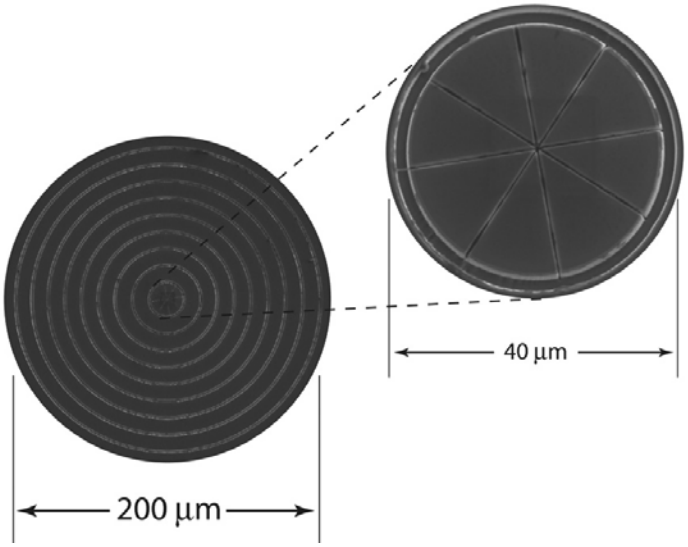

Figure 4-4. SEM image of the patterned modified tip optics offset sample

The series of concentric circles were chosen because it is easy to determine, from an arc, the direction of travel required to head towards the center. A pattern size of 200 μm outer diameter was chosen because it has been observed that from a tip change the tip optics offset rarely varied by more than 100 μm and a 200 μm feature is easily located in an optical microscope. When the scanning imaging function of the Triboindenter is

started, a rastering pattern of 40 μm x 40 μm is a typical scan size, therefore a radial spacing of 20 μm will ensure that at least one line is caught in the initial scan. The inner diameter of 40 μm was chosen because it could be imaged in the initial scan size once located. The two sets of orthogonal crosshairs rotated 45º from each other were chosen because if only one set was present, and one of the lines were aligned closely with the rastering direction, that line would not be imaged. The two sets ensure at least 3 of the 4 lines will be imaged. The reason for the 1 μm line width is two-fold. First, a line of 1 μm in width can be resolved in an optical microscope. For the second reason, we return to Figure 4-3 and Equation 4-2. Equation 4-2 can be rearranged and solved for 'a' to give:

$$a = \sqrt{R^2 - (R - \delta)^2} \tag{4-3}$$

From the geometry of Figure 4-3, 2a will be the minimum width of the line spacing required for a given R and δ. The largest radius tip of interest in this study is R = 250 μm. Hysitron publishes the z axis resolution limit to be 0.04 nm with a noise load floor of 0.2nm. A value of δ = 0.5 nm should be within the resolution of the equipment. Using these values in Equation 4-4 gives a value for a = 0.5 μm, making the line width 2a = 1 μm.

If a FIB is not available, a similar tip optics offset sample could be produced using a soft polished sample such as the Al (001) and a sharp indenter tip. Using the automated methods feature of the Triboindenter, one could set up a similar pattern to that described above and run the pattern with a sharp tip, high load, and a soft sample. Once the sample is produced, the sharp tip can be exchange for a blunt tip and the modified tip optics offset procedure could be followed.

Once the modified tip optics offset sample is produced and mounted on the stage with a safety limits area defined, the blunt tip installed on the capacitive transducer, and the electrostatic force calibration and zero volt gap calibration completed, the modified tip optics offset procedure is initiated. The sample's concentric rings are located and centered to the video window reticule using stage translations (Figure 4-5).

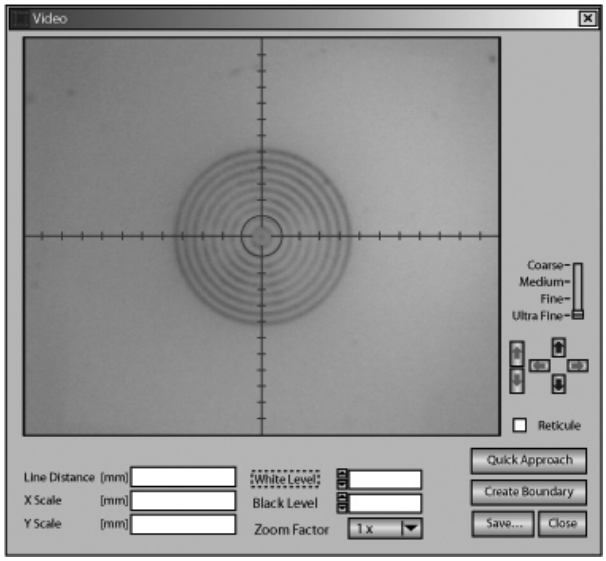

Figure 4-5. Modified tip optics offset sample centered in the video window

From the main positioning window, tip optics offset is selected. Then new 'single indent' is selected from the window seen in Figure 4-6.

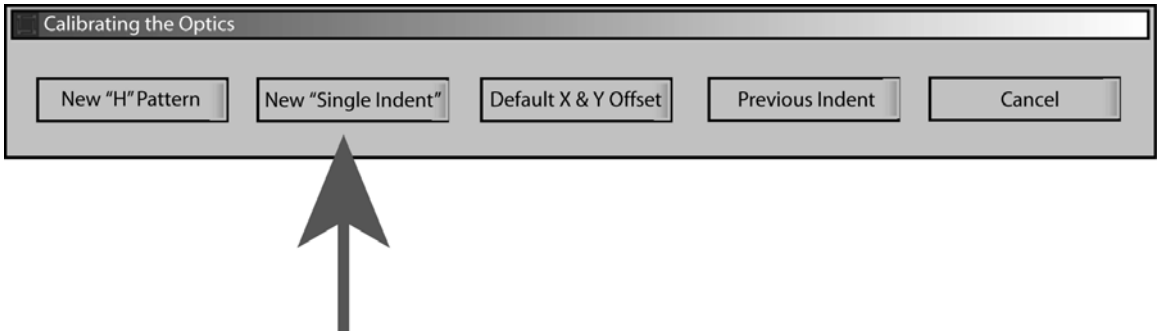

Figure 4-6. At this point, new single indent is selected

In the load function editor, a low load of 2 μN or less is programmed. By setting a low load, the machine will go through the standard procedure of performing an indent, but no

damage to the sample or the tip will occur. The machine will translate the sample so that the tip is over the sample and the user will be prompted by the window in Figure 4-7.

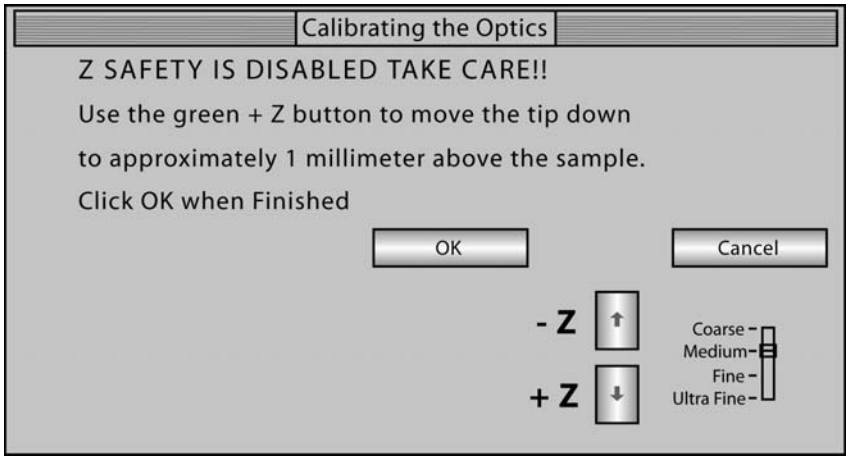

Figure 4-7. Manual height adjustment window

From this window the indenter tip is lowered to approximately 1 mm from the sample surface. The machine then slowly approaches the sample surface until contact is made, and the low load indent is executed. The sample is then translated back to the optical CCD microscope and the window in Figure 4-8 pops up.

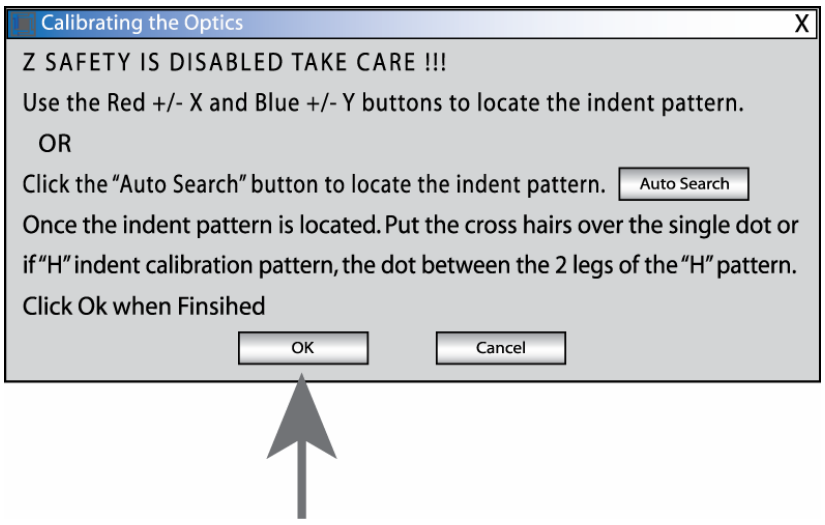

Figure 4-8. Search option window

At this point, no translation is made even though the machine prompts the user to locate the pattern. This set is used only to set the z-axis offset. The x and y offset is set

in following steps. The 'ok' button is pressed without any x or y translation. Now from the Triboscan toolbar, the imaging mode is selected. The windows in Figure 4-9 will open. Initial scan parameters of 50-80 μm scan size, 2 μN set point, and 1 Hz scan rate are entered. Topography and gradient imaging windows are selected.

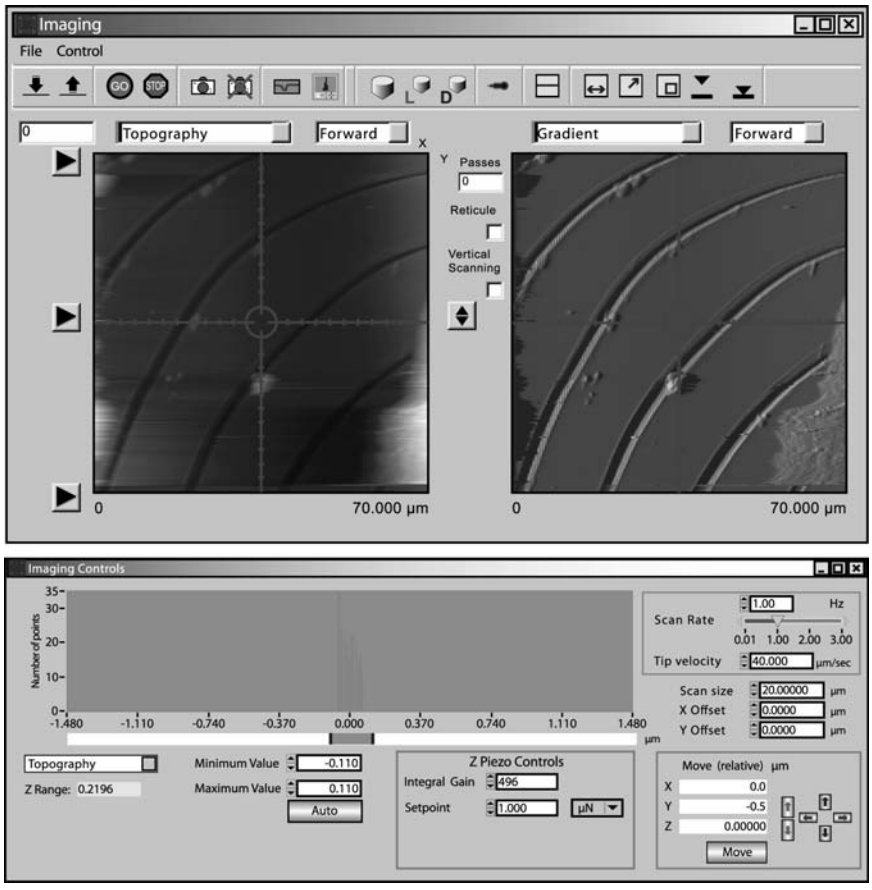

Figure 4-9. Imaging window and control panel with image of modified tip optics offset sample

Tip approach is selected and once the Triboindenter has indicated that the tip is in contact with the surface, the scanning is started. Once one complete raster is finished, some of the tip optics offset sample should be visible. Now the stage controls are used to translate the sample towards the center of the circles. It is critical to use only the stage controls and not the x-y offset to translate the sample. The x-y offset is a bias applied to the piezo tube scanner which will give an inaccurate tip optics offset calibration if used

here. Determining the direction for translation is easily identified by moving radially inward from the patterned arcs. For translation it is easiest to think of the sample being stationary and the reticule moves in the direction indicated on the x-y translate arrows. Relative direction lengths can be entered and are convenient for 'homing-in' on the center. As the center is approached, the raster size is reduced which effectively zooms in on the image. Once the center of the sample is located on the imaging reticule, the tip is withdrawn from the sample and the sample is translated automatically back to the optics window. Now the amount of tip optics offset can be visualized in the video window (Figure 4-10).

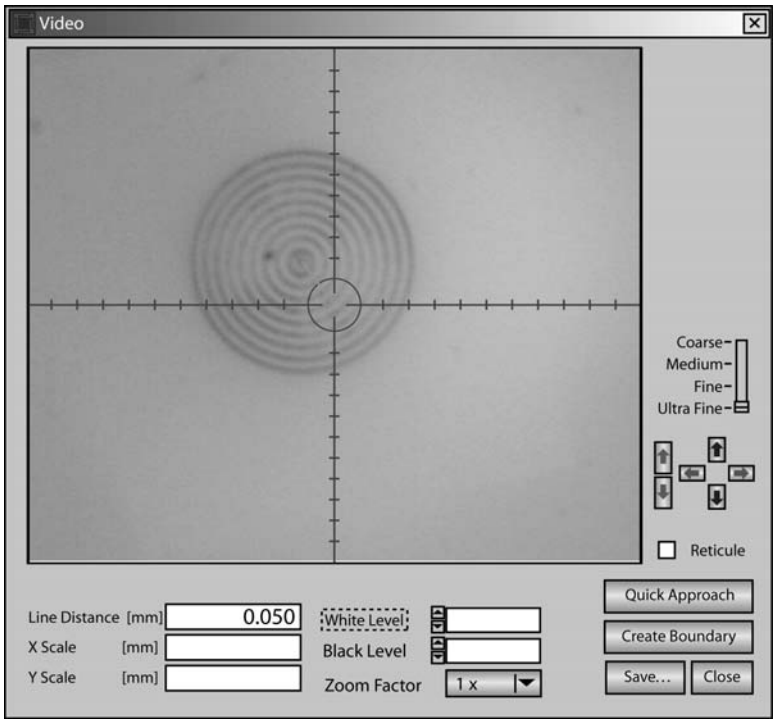

Figure 4-10. Actual tip optics offset seen in the video window

No stage translations are made at this point. Again calibrate optics is selected from the drop down menu, and the window in Figure 4-6 appears. New single indent is selected again and a low load is entered in the load function editor window. The sample

is automatically translated beneath the indenter tip, and the window in Figure 4-7 appears again. The tip is manually lowered to within 1 mm of the surface and the machine performs the low load indent. Upon completion, the sample is translated back to the optical CCD microscope and the auto search window seen in Figure 4-8 reappears. Now stage translations are used to center the tip optics offset sample pattern to the center of the video window reticule, and the 'ok' button is pressed in the auto search window. The calibration is now complete and can be checked by returning to the scanning imaging mode to verify the pattern is at the center of the imaging reticule. This entire procedure was completed with no load greater than 2 μN.

Quick Approach

Now that all calibrations are complete and the samples are mounted with safety zones defined, an area of interest is located using grid lines etched by the FIB. A "quick approach" is performed which involves setting a load threshold and approaching the sample surface. Once the load threshold, called the "set point" is reached, the Triboindenter records the z height as the sample height. This procedure is performed for each sample safety area.

Tip Area Function Calibration

With depth sensing indentation machines, load and displacement are measured, however, an area of residual impression is necessary for analysis of modulus and hardness as can be seen in Equation 4-1. From the analysis above, it is shown that a residual impression cannot be imaged or measured optically. It would be convenient to be able to extract area calculations based on displacement data. Therefore a tip area function relating the residual area to the depth of indentation is needed. For micron and larger scale indentation depths, ideal tip geometry can be assumed and an area function

can be generated from simple geometric relationships. The ideal area function for an indenter with pyramidal Berkovich geometry is $A=24.5*h_c^2$ where h_c is the contact depth and A is the residual area (see Data Analysis section for in-depth explanation). At the nanometer level, the tip of a pyramidal indenter is rounded, therefore the assumption that the three faces of a pyramid intersect at a point is invalid, and the ideal area function breaks down and greatly underestimates the residual area based on the depth. A method has been devised to generate a tip area function by creating a series of indents in a standard of known elastic modulus. In this section, the mechanics of generating a tip area function are explained. For a detailed mathematical description of the procedure, refer to the Data Analysis section.

A fused quartz standard is loaded on the stage of the Triboindenter. A series of approximately 100 indents are made targeting a depth range to cover the series of experiments to be run. The series is run and the data is saved. A power law curve fit is performed on the unloading portion of the curves. A tangent line to the power law curve is used to find the stiffness from which an area is calculated. The calculated area versus displacement for all the indents is plotted, and a curve fit is performed to generate an area versus displacement function. This function is saved for this tip and displacement range. A new function must be generated for each different tip and the functions must be verified periodically on a standard to ensure the tip geometry has not changed.

Machine Compliance Calibration

In a depth sensing indentation device, the desired measurement is the position of the tip relative to the sample surface. This is determined by displacement, however measured displacements include compliance of the system along with the tip and the sample.

There are several factors that can contribute to the system compliance such as:

- Indenter tip—the indenter tips are handmade from various materials and adhesives.
- Sample mounting—if the sample mounting procedure varies in materials, the compliance will vary.
- Transducer mounting—the transducer must be mounted the same way each time and should be level and properly seated.

Therefore it is necessary to determine the system compliance and remove it from the measurements. This section only explains the procedure for the compliance calibration. The mathematics are explained in detail in the Data Analysis section.

Once the other procedures have been completed, the transducer calibration constant is set so that the machine compliance is 0.00. A set of 15 indents are made with loads varying from 5 mN to 10 mN. Curves from the data are ploted and the multiple file analysis is executed. A plot is generated of the inverse of the stiffness versus the inverse of the square of the load. A linear fit is generated and the machine compliance in nm/mN is equal to the y-intercept times 1000. This number is entered for machine compliance. A new machine compliance is generated for each tip and any time the conditions mentioned above might change.

Testing Modes

The Triboindenter has three basic modes of operation which are illustrated in Figure 4-11. The static indentation mode brings the tip into contact with the surface, applies a normal load, and records load and displacement. The scratch mode brings the tip into contact, applies a normal load, translates the tip laterally, and records normal load, normal displacement, lateral load, and lateral displacement. The rastering wear test mode applies a normal load, and uses the piezo tube scanner to raster the tip over an area. No quantitative data except the prescribed normal load is collected in this test.

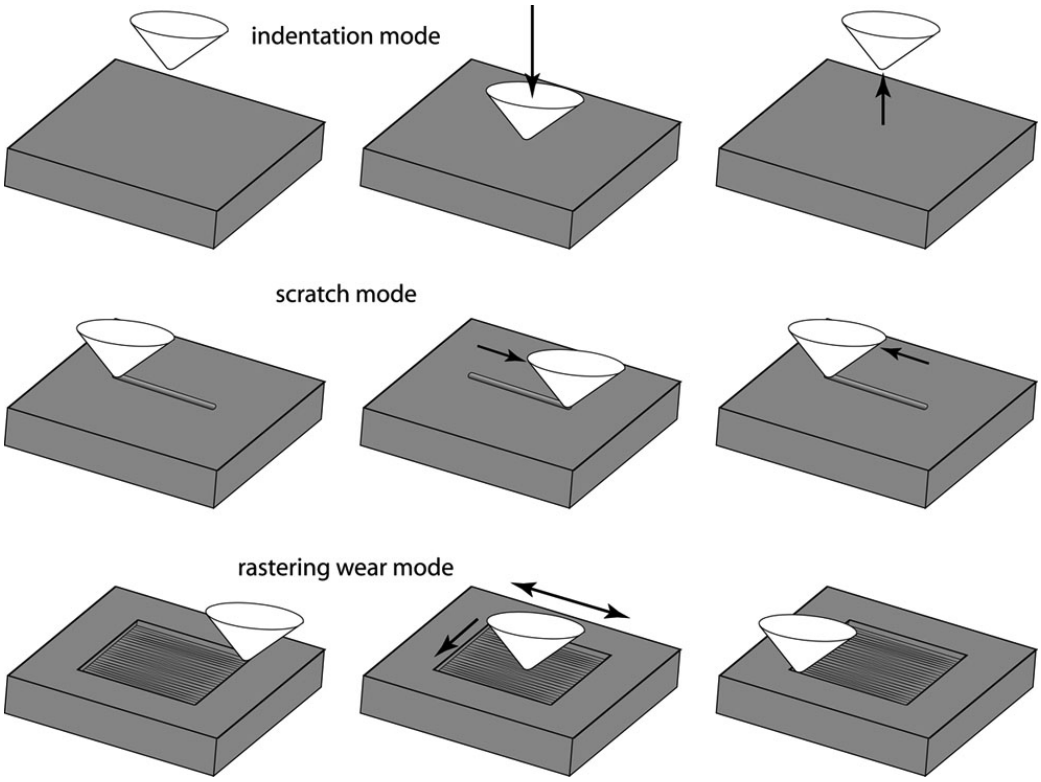

Figure 4-11. Schematic illustration of Triboindenter testing modes.

Depth sensing indentation

Depth sensing indentation tests yield data in the form of loads and displacements which can be analyzed to obtain material properties such as elastic modulus and hardness as described in the data analysis section. Once the calibrations have been completed, load versus displacement versus time functions are generated in the load function editor. The area of interest is located, and the test is initiated. Indentation tests can be operated in load control, displacement control, or open loop where a DC bias voltage is set based on the electrostatic force calibration to approximate a maximum load. Once the test is started, the tip approaches the surface and makes contact at the set point. The load is increased and load, displacement, and time are recorded. A general 'rule of thumb' has been established for testing thin films on substrates which suggests maximum indentation

depth should not exceed 10% of the film thickness to avoid a contribution from the substrate properties.

Rastering wear test

For data analysis, fiducial marks are placed using the indentation mode prior to running the test. An automated pattern of eight indents surrounds the test area (Figure 4-12). An atomic force microscope AFM scan of this area with the fiducial marks is necessary prior to testing. In this test, a normal load is prescribed in the wear function editor along with an area to raster over and a scan rate. The number of raster lines is set at 256. The area of interest is selected in the optical CCD microscope. Once the test is started, the tip approaches and contacts the surface, applies the desired load, and the piezo rasters the tip over the prescribed area for a given number of cycles.

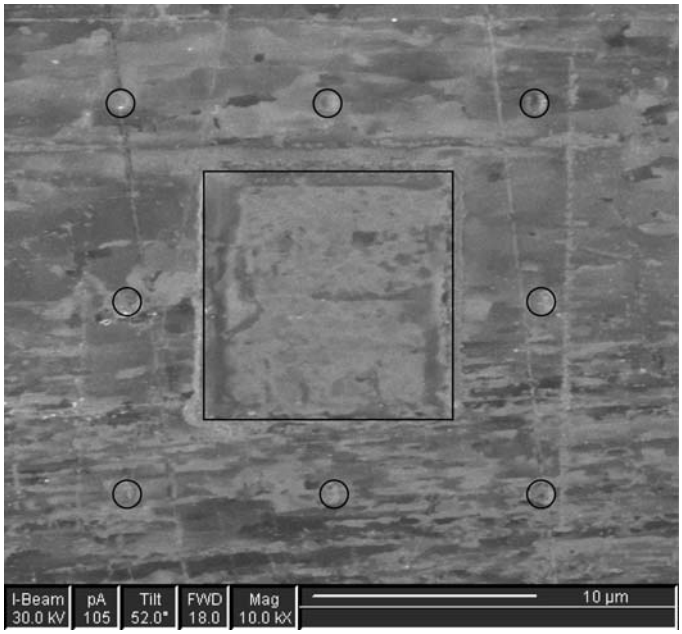

Figure 4-12. SEM image of a rastering wear test showing fiducial indentation marks in circles.

Reciprocating Wear Test

The scratch test mode is modified to replicate a reciprocating linear tribometer. This mode was originally designed to place a normal load on the tip, and using the 2D transducer, translate the tip to produce a scratch. The test mode is often employed for testing relative coating adhesion. By using this method with a low normal load, and programming multiple passes in the function editor, a nanodisplacement scale reciprocating tribometer is emulated.

CSM Microtribometer

Tip Preparation

Tips on the CSM Microtribometer were mounted on the cantilever flexure using a cyanoacrylate based adhesive [22] (Figure 4-13). The tips are commercially available BK7 optical glass lenses with a semi-spherical geometry.

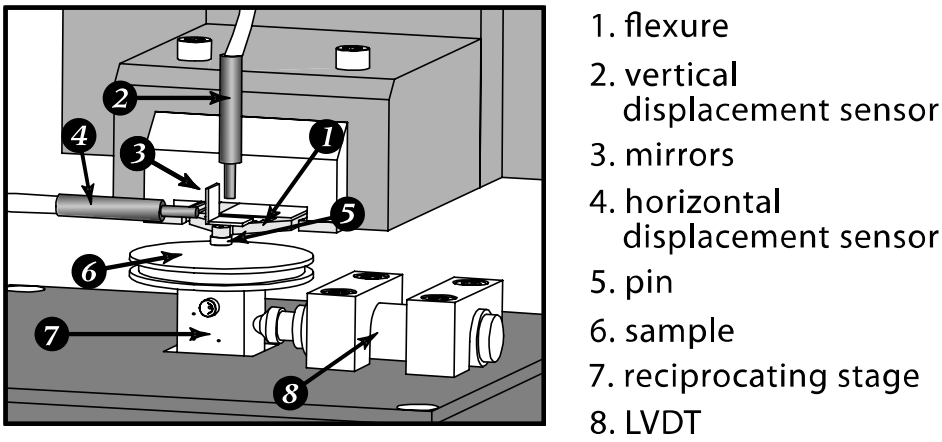

Figure 4-13. Schematic of the CSM Microtribometer.

Sample Mounting

The sample is mounted on a SEM microscope stub using a cyanoacrylate based adhesive. The SEM stub is fixed to the linear reciprocating stage. Stepper motors are used for coarse positioning of test area with the aid of a portable microscope.

Reciprocating Wear Test

The Microtribometer has a normal load range of 0.5 mN – 1 N. This range of applied normal loads is achieved by having three different types of dual flexures, with varying stiffness values. Low range normal loading (0.5-100 mN) is achieved with a glass flexure, middle range loading (50 mN-300 mN) is achieved with a stainless steel flexure, and high range loading (200 mN-1N) is achieved with a thicker stainless steel flexure. The appropriate flexure for the desired load range is selected, and the testing parameters of normal load, track length, sliding speed, and sampling rate are entered in the computer. The machine records lateral load and lateral position. From this data, friction coefficient and sliding speed can be calculated.

CHAPTER 5
DATA ANALYSIS

Indentation Testing

Indentation testing is a convenient, relatively non-destructive method to determine mechanical properties such as hardness and elastic modulus. Hardness is defined as:

$$H = P / A \tag{5-1}$$

where P is the normal load and A is the projected residual area in the direction of the load. Microhardness tests are typically performed by applying a known load and calculating the area of the residual indent from measurements taken in an optical microscope. Nanoindentation has been defined as tests involving normal displacements on the order of nanometers [23]. Residual indents from tests at this scale have dimensions smaller than the resolution limits of optical microscopy and would require electron microscopy for measurements. Since electron microscopy is costly and time consuming, requiring a subsequent characterization of the sample, post-indentation, methods have been developed to calculate the residual area based on a measured depth of indentation.

The Oliver-Pharr Method

The most widely accepted method for depth sensing nanoindentation analysis involves a model first proposed by Doerner and Nix and later refined by Oliver and Pharr [24, 25]. This analysis is often referred to as the Oliver and Pharr Method. Once load and displacement data has been collected and plotted as shown in Figure 5-1, a power law curve fit of the form:

$$P = A(h - h_f)^m \tag{5-2}$$

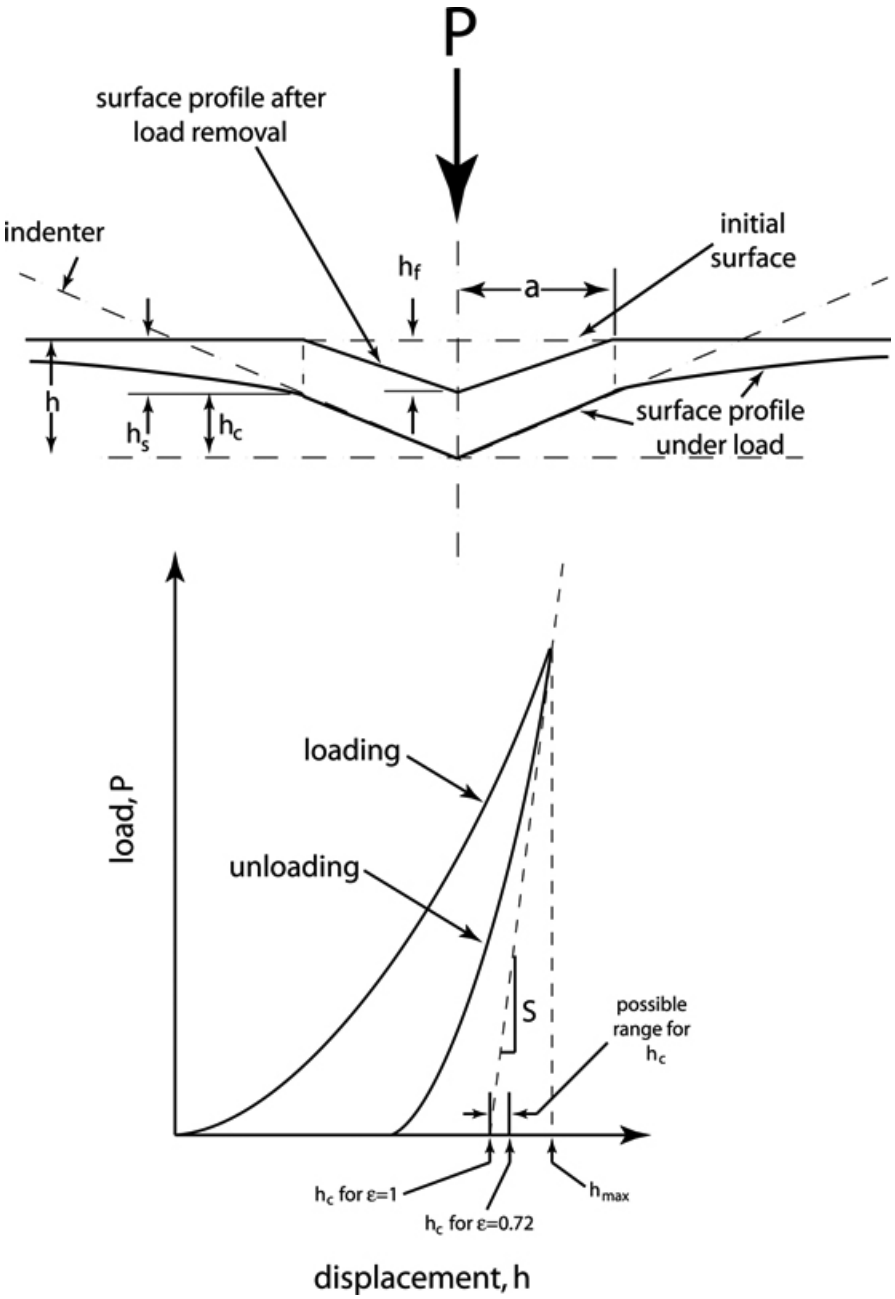

Figure 5-1. Schematic of load versus displacement curve along with a cross section of an indented surface. The range of ε is indicated for various indenter geometries.

where P is the load, h is the depth and h_f is the depth of the residual impression, is fit to the unloading portion of the data. Sneddon derived the following equation to describe the

load as a function of displacement for an infinitely rigid cylindrical flat punch into an elastic half-space:

$$P = \frac{4Ga}{1-\nu} h \tag{5-3}$$

where P is the load, G is the shear modulus, a is the radius of the cylinder, h is the depth of penetration, and ν is the Poisson ratio [26]. By substituting:

$$G = \frac{E}{2(1+\nu)} \tag{5-4}$$

for G, Equation 5-3 becomes:

$$P = \frac{2Ea}{(1-\nu^2)} h \tag{5-5}$$

Rearranging the equation for the area of contact of the indenter to:

$$a = \frac{\sqrt{A}}{\sqrt{\pi}} \tag{5-6}$$

and substituting, Equation 5-5 becomes:

$$P = \frac{2}{\sqrt{\pi}} \sqrt{A} \frac{E}{(1-\nu^2)} h \tag{5-7}$$

and differentiating with respect to h yields:

$$\frac{dP}{dh} = \frac{2}{\sqrt{\pi}} \sqrt{A} \frac{E}{(1-\nu^2)} \tag{5-8}$$

where dP/dh is, by definition, the stiffness.

One must now consider the elastic properties of the indenter. Defining the modulus of the system as the reduced modulus E_r yields:

$$\frac{1}{E_r} = \frac{(1-\nu_s^2)}{E_s} + \frac{(1-\nu_i^2)}{E_i} \tag{5-9}$$

where E_s and ν_s are the Young's modulus and Poisson ratio for the indented surface and E_i and ν_i are the Young's modulus and Poisson ratio for the indenter. Substituting into Equation 5-8 yields:

$$\frac{dP}{dh} = \frac{2}{\sqrt{\pi}} \sqrt{A}\, E_r \tag{5-10}$$

Solving for E_r gives:

$$E_r = \frac{\sqrt{\pi}}{2\sqrt{A}} S \tag{5-11}$$

Oliver, Pharr, and Brotzen have shown that this equation holds true for any axisymmetric indenter, and will extend to pyramidal indenters with a correction factor, ε, for different geometries [27]. A function to describe contact area from displacement along with Equation 5-11 gives a convenient method to measure the reduced modulus from data shown in Figure 5-1. The Poisson ratio of the material of interest is often unknown, therefore reduced modulus rather than Young's modulus is often reported.

For a Berkovich indenter of ideal geometry, the relationship between contact area and contact depth can be calculated from simple geometry:

$$A = 24.5\, h_c^{\,2} \tag{5-12}$$

However, due to the inability to produce a perfectly sharp indenter, some radius is expected at the tip apex. For large indents, this radius is negligible, but for nano-displacements, it cannot be neglected. An area function to relate contact area as a function of contact depth can be generated by indenting on a fused quartz sample of know elastic modulus, E = 72 GPa. A series of indentation tests of increasing displacement over the desired range are run on the standard sample. Load versus

displacement plots are generated to find the stiffness as described above. By solving for h_c from the relationship in Figure 5-1:

$$h_c = h_{\max} - \varepsilon \frac{P_{\max}}{S} \tag{5-13}$$

and Equation 5-10 solved for area and plotting A_c versus h_c, a curve fit is generated in the form:

$$A_c(h_c) = C_0 h_c^{\,2} + C_1 h_c + C_2 h_c^{1/2} + C_3 h_c^{1/4} + C_4 h_c^{1/8} + C_5 h_c^{1/16} \tag{5-14}$$

Indentation testing data can now be analyzed from eqn. 5-1 and 5-11 to obtain hardness and reduced modulus. The Oliver and Pharr method includes the following assumptions:

- Material does not pile-up outside the indent.
- The unloading behaves as an isotropic elastic half-space.
- The tip area function is well approximated over the range of displacements.

Compliance Method (Stone's Method)

When designing mechanical testing equipment, engineers choose stiff materials to reduce the effect of machine compliance upon sample data, however, machine compliance cannot be ignored. Compliance is defined as the inverse of stiffness. Compliance of the entire system, C_T, can be written as:

$$C_T = C_m + C_s \tag{5-15}$$

where C_m is the compliance of the load frame (machine) and all other compliances except the sample, and C_s is the compliance of the sample. The load frame compliance includes sample mounting, tip, frame, and stage. The following method is suggested by Hysitron to determine the compliance of the machine [28]. The inverse of Equation 5-10 can be substituted in Equation 5-15 for C_s to give:

$$C_T = C_m + \frac{\sqrt{\pi}}{2E_r\sqrt{A}} \tag{5-16}$$

solving Equation 5-1 for area and substituting yields:

$$C_T = C_m + \frac{\sqrt{\pi H}}{2E_r\sqrt{P_{\max}}} \tag{5-17}$$

Assuming hardness is constant at large indentations, a series of large indents can be run and plotting the inverse of the total measured compliance versus $1/P_{max}$ will give y-intercept equal to C_m. This method can be run on various mounting techniques and different tips to determine the compliance for any given testing conditions. Figure 5-2 shows a plot of the total compliance measured versus the inverse of the square root of the maximum load for various large loads on a quartz standard, an aluminum standard, and a (001) silicon wafer.

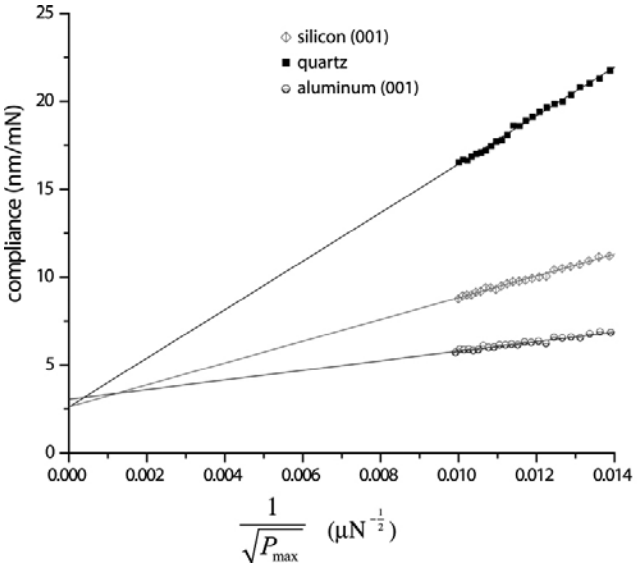

Figure 5-2. Measured compliance versus square root of maximum load for a load range of 5mN to 10mN on quartz, Al (001), and Si (001).

A least squares fit line is generated to determine C_m. Both the quartz standard and the silicon sample show good agreement in the machine compliance of 2.6 nm/mN. The

aluminum sample shows a slightly higher compliance of 3.0 nm/mN which may be attributed to differences in sample mounting.

A similar yet alternative method to analyze machine compliance and extract hardness and modulus information has been developed by Stone et al. [29]. Stone et al. begin by defining a material compliance parameter:

$$J_0 = P_{\max} C_s^2 = \frac{H}{E_r^2} \tag{5-18}$$

where P_{max} is the maximum load, C_s is the compliance of the sample, H is the hardness of the sample, and E_r is the reduced modulus. Note that the parameter J_0 is independent of the tip geometry. This parameter was originally developed by Joslin and Oliver [30] who noted that by substituting for the definition of hardness from Equation 5-1 and stiffness from Equation 5-11, one could obtain:

$$\frac{H}{E_r^2} = \frac{4}{\pi}\frac{P_{\max}}{S^2} \tag{5-19}$$

Stone's parameter is missing the $\pi/4$ term from Joslin and Oliver's analysis. This $\pi/4$ term arises from the geometry in Sneddon's [26] analysis of the cylindrical punch, which Pharr et al. have shown to apply to any axis symmetric indenter [27]. Stone incorporates a geometrical factor in his E_r term which is adjusted depending on tip geometry to account for the $\pi/4$ term. The indenter used in this study is modeled as an axisymmetric indenter and no geometrical term is incorporated in the reduced modulus; therefore a parameter will be substituted in Stone's analysis to better fit this study. This parameter, K_0, is defined as:

$$K_0 = P_{\max} C_s^2 = \frac{\pi}{4}\frac{H}{E_r^2} \tag{5-20}$$

By taking Equation 5-15 and multiplying by the square root of P_{max} yields:

$$C_T\sqrt{P_{\max}} = C_m\sqrt{P_{\max}} + C_s\sqrt{P_{\max}} \tag{5-21}$$

and substituting for the material parameter:

$$C_T\sqrt{P_{\max}} = C_m\sqrt{P_{\max}} + \sqrt{K_0} \tag{5-22}$$

Now plotting the $C_T P_{max}^{½}$ versus $P_{max}^{½}$ yields a line with a slope of the machine compliance and an intercept of $K_0^{½}$ provided the material shows no indentation size effect. This analysis is useful in that the material parameter can be verified for the calibration standard and material data can be extracted without knowing the indenter tip geometry. Just as in the Oliver and Pharr analysis, the unloading is assumed to behave as an isotropic elastic half-space.

Modified Winkler Method

The Oliver and Pharr model works well on materials that do not exhibit significant pile-up. However, their model greatly overestimates hardness and modulus in materials that exhibit pile-up due to the underestimation of the contact area [31-33]. This overestimation of properties is amplified in soft thin films on hard substrates due to excessive pile-up. The compliance method of Stone et. al. extracts a material parameter that requires knowledge of either the hardness or the modulus to determine the other. The Stone model also assumes no indentation size effect.

An alternate model is developed based on the Winkler model of a bed of independent springs to account for material pile-up. Figure 5-3 shows schematic representations of indent cross sections from the Oliver-Pharr model, the modified Winkler model, and the output from an actual indent in a material exhibiting pile-up.

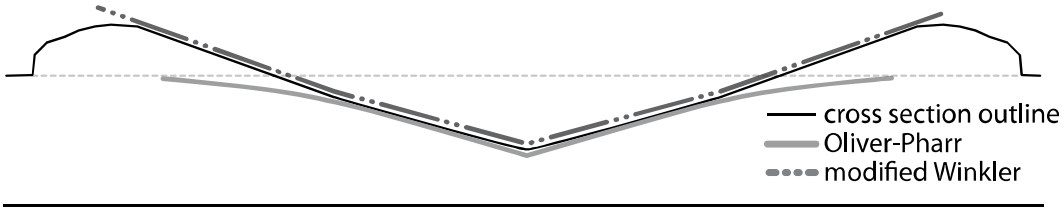

Figure 5-3. Schematic illustration of indent cross sections from Oliver-Pharr and Modified Winkler compared to an actual indent.

It is assumed that each differential element is constrained orthogonal to the loading direction due to surrounding material. The justifications for this assumption are the contact area radius is much larger than the film thickness and the Poisson ratio of gold is 0.42 which is nearly incompressible. The indenter tip is assumed to have axisymmetric geometry and is modeled based on a curve fit to a 4^{th} order polynomial from micrographs (see Chap. 6). To account for pile-up and plastic deformation neglected in the Oliver and Pharr model, each discretized element is examined to determine the onset of plastic deformation based on the hardness. Upon plastic deformation, the volume deformed is transferred to the next differential element. Once the maximum displacement is reached, elastic unloading is assumed. This model is developed to attempt curve fits with load versus displacement data collected from the nanoindenter.

The first assumption of constraint due to the surrounding material and the indenter tip/displacement scale results in no elastic strain in the directions orthogonal to the loading direction such that $\varepsilon_{xx}=\varepsilon_{yy}=0$. From this assumption, and effective modulus can be calculated from:

$$\{\varepsilon\} = [S]\{\sigma\} \tag{5-23}$$

where ε is the strain, S is the compliance matrix, and σ is the stress. Expanding yields:

$$\begin{pmatrix} \varepsilon_x \\ \varepsilon_y \\ \varepsilon_z \\ \gamma_{yz} \\ \gamma_{zx} \\ \gamma_{xy} \end{pmatrix} = \begin{pmatrix} \frac{1}{E} & \frac{-\nu}{E} & \frac{-\nu}{E} & 0 & 0 & 0 \\ \frac{-\nu}{E} & \frac{1}{E} & \frac{-\nu}{E} & 0 & 0 & 0 \\ \frac{-\nu}{E} & \frac{-\nu}{E} & \frac{1}{E} & 0 & 0 & 0 \\ 0 & 0 & 0 & \frac{1}{G} & 0 & 0 \\ 0 & 0 & 0 & 0 & \frac{1}{G} & 0 \\ 0 & 0 & 0 & 0 & 0 & \frac{1}{G} \end{pmatrix} = \begin{pmatrix} \sigma_x \\ \sigma_y \\ \sigma_z \\ \tau_{yz} \\ \tau_{zx} \\ \tau_{xy} \end{pmatrix} \tag{5-24}$$

where E is the Young's modulus. Solving for the stiffness and assuming no shear coupling yields:

$$C = S^{-1} = \frac{1}{(1+\nu)(1-2\nu)} \begin{pmatrix} E(1-\nu) & -E\nu & -E\nu \\ -E\nu & E(1-\nu) & -E\nu \\ -E\nu & -E\nu & E(1-\nu) \end{pmatrix} \tag{5-25}$$

The assumption of no strain in the x and y directions:

$$\{\varepsilon\} = \begin{pmatrix} 0 \\ 0 \\ \varepsilon_z \end{pmatrix} \tag{5-26}$$

can be substituted into:

$$\{\sigma\} = [C]\{\varepsilon\} \tag{5-27}$$

which yields:

$$\sigma_z = \frac{E(1-\nu)}{(1+\nu)(1-2\nu)} \varepsilon_z \tag{5-28}$$

The coefficient:

$$\frac{E(1-\nu)}{(1+\nu)(1-2\nu)} = \lambda \tag{5-29}$$

is Lame's constant and can be thought of as an 'effective modulus.'

Each element of the model film is described in cylindrical coordinates as illustrated in Figure 5-3. For the illustration, the tip geometry is shown as spherical; however, for calculations, the 4th order polynomial fit from micrographs of the tip characterization in Chapter 6 is used.

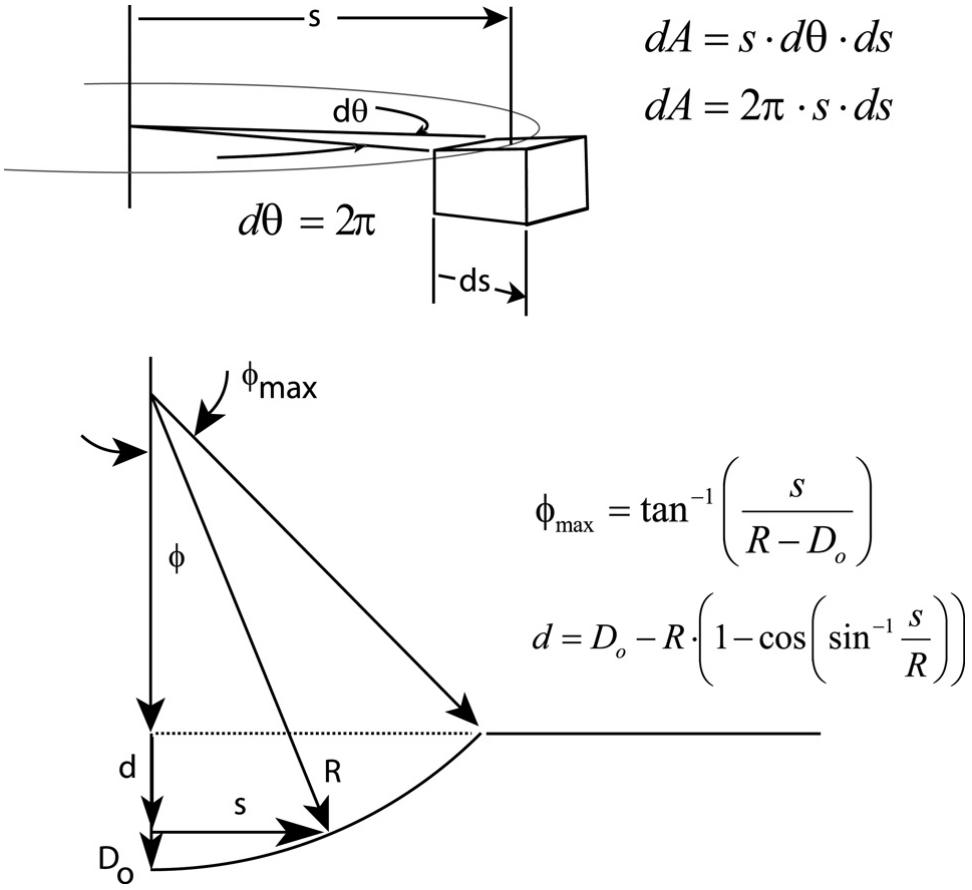

Figure 5-3. Schematic illustration of a differential element described with cylindrical coordinates and tip displacement based on a spherical tip geometry.

A MATLAB® code is developed to increment tip displacement and calculate differential element elastic-plastic response sequentially. Figure 5-4 shows the variable designations for the loading and unloading response.

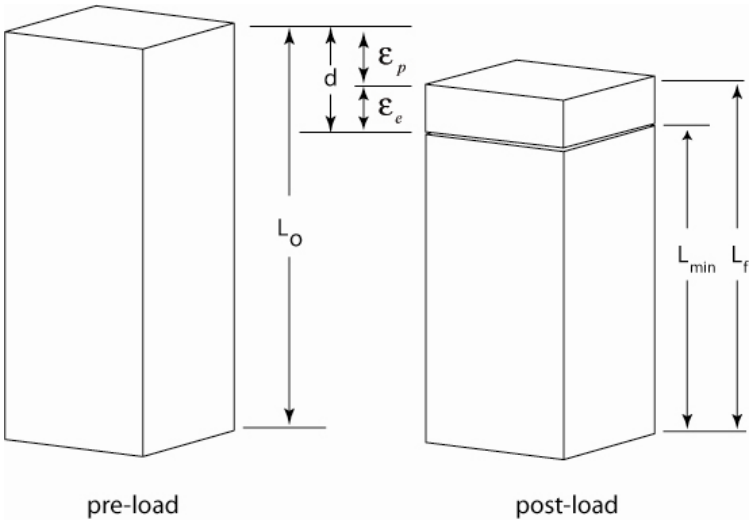

Figure 5-4. Differential element illustration prior to (left) and after load (right) with variable notation indicated.

At each displacement increment, the stress on each element is calculated by:

$$\sigma = \lambda \frac{\delta}{L_0} \tag{5-30}$$

where σ is the stress, λ is the effective modulus, δ is the incremented displacement, and L_0 is the film thickness. The incremental load is calculated by:

$$dF = \sigma dA \tag{5-31}$$

If σ=H, the hardness, the amount of volume from that incremental displacement over the differential element is transferred to the next element in the outward radial direction. The force is summed and the total displacement is compared to the maximum displacement. The displacement is incremented until the maximum displacement is reached, upon which, the unloading cycle begins. The loading code is represented in the flow chart in Figure 5.5.

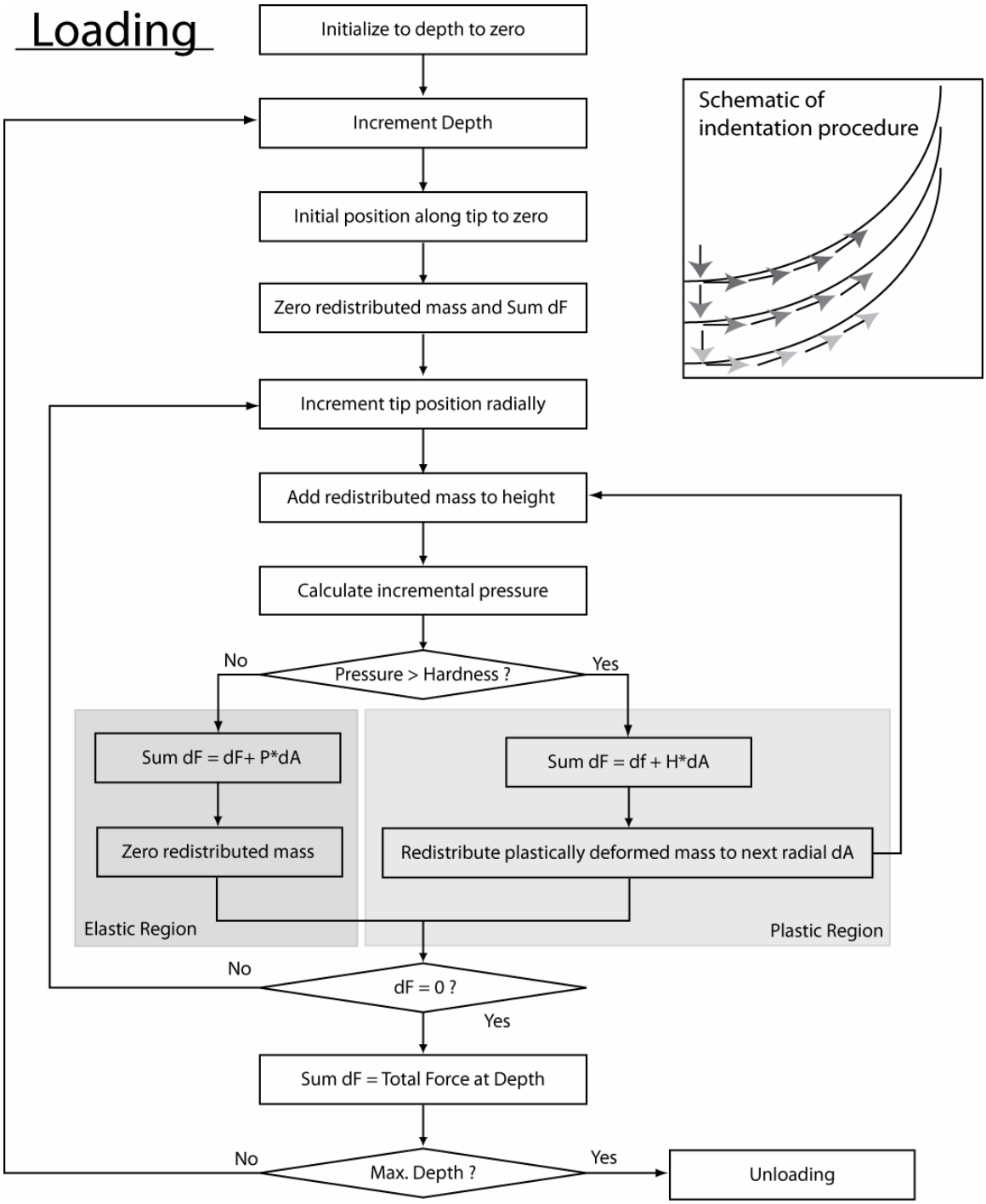

Figure 5-5. Flow chart diagram of loading code.

The unloading is assumed to be elastic. Each element begins compressed to the point L_{min} in Figure 5-4. The material will only recover to the point L_f. Figure 5-6 shows a flow chart of the elastic unloading code.

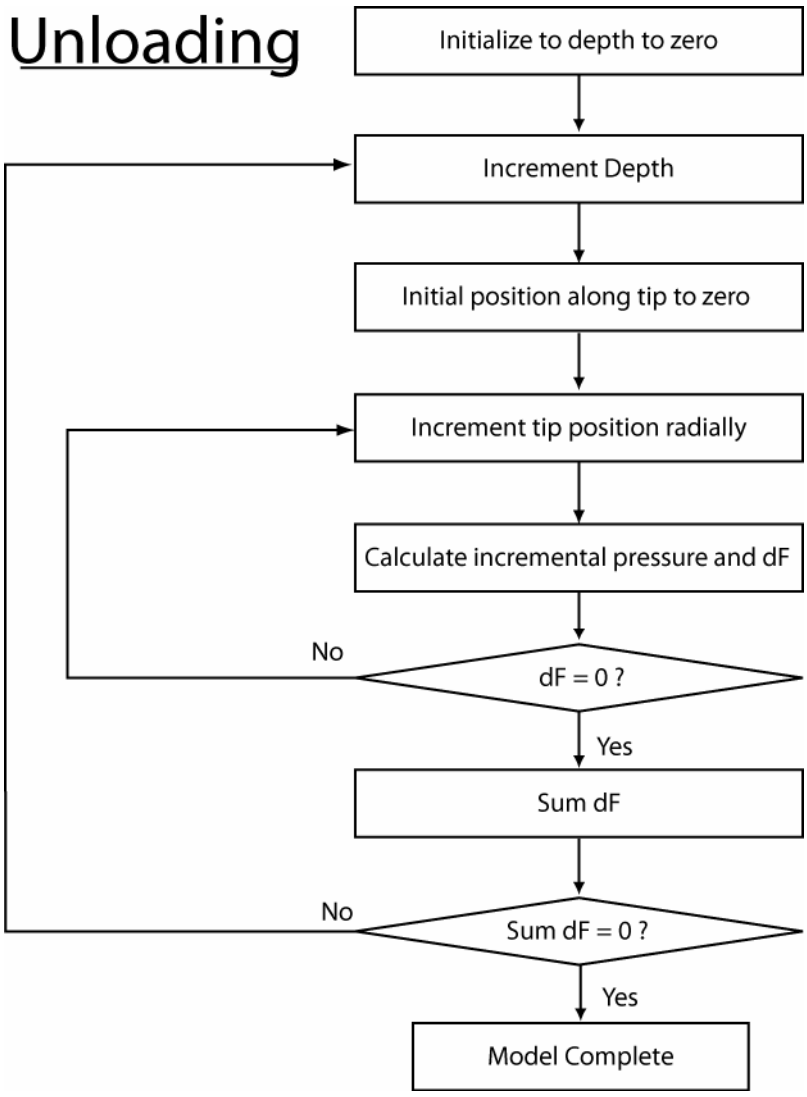

Figure 5-6. Flow chart of unloading code.

Rastering Wear Test

In the rastering wear test mode, no data is collected during the test by the Triboindenter. The input normal load is the only quantitative information available without subsequent analysis. Often in wear testing, a wear rate is reported to quantify the material performance. The wear rate, K, is the volume of material removed per normal load per distance of sliding. The normal load is the input parameter of the test, and the distance of sliding can be calculated by the square root of the area rastered over times

256, the number of raster lines, times the number of passes over the raster area. The volume can be calculated in the following manner:

- Fiducial marks are placed around the area to be worn prior to testing.
- An area larger than the test area is scanned in the AFM to include the fiducial marks.
- The desired rastering test area is run for a given load and number of passes.
- The larger area including the fiducial marks is again scanned with the AFM.
- The digitized data from the final scan is aligned to the data from the initial scan using the fiducial marks.
- The initial surface is then subtracted from the final surface.
- The data below the zero surface plane is integrated to calculate a volume of material removed.

This volume can now be used in the wear rate calculation. The subtracted data can be plotted to reveal wear morphology as shown in Figure 5-7.

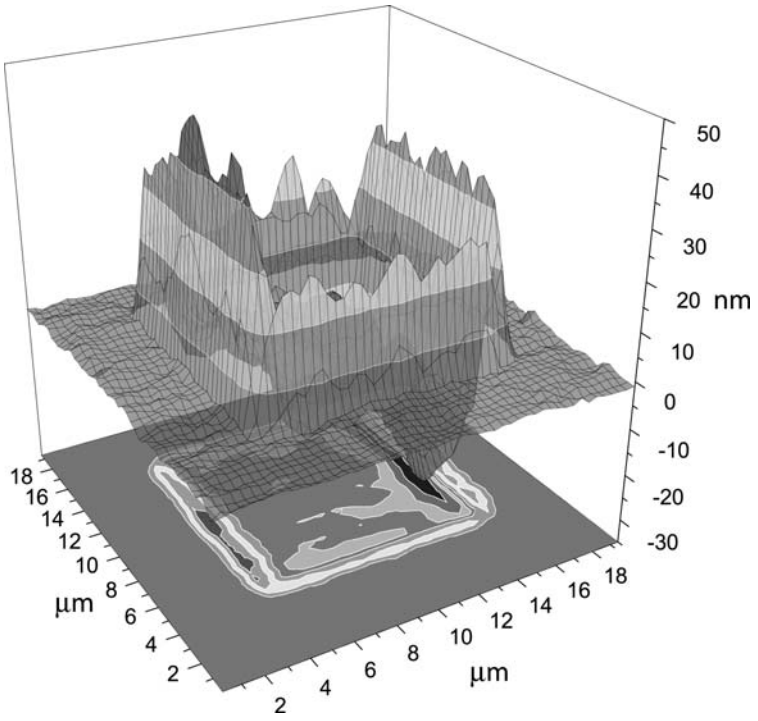

Figure 5-7. Rastering wear test data plot showing a trenched area on the right of the test area and a pile-up area on the left.

Triboindenter Reciprocating Wear Test

The reciprocating wear test mode, or scratch mode, is a normal load control and lateral displacement control test. The Triboindenter collects normal displacement, and lateral force data during the experiment. The normal displacement data is subject to errors from sample tilt and thermal drift. To compensate for sample tilt, a low load pre-scan of the wear track is collected and this displacement data is subtracted from the data collected during the test. In the indentation mode, there is a provision to monitor thermal drift for a selected amount of time, and then subtract the recorded drift from the displacement data. A typical indentation test is run over a short period of time. The drift monitor can be set to record drift over a similar amount of time and wait until the drift reaches some minimum threshold, or until the drift is sufficiently linear. In the reciprocating wear mode, this is not practical due to the length of time that the test is run. Therefore, the displacement of the test will be verified by cross sections taken from wear tracks and measured in SEM or TEM and adjusted accordingly.

Lateral force data is also subject to errors due to sample tilt. To remove tilt error from the lateral force data, the initial low load pre-scan friction data is subtracted from the data. During the reciprocating tests, material piles up at the ends of the tracks, and near the endpoints of reciprocation, displacement is increased due to smaller initial contact areas. The frictional data is filtered to examine sliding conditions excluding these transient areas (Figure 5-8). The friction force is the average per sliding pass and can then be examined versus sliding cycle.

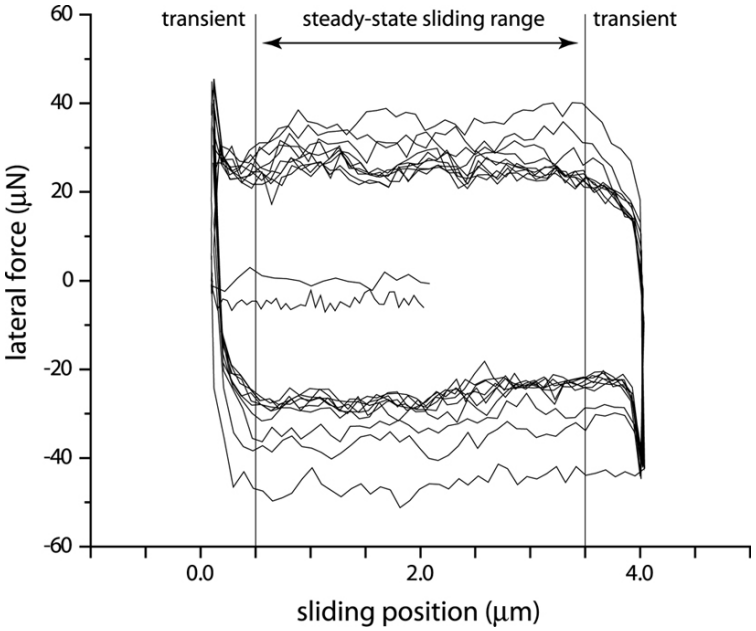

Figure 5-8. Data from a 10-cycle reciprocating wear test showing the transient areas near the ends of the reciprocation and the area over which the friction force data is analyzed.

CSM Microtribometer

Frictional force data is collected and analyzed in a similar manner to the reciprocating test in the Hysitron Triboindenter. An extensive development of data collection and analysis was presented by Dickrell [22].

CHAPTER 6
CHARACTERIZATION

Tip Characterization

The indenter tip used for the majority of testing in this study is a single crystal diamond. Diamond is a convenient material due to its high hardness and resistance to wear. In addition, it is well known that gold does not wet carbon which will be beneficial to avoid material transfer from the film to the indenter tip. Due to high costs and limited available geometries, indenter tips of various materials may be sought out. The following methods can be applied to most tip materials. Tip geometry is critical in analysis of indentation and wear testing. Properties such as elastic modulus, hardness, shear stress, and friction coefficient are all calculated from contact areas based on tip geometry. Inaccuracies in tip geometry will cause significant errors in contact area calculations which will propagate to the above mentioned properties. Methods for determining tip geometry include: the indentation method, the scanning method, and electron microscopy imaging.

Indentation Method

This method, developed by Oliver and Pharr [25], involves creating a series of indents of various depths on a standard sample of known elastic modulus, typically fused quartz. By generating a plot of area versus contact depth as described in Chapter 5, a function in the form of Equation 5-14 can be generated to describe the contact area as a function of contact depth. This method has proven reliable for samples that exhibit high hardness with little plastic deformation; however, it greatly underestimates the contact

area in samples that exhibit pile-up which leads to errors in hardness and modulus [32]. This method is also lacking in three-dimensional information which is necessary in calculating properties derived from lateral translation of the tip.

Scanning Method

The scanning method is an adaptation of scanning tunneling microscopy (STM) and atomic force microscopy (AFM) techniques that involve scanning the tip over a sample with well characterized features or features of much smaller radii than the tip [34-36]. By scanning a feature with a radius much smaller than the tip, the image produced is representative of the tip (Figure 6-1).

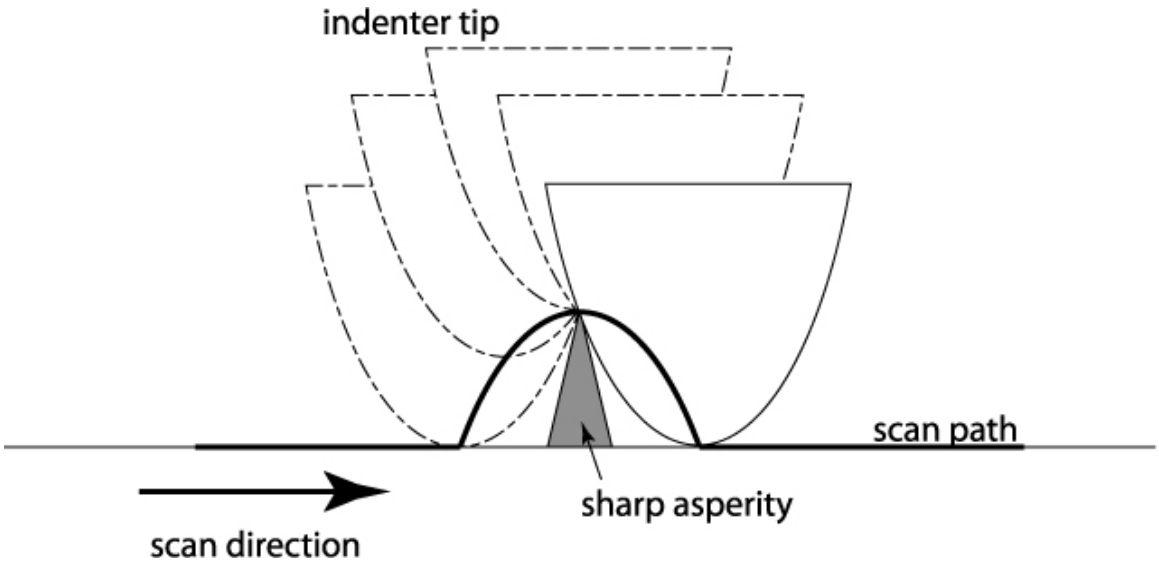

Figure 6-1. A schematic representation of a large radius tip scanning a small radius asperity.

An FEI DB235 dual beam focused ion beam (FIB) microscope (described later in greater detail) was used to produce a sharp pyramidal asperity with a radius of less than 100 nm. A silicon wafer was mounted in the FIB and the normal to the sample was tilted to 20º with respect to the ion beam. A trench was milled, and the sample was rotated 120º about the ion beam. Another trench was milled and the sample was again rotated 120º. This

procedure was repeated at progressively lower beam currents to sharpen the asperity radius (Figure 6-2).

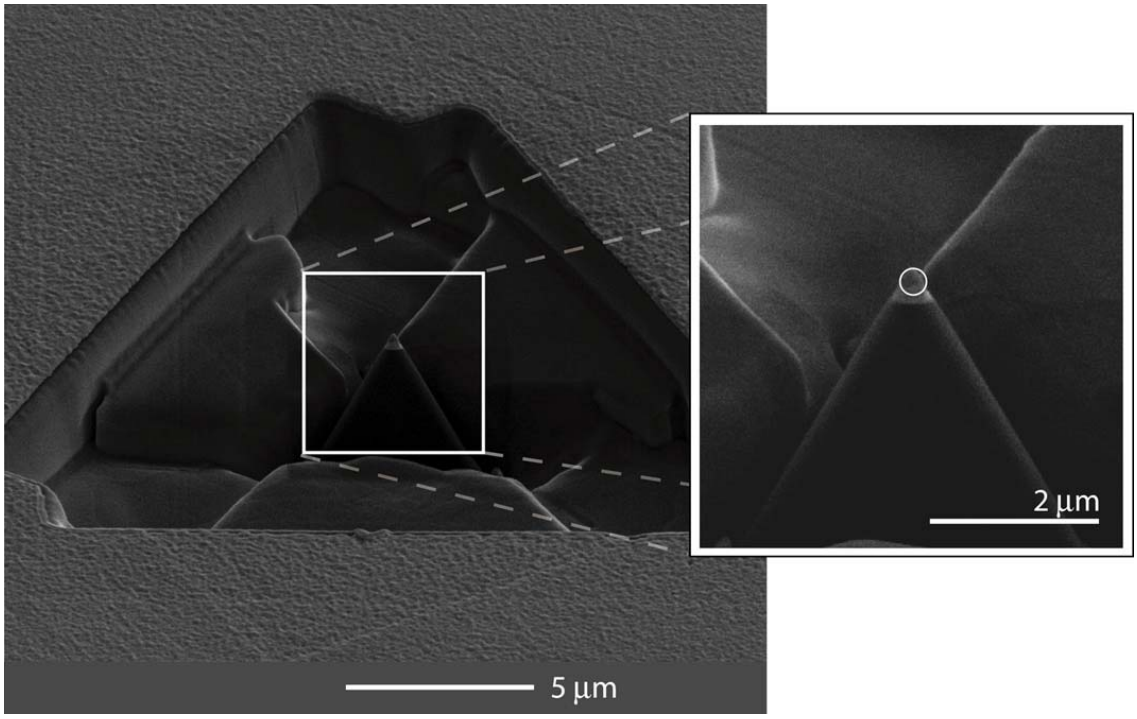

Figure 6-2. Sharp asperity milled on silicon to scan indenter tip.

The sharp asperity sample is mounted on the Triboindenter and the desired tip is installed on the transducer. The Triboindenter is set to imaging control which places the transducer into load feedback mode. An imaging set point load of 1 µN is selected. Using the piezo tube scanner, the tip rasters over the sharp asperity feature maintaining the 1 µN load and recording x, y, and z positional data. The x, y, and z data is entered in scanning imaging software to produce the image seen in Figure 6-3.

This procedure is attractive because it can be run just prior to and upon completion of testing to verify tip geometry. Because it is an in-situ method, removal of the tip for characterization is not required. This method suffers from longevity of the sharp asperity

feature. The feature should be made from the hardest, toughest material available. A diamond sample of the sharp asperity would be optimum.

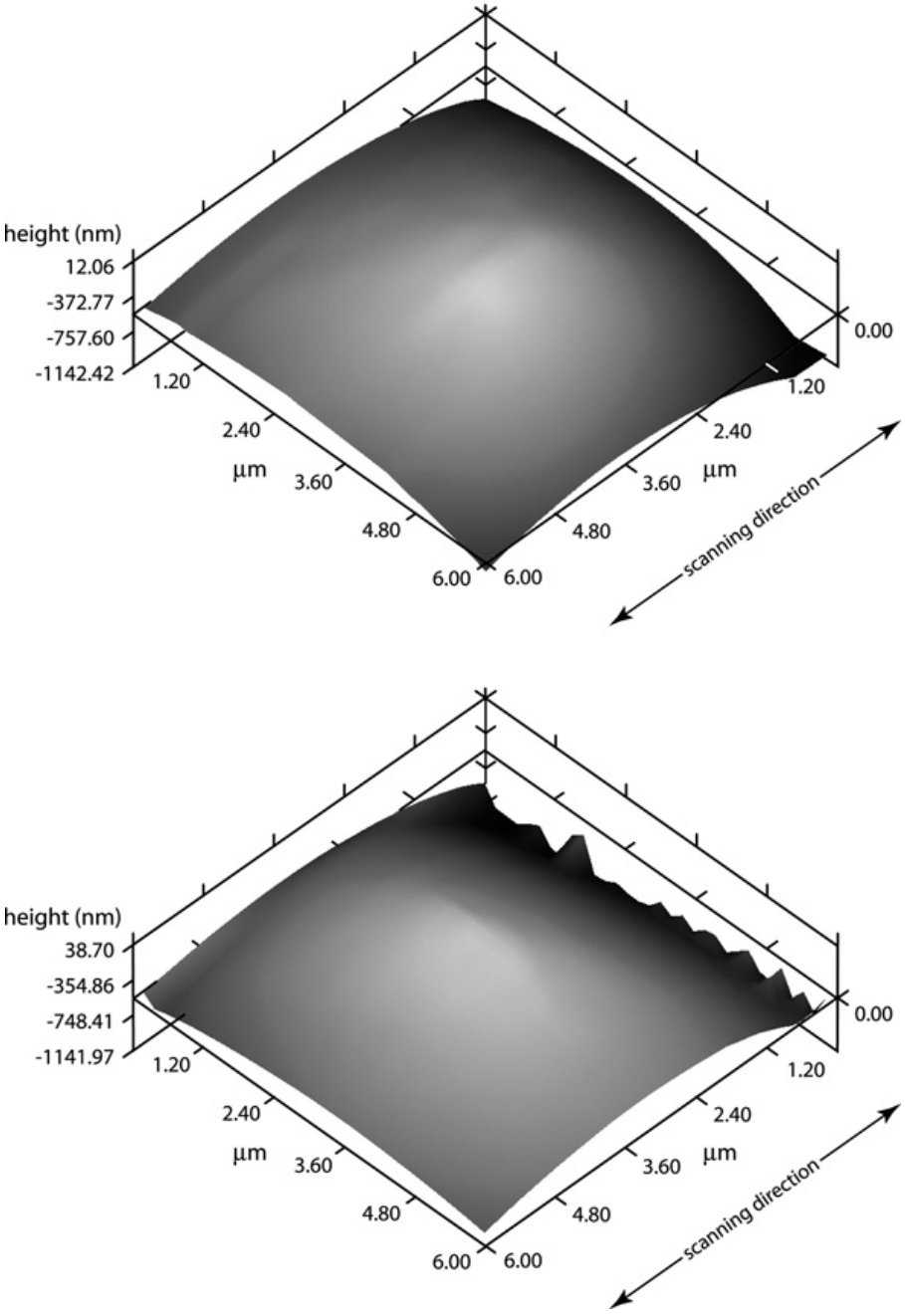

Figure 6-3. Scanning image produced with a sharp asperity by rastering first in the x direction, and then in the y direction.

Transmission Electron Microscopy Method

A direct measure of the tip geometry is the best method for characterization. Imaging the tip in a transmission electron microscope provides a high resolution profile of the geometry. A fixture to mount the indenter tip in a TEM sample holder was fabricated and is seen in Figure 6-4. The indenter tip is fixed in a polymeric mounting device with a blind threaded hole as received from the equipment manufacturer. The polymeric fixture is glued into the TEM mounting fixture, using a conductive adhesive. The mounting fixture is attached to the TEM sample holder with countersunk set screws.

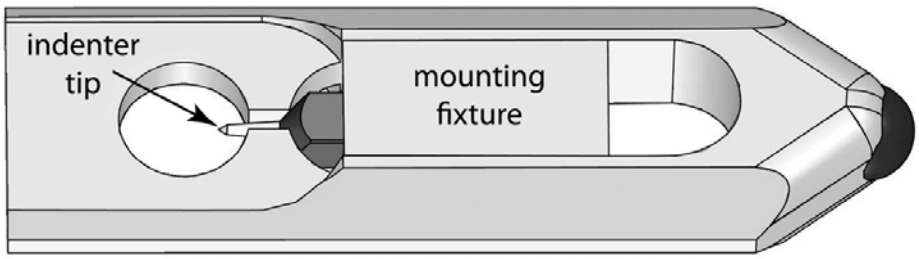

Figure 6-4. Schematic drawing of TEM 200 CX sample holder with tip holder fixture and indenter tip mounted.

The normal loading axis of the indenter tip is oriented such that it is parallel with the sample holder tilt axis. The sample holder is inserted into a JEOL 200CX TEM and the tip is imaged at 50 kX and 200 kV. The sample is adjusted so the normal loading axis and sample tilt axis are at the eucentric height. The indenter tip can be rotated from 60º counter-clockwise (CCW) to 60º clockwise (CW) to produce profile images through 120º of rotation. A series of images are collected at 40º CCW, 0º, and 40º CW, the images are digitized and points are plotted along the profile. The data is fit to a curve to approximate an axisymmetric geometry to describe the tip shape, see Figure 6-5.

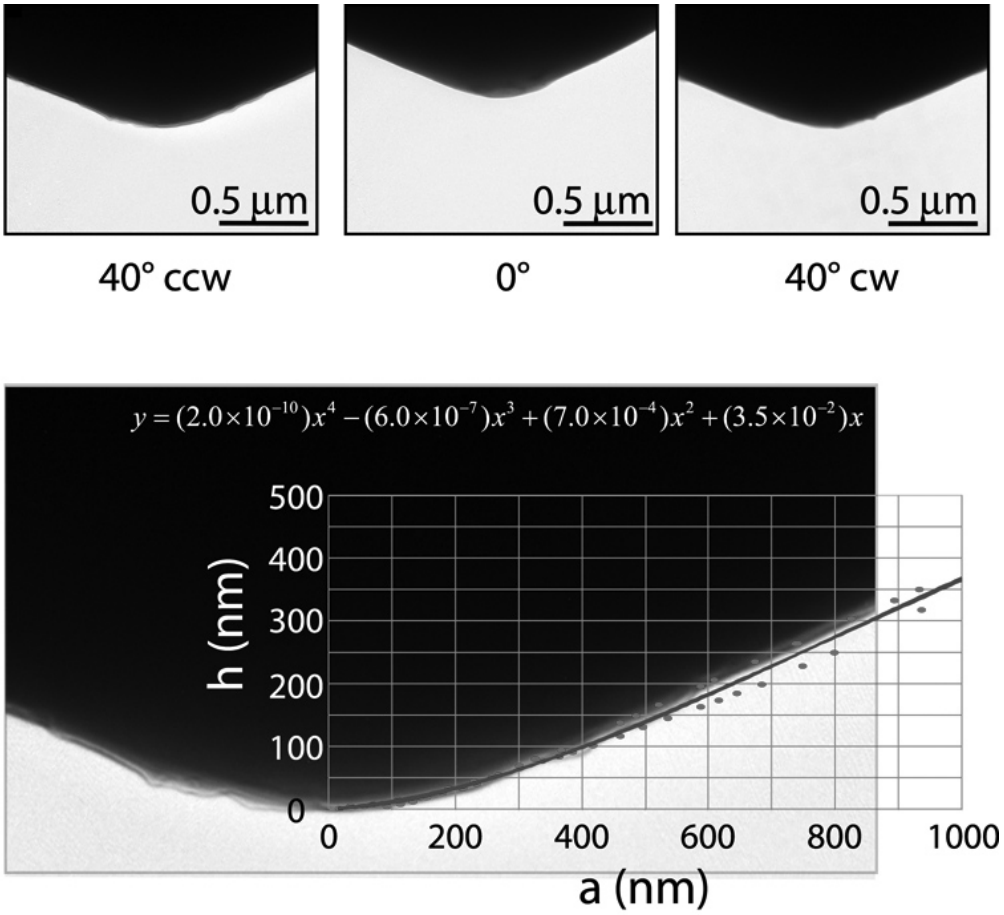

Figure 6-5. The upper images are taken at 40º CCW, 0º, and 40º CW respectively. The lower image shows data points plotted along the profile and subsequently curve fit to a 4th order polynomial.

This method can also provide crystallographic orientation information in addition to tip geometry. By entering diffraction mode with the beam focused on the indenter tip, a Kikuchi map image is produced. The crystallographic planes that are orthogonal to the tilt axis remain parallel to the electron beam and therefore diffract through the range of tilt. Since the normal loading axis of the indenter tip is coincident with the tilt axis the planes that remain diffracting through the tilt, or the planes indexed to correspond to the Kikuchi band upon which the tilt occurs, correspond to the planes normal to the loading axis. One degree of freedom remains to describe the crystallographic orientation of the indenter tip. By noting the tilt angle at zone axes along the Kikuchi band, the

crystallographic orientation of the tip is characterized, see Figure 6-6. Figure 6-7 shows a schematic representation of the crystallographic orientations of the indenter tip and the direction of reciprocation in the wear tests.

Once the crystallographic orientation of the indenter tip is characterized, elastic properties of the tip can be calculated from the stiffness matrix. Single crystals are often elastically anisotropic and therefore the Young's modulus and Poisson ratio are orientation dependent [37].

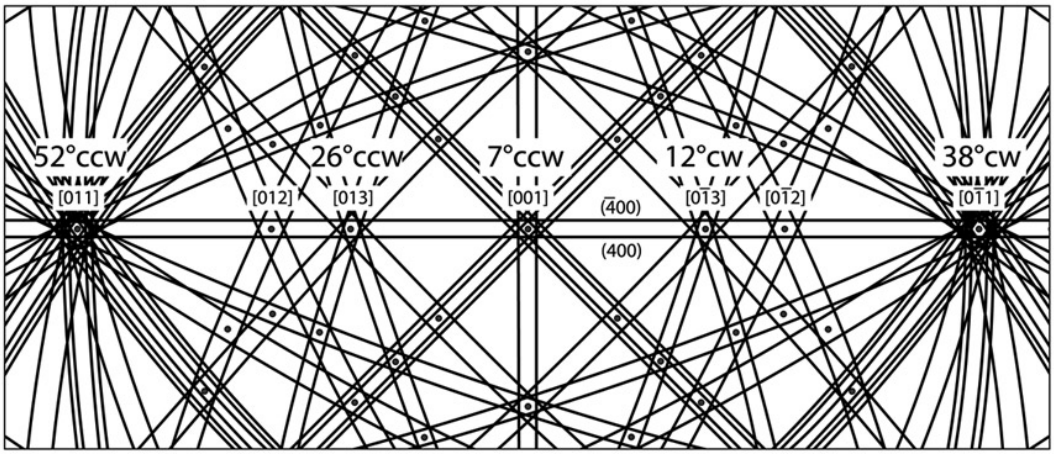

Figure 6-6. Schematic representation of the Kikuchi map observed in diffraction mode indexed such that the (100) plane is orthogonal to the tip loading axis. The major zone axes are labeled with the sample holder tilt angle readings.

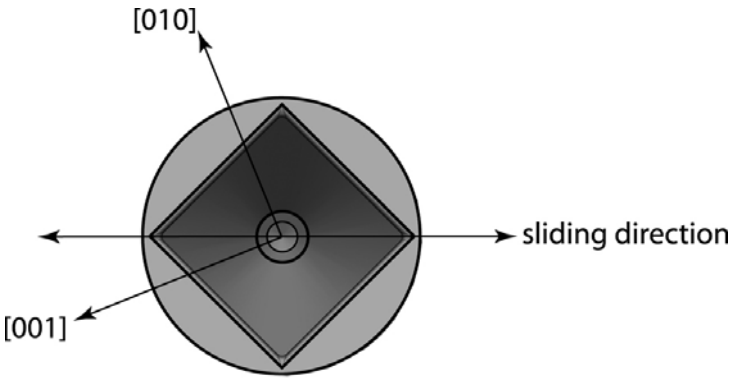

Figure 6-7. Schematic representation of a top down view of the single crystal diamond indenter tip with crystallographic orientations and sliding direction indicated. Note the loading axis of the indenter corresponds to the [100] direction as indexed in the image.

The orientation dependent Young's modulus of a cubic single crystal is given by:

$$\frac{1}{E_{uvw}} = S_{11} - 2[(S_{11} - S_{12}) - \frac{1}{2}S_{44}](l^2m^2 + m^2n^2 + l^2n^2) \quad (6\text{-}1)$$

where E_{uvw} is the Young's modulus for the direction of interest; S_{11}, S_{12}, and S_{44} are the coefficients of the compliance matrix; and l, m, and n, are the direction cosines of the [uvw] with respect to the unit cell axes [38] . Equation 6-1 contains the stiffness matrix for diamond [39]

$$C_{ij} = \begin{pmatrix} 1079 & 124 & 124 & 0 & 0 & 0 \\ 124 & 1079 & 124 & 0 & 0 & 0 \\ 124 & 124 & 1079 & 0 & 0 & 0 \\ 0 & 0 & 0 & 578 & 0 & 0 \\ 0 & 0 & 0 & 0 & 578 & 0 \\ 0 & 0 & 0 & 0 & 0 & 578 \end{pmatrix} GPa$$

which can be converted to the compliance matix by:

$$S_{ij} = C_{ij}^{-1} = \begin{pmatrix} 0.949 & -0.0979 & -0.0979 & 0 & 0 & 0 \\ -0.0979 & 0.949 & -0.0979 & 0 & 0 & 0 \\ -0.0979 & -0.0979 & 0.949 & 0 & 0 & 0 \\ 0 & 0 & 0 & 1.73 & 0 & 0 \\ 0 & 0 & 0 & 0 & 1.73 & 0 \\ 0 & 0 & 0 & 0 & 0 & 1.73 \end{pmatrix} TPa^{-1}$$

From figure 6-7, the loading orientation of the indenter tip is characterized and therefore the Young's modulus in the loading direction is calculated at 1053 GPa.

X-ray Diffraction

X-ray diffraction is used to characterize the grain size and the texture of the gold films. A Philips APD 3720 diffractometer with a Cu Kα (λ=1.54178 Å) x-ray source is used to scan the samples. Figure 6-8 shows a schematic drawing of the diffractometer.

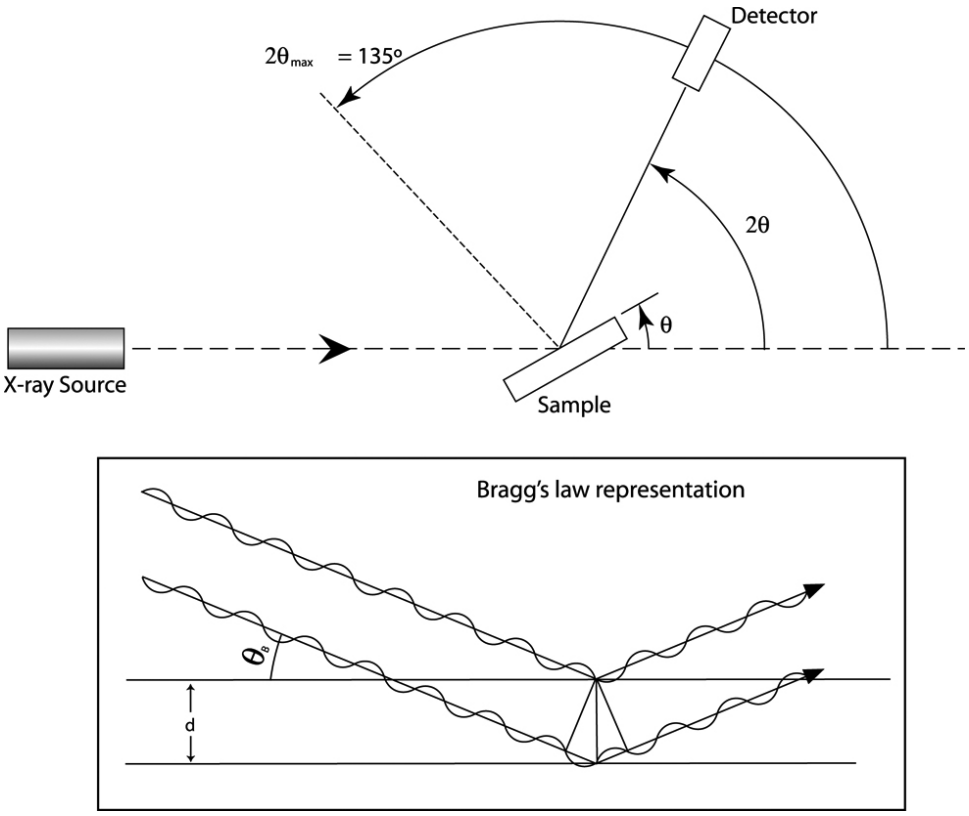

Figure 6-8. Schematic drawing of an x-ray diffractometer with a representation of Bragg's law.

The x-ray source is in a fixed position, and the sample is rotated through θ. The x-ray detector is rotated 2º for every 1º of the sample and is therefore rotated 2θ with respect to the x-ray source. A plot is generated containing the number of counts recorded by the detector versus 2θ. From Bragg's law:

$$n\lambda = 2d\sin\theta \tag{6-2}$$

where n is an integer (1, 2, 3….), λ is the wavelength of the radiation, d is the spacing of the diffracting planes, and θ is the Bragg angle, the spacing of the diffracting planes can be determined. Samples are scanned from 30º to 130º 2θ and data is collected to determine crystallographic texture and to choose a family of planes to analyze for grain size approximation.

Crystallographic Texture

Often in processing a certain crystallographic orientation develops due to conditions. These conditions may be due to mechanical processing, thermal gradients upon solidification, or preferred growth orientation. For thin films, the latter is often the case. Since most single crystals exhibit anisotropic mechanical properties, it tends to reason that polycrystalline samples with a preferred orientation will also exhibit similar anisotropy.

Analysis of crystallographic texture by x-ray diffraction can range from exceptionally simplistic when only one out-of-plane orientation exists, to rather complex as the orientation becomes more random. For the simple case when only one out-of-plane orientation exists, Bragg's law will only be satisfied for planes parallel to the surface and they will be the only intensities that show up in the 2θ scan. To analyze the texture of a more random sample, one must consider the integrated intensities of the various peaks that show up in the scan. This is not a simple direct comparison because the intensity is a function of the diffracting planes and the Bragg angle through the structure factor, multiplicity factor, and the Lorentz-polarization factor [40]. A simple method to approximate the sample texture is obtained in the JCPDS files. Each file contains space group, lattice parameter, planar spacings, and relative peak intensities for perfect powder samples. A perfect powder sample is equiaxed, or randomly oriented, therefore by comparing relative peak intensities collected from a sample of interest with those of the JCPDS file, one can draw conclusions about the texture.

Samples were scanned from 30º to 135º 2θ with a step size of 0.02º. Figure 6-9 shows 2θ scans for the six different gold coatings used in the test matrix. All six show a strong (111) texture with no other significant orientations.

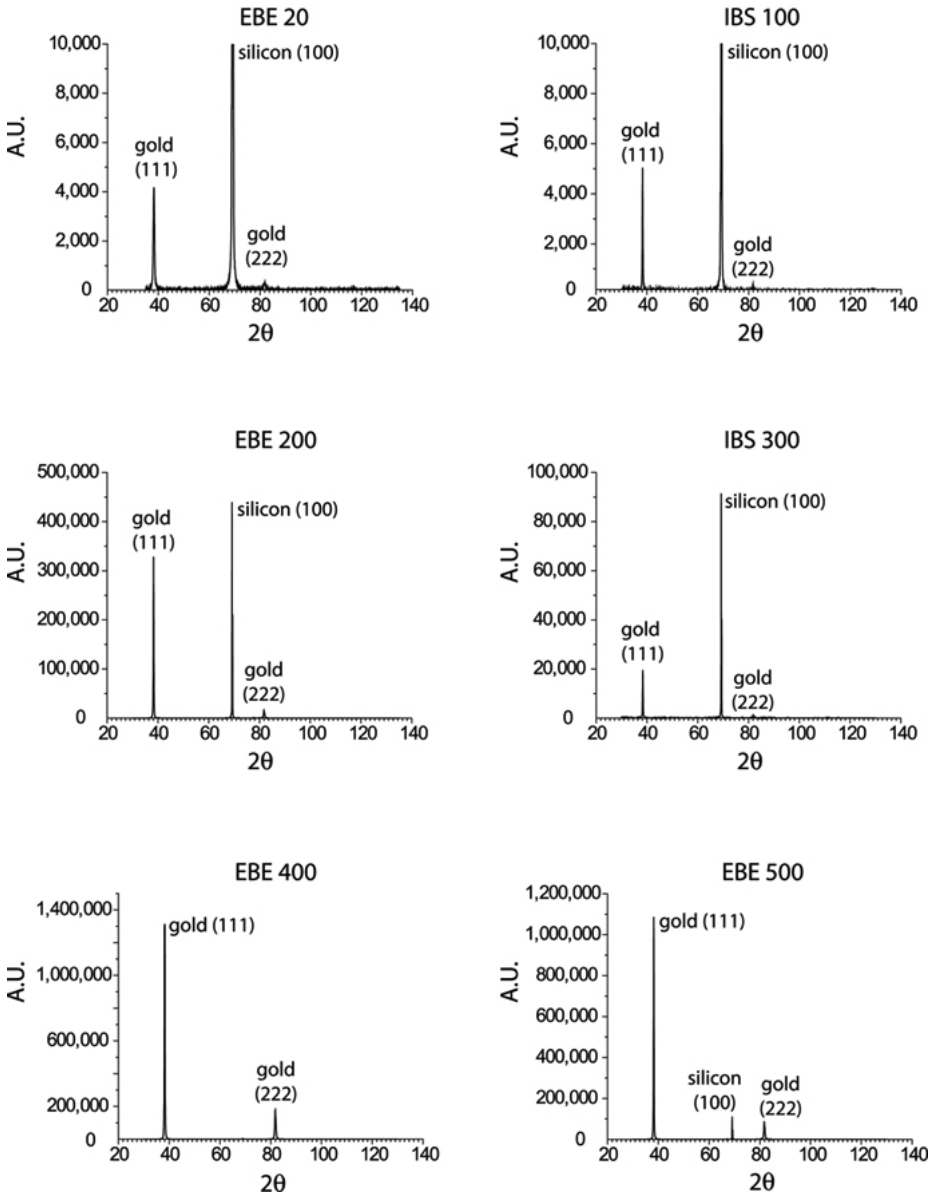

Figure 6-9. Scans of the six different gold films shown with indexed peaks.

Equiaxed polycrystalline gold has a Young's modulus of 78.5 GPa [41], whereas single crystal gold is elastically anisotropic with the <111> orientation being the stiffest. It is reasonable to assume that the textured film will exhibit the elastic properties of the single crystal rather than those of an equiaxed polycrystalline sample, therefore the Young's modulus is calculated to be $E_{Au<111>} = 117$ GPa using Equation 6-1 and the stiffness matrix for gold:

$$C_{ij} = \begin{pmatrix} 190 & 42.3 & 42.3 & 0 & 0 & 0 \\ 42.3 & 190 & 42.3 & 0 & 0 & 0 \\ 42.3 & 42.3 & 190 & 0 & 0 & 0 \\ 0 & 0 & 0 & 161 & 0 & 0 \\ 0 & 0 & 0 & 0 & 161 & 0 \\ 0 & 0 & 0 & 0 & 0 & 161 \end{pmatrix} GPa$$

Grain Size

The grain size of a metal affects the yield strength by the Hall-Petch relationship [37]:

$$\sigma_y = \sigma_0 + kD^{-\frac{1}{2}} \tag{6-3}$$

where σ_y is the yield strength, D is the grain size, and σ_0 and k are material parameters. To elucidate the plastic response of a material, the grain size should be well characterized.

Scherrer first showed that decreasing particle size resulted in slight deviations from Bragg's law in diffraction due to incomplete destructive interference, which results in peak broadening [42]. Peak broadening can be due to particle size, or grain size, and residual strain, and is usually a combination of the two. Warren and Averbach devised a method to represent diffraction peaks as Fourier series. They showed that by comparing families of peaks, (111) and (222) for example, coefficients due to strain and grain size could be separated because the strain coefficient is dependent upon the index of the planes, whereas the grain size coefficient is not. These calculations have been incorporated into software packages for stain and grain size analysis.

To collect data for the grain size and strain measurements, the diffractometer was set to scan ± 2.5º at 38.2º 2θ and ± 2.5º at 81.7º 2θ which correspond to the (111) and

(222) respectively. To increase resolution, the step size was set at 0.05º. The data was entered in the Philips Line Profile software along with scans from standard samples with similar d-spacing, and the Warren-Averbach grain size and strain analysis was performed. Figure 6-10 shows results of the film grain size and strain with respect to the film thickness. The grain size is increasing with film thickness up to 45 nm grains in films over 300 nm thick. All films show 0.1% compressive strain except the sample designated EBE20 with a film thickness of 27 nm and 0.22% compressive strain.

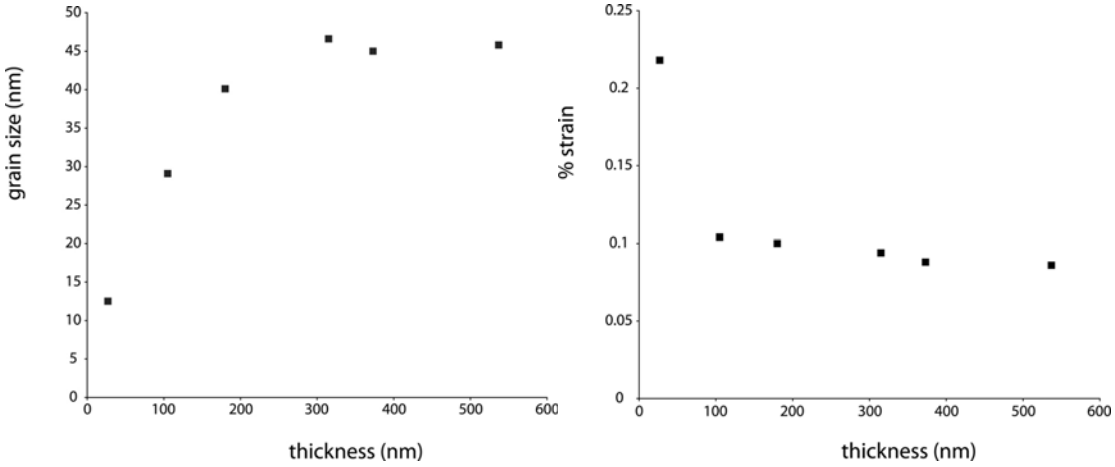

Figure 6-10. Plots of grain size and strain versus gold film thickness.

Scanning Electron Microscopy

Samples were imaged to examine wear tracks and determine film failure in an FEI DB235 field emission gun (FEG) microscope by first locating the test area from the grid lines that were milled prior to testing. Once the area was located, magnification was increased and the sample was oriented so that the direction of wear was along the horizontal, or x-axis. The sample was then tilted about that axis 52º to provide better perspective. Test areas were imaged at 20-25 kX magnification using a secondary electron detector, 30 μm aperture, 5 keV accelerating voltage and number 2 spot size. Some samples displayed beam sensitivity, so image quality was sacrificed to protect the

sample from repeated rastering with the beam. Each wear test from the matrix was imaged and examined for coating damage and breakdown.

Focused Ion Beam Milling

A Dual Beam FEI focused ion beam (FIB) DB235 microscope was used for grid line etching as mentioned earlier. This microscope is equipped with a field emission gun (FEG) high resolution SEM column situated vertical. Mounted 52º with respect to the electron column is a liquid metal ion source (LMIS) FIB column using gallium for the ion source. The microscope has a gas injection system (GIS) which allows platinum deposition by heating the organic-metallic compound methylcyclopentadienyl (trimethyl) platinum to 313 K and then opening the injection system in the microscope chamber. The low pressure of the microscope chamber (~ 10^{-5} Torr) causes the compound to out gas and adsorb on the sample surface. Scanning with the ion beam reduces the compound leaving a platinum layer on the surface. The area of platinum deposition can be controlled by the rastering area. The microscope is also equipped with an Omniprobe Autoprobe 200 which provides in-situ mechanical micro-manipulation.

Transmission Electron Microscopy Sample Thinning

Samples for TEM examination must be at least less than 200 nm thick for most materials. For HRTEM, samples must be typically less than 100 nm thick. Producing cross sectional TEM samples of a uniform thin film using conventional techniques is challenging. Attempting to produce site specific cross sectional TEM samples with conventional techniques of micron sized features would require a degree of luck that would be better suited for playing the Florida Lottery. Fortunately, the FIB microscope has the capability of locating micron sized sites and milling thin cross sections from them.

Once the wear tests were finished, samples were selected for TEM examination. On those samples, the wear tests were located using the grids lines. The wear test was oriented such that the cross section would be orthogonal to the sample surface, and either orthogonal or parallel to the wear direction. For cross sections that were parallel to the wear direction, indicator marks were etched for final thinning process (Figure 6-11). Fiducial 'x' marks were milled for automated milling.

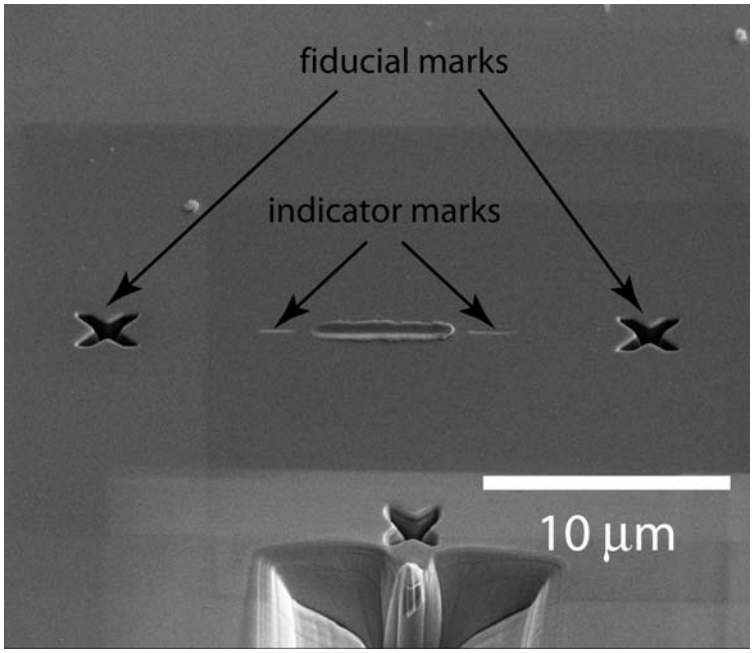

Figure 6-11. SEM micrograph of wear track in center of image to be prepared with cross sectional TEM parallel to the wear direction. Both indicator and fiducial marks milled by ion beam are indicated with arrows.

Platinum was deposited 2 um x 15 um x 1 um high to protect the area of interest while milling. Trenches approximately 15 µm x 5 µm were milled at 5 nA beam current to 6 µm deep at the base and sloped out to about 1 µm deep on both sides of the desired cross section area. Progressively lower beam currents were then used to remove more material and reduce ion damage. Once the sample is thinned to approximately 1 µm thick, the stage is tilted and the sample is undercut with only small tabs of material keeping the

cross section connected to the bulk. The sample is then tilted back and the final automated polishing steps are performed at 300 pA current to thin the sample to approximately 300 nm. Once the automated script is complete, the thinning is controlled manually at 30 pA to thin the sample to less than 100 nm thick. The cross section is then cut free with the 30 pA beam current, and the sample is removed from the FIB. Figure 6-12 illustrates the steps.

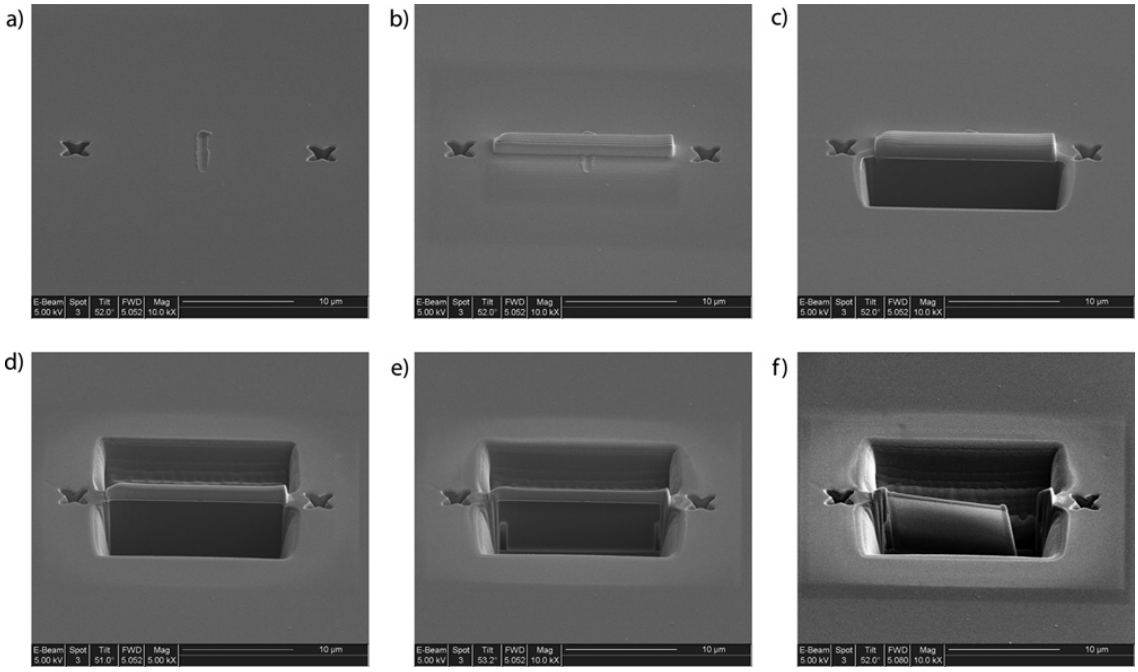

Figure 6-12. FIB cross section sample preparation. A) area of interest is located and fiducial marks are milled. B) platinum is deposited. C) front trench is milled. D) back trench is milled. E) cross section is undercut. F) cross section is cut free.

The sample is then transferred to an optical microscope equipped with hydraulic micromanipulators. Glass rods are heated and pulled in tension to form sharp radius tips of approximately 1 μm radius. The rods are attached to the hydraulic micromanipulators for precise movement. The cross section area is imaged with the optical microscope and the glass rod is brought into contact with the cross section. The cross section is attached to the rod by static forces and it is lifted out of the sample trench. The sample is removed

and replaced with a carbon film coated copper TEM grid. The static attraction between the carbon film and the cross section is greater than the attraction between the cross section and the glass rod so the cross section can be deposited on the carbon film. The process is illustrated in Figure 6-13. The cross section is now ready for TEM examination.

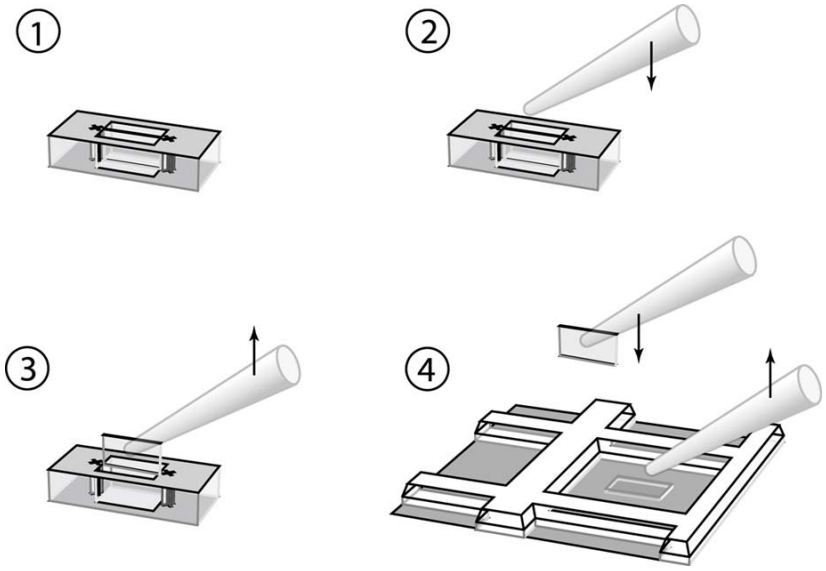

Figure 6-13. Cross section is removed from the sample trench with a glass rod attached to a hydraulic micromanipulator and then deposited on a carbon film coated copper TEM grid.

Slice and View Serial Sectioning

The FEI DB235 FIB microscope is capable of milling with the ion beam, followed by imaging with the electron beam. Using these techniques, a series of images can be produced similar to tomography. From these images, movies can be assembled to produce a view of 'moving' through the bulk of a sample and with the aid of computer software, three dimensional reconstructions of the sectioned sample can be generated. There are alternate methods for producing a series of slice and view images. The first

described will be referred to as the ‘fixed sample method.’ The second technique will be referred to as the ‘rotated sample method.’

Fixed sample method

In this method, the sample is not rotated once the sectioning process has begun. The sample is oriented orthogonal to the ion beam or 52º from the electron beam. A sloped trench is milled to clear material so the sectioning area can be imaged with the electron beam (Figure 6-14). Some bulk material from around the area of interest can be removed prior to sectioning to aid in imaging.

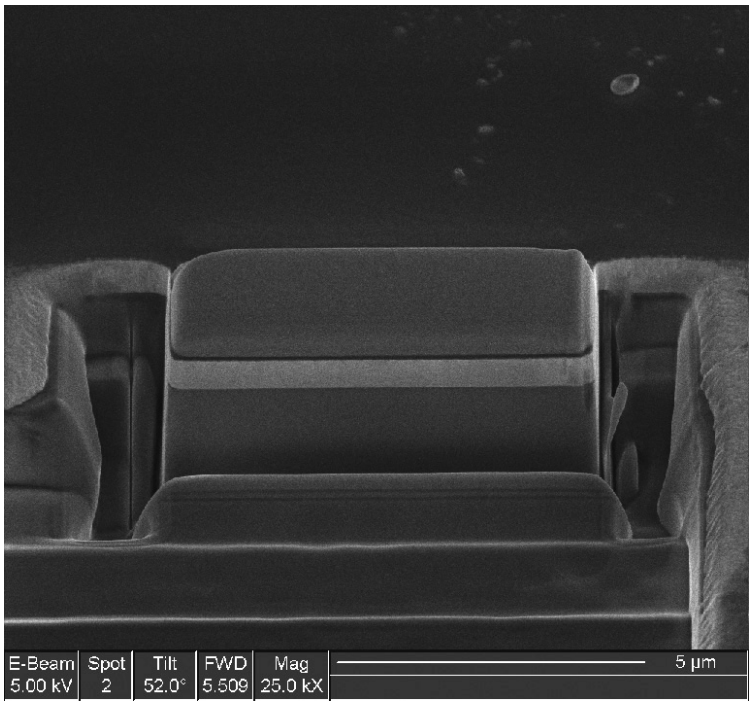

Figure 6-14. SEM image of trenched area in preparation of fixed sample method slice and view serial sectioning procedure.

A series of ion beam slices, each followed by an electron beam image, is recorded. The fixed sample method can be automated using scripting software which requires initial set up but then runs to completion without user interaction.

The ion beam is mounted 52º with respect to the electron beam so the image height will need to be corrected if the sample is not rotated when imaging. The correction is as follows:

$$y_{actual} = \frac{y_{image}}{\sin 52^{o}} = 1.27 y_{image} \tag{6-4}$$

where y_{actual} is the actual dimension in the y-axis or height of the image area, y_{image} is the dimension of the projected height in the image. The image can be corrected in image processing software by changing the height on the image by 1.27 times while keeping the width the original value. In addition to producing a series of images, this technique can be used to produce a single cross section image. This is much less time consuming, and greater emphasis can be place on image quality.

Rotated sample method

An alternative to correcting the image is tilting the sample so that the electron beam is orthogonal to the imaging surface. This requires a free, unobstructed view of the surface. The following method, illustrated in Figure 6-15, was devised to section and image wear tracks.

- The wear test is located with the electron beam and tilted to 52º with respect to the e-beam.
- A platinum layer is deposited approximately 1 μm thick and twice as long as the wear scar.
- Trenches are milled on each side and in front of the wear scar to about 4 μm deep. The trench on one side is milled with the sloping cut, so an undercut can be performed.
- The sample is tilted to 0º with respect to the electron column, and an undercut is made the entire length of the wear scar up to the platinum protection layer.

- The Omniprobe in-situ micromanipulator is inserted in the front trench and the material containing the wear scar is lifted up to approximately 45º using the platinum as a plastic hinge.
- Now the sample is tilted 7º and the first slice is taken off with the ion beam.
- The sample is rotated 38º and an image is taken with the electron beam.
- Step 6 and 7 are repeated until the entire wear track has been sliced and imaged.

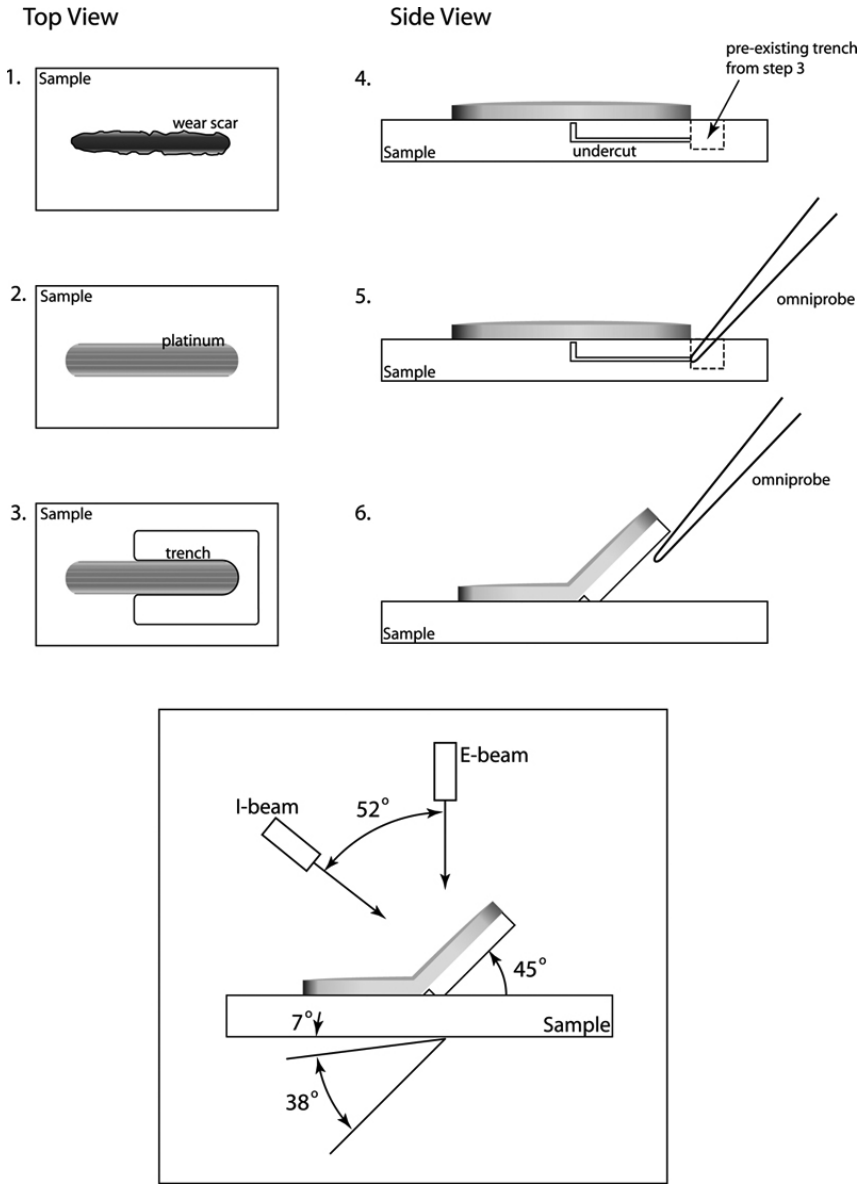

Figure 6-15. Schematic illustration of slice and view rotating sample method.

This process has advantages over the fixed sample process in that no correction is needed and the image retains the same resolution in the height and width. Since there is no bulk surrounding the area, imaging is less challenging because there is no signal loss due to imaging down into a trench. The exposed surface can also facilitate electron back scattered diffraction (EBSD) if the FIB is equipped with such analysis. The process has disadvantages due to complications with some geometries and the time required is considerably longer than the fixed sample method.

Once the images are collected, they can be loaded into Macromedia Flash or similar processing software. The images can be registered to each other and generate a movie of slices through the material. In addition to movie making software, three dimensional reconstructure software, such as TGS's Amira, can be used to produce three dimensional images and slices in different orientations from the slicing orientation. These techniques provide information about surface and subsurface damage, such as material volume exuded from the contact, plastic deformation zone characteristics, and sub-surface crack formation and delamination, that is unobtainable by top-down microscopy techniques.

Transmission Elelctron Microscopy Analysis

After cross sections are produce on the FIB, they are analyzed in a TEM. Film thickness is determined in a JEOL 200CX microscope at 200kV. Figure 6-16 shows cross sectional images of the six different film thicknesses with half cycle wear scars run at 500 μN normal load. Samples are named based on the deposition techniques, electron beam evaporation (EBE) and ion beam sputtered (IBS), and the targeted coating thickness. Acutal coating thickness is indicated on the images.

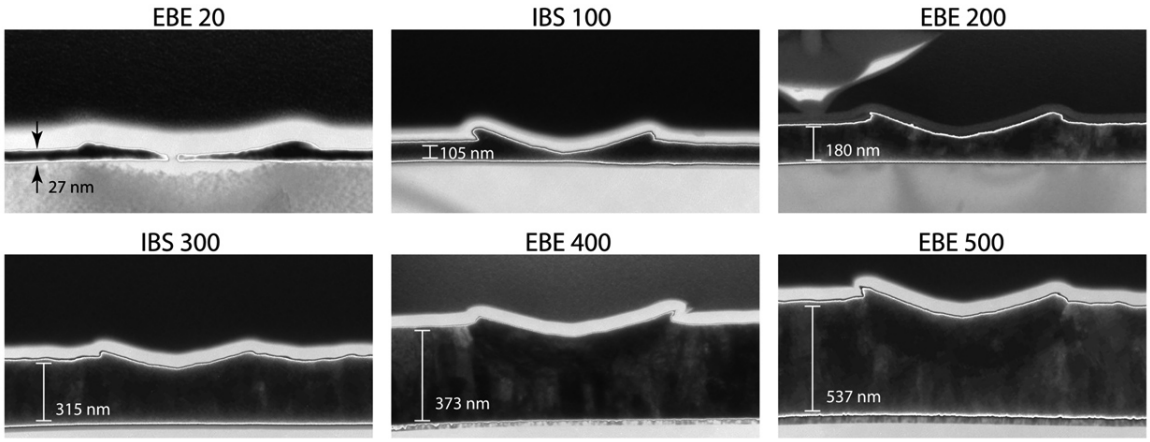

Figure 6-16. Cross sectional TEM images of gold films with wear tracks run for half cycles at 500 μN normal load. Film thicknesses are indicated on each image.

CHAPTER 7
RESULTS AND DISCUSSION

Static Indentation Testing

A series of fifty displacement control indents were performed from 10 nm to 100 nm on each sample varying the displacement incrementally from test to test. The tests were analyzed using all three methods mentioned in Chapter 5 namely: Oliver and Pharr (O-P), Stone, and Modified Winkler (MW). For each sample, hardness is plotted versus maximum tip displacement.

Oliver and Pharr Analysis Results

A plot of the hardness results based on the Oliver and Pharr model is shown in Figure 1.

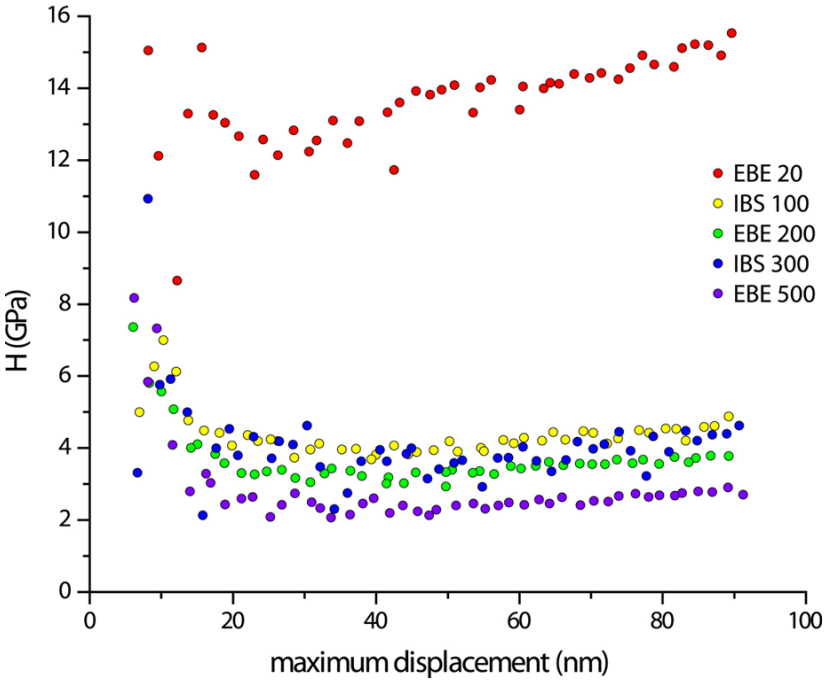

Figure 7.1. Plot of hardness determined by the Oliver and Pharr method versus maximum tip displacement for five samples of varying thickness.

As mentioned earlier, the Oliver and Pharr model overestimates hardness of materials that exhibit significant plastic flow. The Oliver and Pharr model assumes no pile-up. For indentations on materials that exhibit large plastic flow resulting in pile-up, the load is supported by a portion of the material that has been exuded. Oliver and Pharr's assumption of no pile-up results in an underestimated contact area. Since hardness is calculated from $H=P_{max}/A$, where H is the hardness, P_{max} is the maximum normal load, and A is the area, underestimating the area will result in overestimating the hardness. Indentation tests analyzed with the O-P model results show an increase in hardness for each sample below 15 nm in maximum displacement. This result could arise from an inaccurate tip area function for these low displacements or from excessive scatter observed at indentation tests performed below 15 nm maximum displacement. The exceptionally high hardness shown by the EBE 20 sample (27 nm thick) is more representative of hardness values for silicon (100) [43], which is due to the maximum displacement for the tests being well beyond 10% of the film thickness. Indentation well below 15 nm maximum displacement is required to examine the hardness of the gold film in sample EBE 20 without a substrate contribution. Although the manufacturer claims resolution of 0.2 nm displacement on the Hysitron Triboindenter, special tips are required to achieve repeatable results below approximately 10-15 nm.

Figure 7-1 shows the hardness for the remainder of the samples ranging from over 2 GPa for sample EBE 500 up to 5 GPa for sample IBS 100. Although the general 'rule of thumb' for indentation suggests indenting only 10% of the film thickness to avoid substrate contribution, the hardness values are not greatly affected by indentation depth for samples other than EBE 20 even on the IBS 100 sample with a film thickness of 105

nm. At a maximum displacement of 85% of the film thickness, the hardness has only increased by 25%.

For materials that exhibit significant plastic deformation, hardness is frequently approximated by the yield strength with the equation:

$$H = 3\sigma_y \tag{7-1}$$

where H is the hardness and σ_y is the yield strength [44]. Yield strength values for bulk gold range from 100 MPa to 200 MPa [41] giving a hardness range of 300 MPa to 600 MPa, well below the values calculated from Oliver and Pharr's model shown in Figure 7-1. However, the published yield strength values from handbooks are for coarse grained microstructures. It is well documented that yield strength increases with decreasing grain size by the Hall-Petch equation [37]:

$$\sigma_y = \sigma_0 + kD^{-\frac{1}{2}} \tag{7-2}$$

where σ_y is the yield strength, σ_0 and k are material dependent parameters, and D is the grain size. Combining Equation 7-1 and 7-2 gives:

$$H = 3(\sigma_0 + kD^{-\frac{1}{2}}) \tag{7-3}$$

Conrad and Jung found σ_0=216 MPa and k=0.06 MPa $m^{½}$ for gold [45]. Table 7-1 shows Hall-Petch calculated hardness using Conrad and Jung's constants and the grain size of the sample measured by XRD from Figure 6-10. The values for hardness range from 1.48 to 1.70 GPa. The reduction in grain size does not justify the high hardness values obtained from the Oliver and Pharr analysis method. Thus, inaccurate approximations of contact area due to material pile-up is the likely cause of over estimation of hardness.

Table 7-1. Hardness values calculated for samples from the Hall-Petch equation.

Sample	Hardness (GPa)
EBE 20	2.26
IBS 100	1.70
EBE 200	1.55
IBS 300	1.48
EBE 500	1.49

Stone Analysis Results

The same load displacement data that was used in the Oliver and Pharr method above is also analyzed using Stone's approach. If the assumptions of no indentation size effect and unloading as an isotropic elastic half-space are valid, the plots of compliance times the square root of load versus the square root of load should fall on one line as described in Chapter 5. Figure 7-2 and 7-3 show Stone plots for samples EBE 20 and IBS 100 respectively.

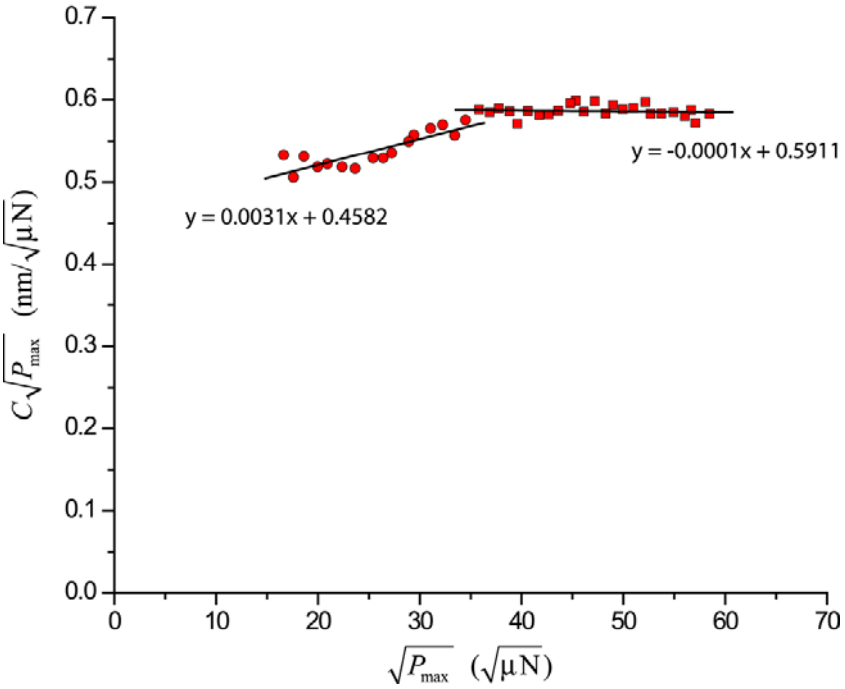

Figure 7-2. Stone plot including linear curve fits for sample EBE 20 with a gold film thickness of 27 nm.

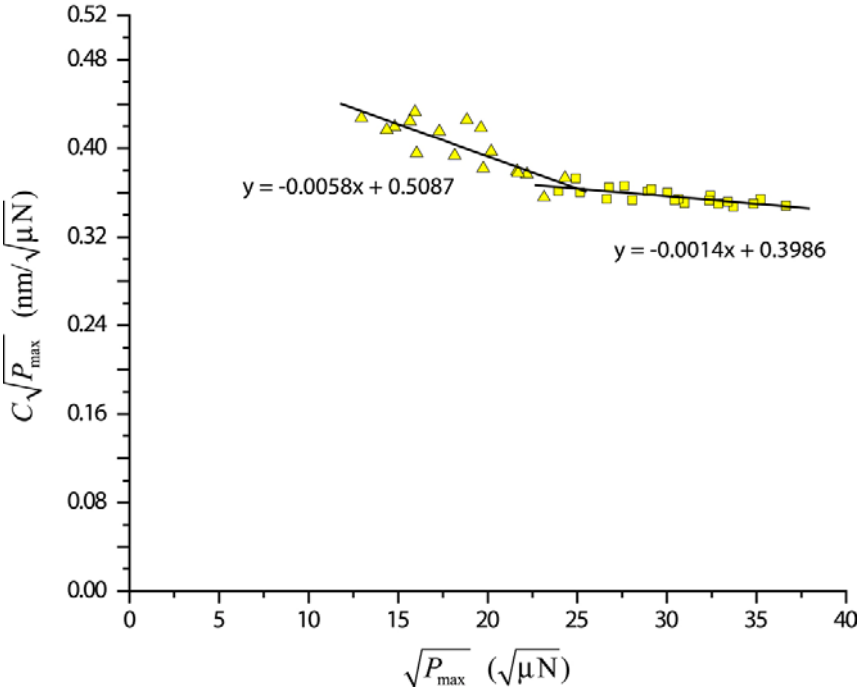

Figure 7-3. Stone plot including linear curve fits for sample IBS 100 with a gold film thickness of 105 nm.

Both plots do not fit well to a single line indicating a problem with the model. The assumption of an isotropic elastic half-space is questionable for multiple reasons. It is reasonable to expect some contribution from the substrate on both of these samples considering the ratio of indentation depth to film thickness is 74-330% on sample EBE 20 and 19-84% on sample IBS 100. The assumption of isotropy is problematic in that single crystals and textured surfaces are often elastically anisotropic. A measure of the degree of anisotropy is given by [46]:

$$\frac{C_{11}-C_{12}}{2C_{44}} \tag{7-4}$$

The compliance matrix for gold is given in Chapter 6, and the value for C_{11}, C_{12}, and C_{44} for silicon are 165 GPa, 64 GPa, and 79.2 GPa, respectively [41]. Calculating the degree of anisotropy for gold and silicon gives 0.46 and 0.64 where 1.0 is the result for an

isotropic material. In addition to these factors, there exists a pressure induced phase transformation in silicon which may occur in the upper bounds of the maximum displacement [47]. Figure 7.4 shows Stone plots for the remaining three samples, EBE 200, IBS 300, and EBE 500.

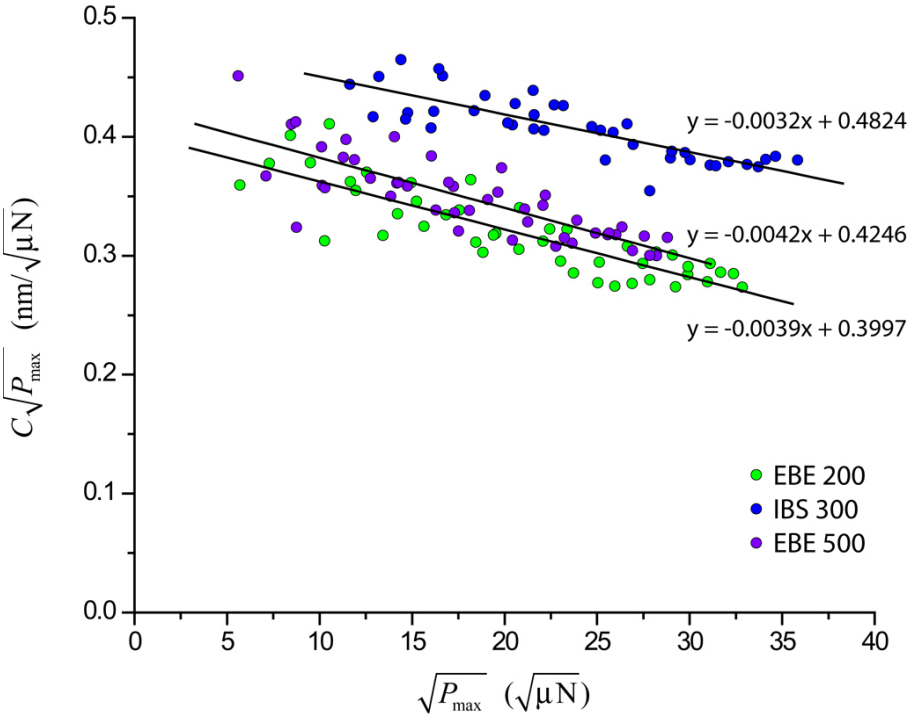

Figure 7-4. Stone plots including linear curve fits for samples EBE 200, IBS 300, and EBE 500 with a gold film thickness of 180 nm, 315 nm, and 537 nm, repectively.

The data from three samples from Figure 7.4 fits reasonably well to linear curves suggesting the assumption of no indentation size effect may be valid for these samples. The hardness for samples EBE 20 and IBS 100 will be calculated from the curve fits for the lower values of the square root of P_{max} because these values correspond to smaller indentation depths. Table 7-2 shows the sample versus the hardness calculated by the Stone method.

Table 7-2. Hardness values calculated for samples from the Stone method.

Sample	Hardness (GPa)
EBE 20	2.57
IBS 100	3.19
EBE 200	1.96
IBS 300	2.83
EBE 500	2.21

The values in Table 7-2 from the Stone analysis are lower than the values determined by Oliver and Pharr, but they are still higher than those predicted by the Hall-Petch equation.

Modified Winkler Approach

The Modified Winkler method was employed as described in Chapter 5 to account for the material pile-up exhibited in this system. This model assumes axisymmetric tip geometry based on the TEM characterization. Input parameters are film modulus and film thickness. The same load versus displacement data is used from the two previous analyses. Figure 7-5 shows a plot of the hardness versus the sample thickness for the Oliver and Pharr method, the Stone method, the Modified Winkler model, and the predicted values based on the Hall-Petch equation and sample grain size. The Modified Winkler predictions show excellent agreement with Hall-Petch for sample IBS 100, EBE 200, and IBS 300. Stone's method shows good agreement with Hall-Petch for sample EBE 20, however this is probably a coincidence. As mentioned previously, the assumptions for Stone's model are questionable for large displacement depth to film thickness ratios. The more likely agreement shows up on sample EBE 500 where Modified Winkler determines a value somewhat lower than Hall-Petch, and Stone calculates a higher value. The larger thickness of EBE 500 at 537 nm gives an

indentation depth to film ratio from 3.7% to 16.6% making the elastic half-space assumption much more reasonable.

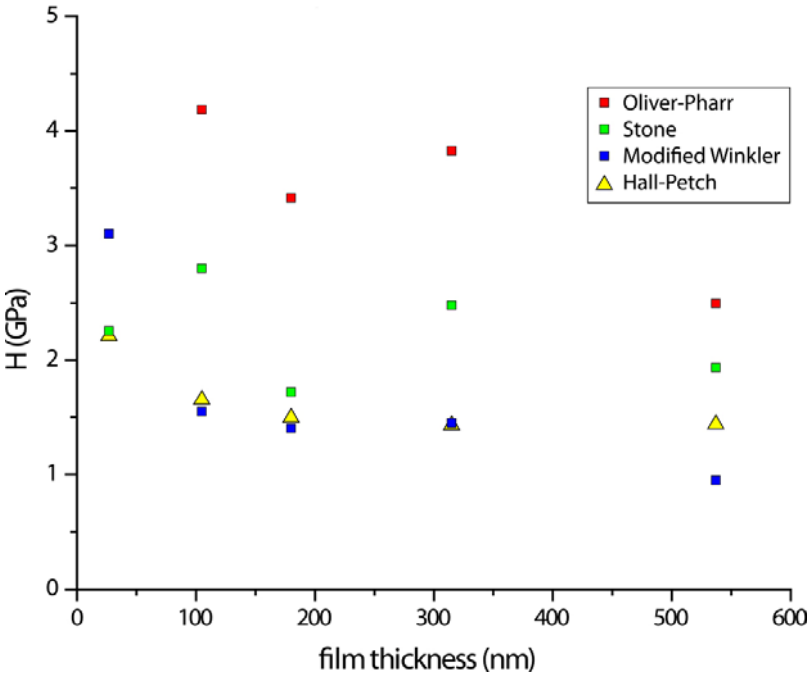

Figure 7-5. Hardness determined by four methods plotted versus sample thickness for five samples.

Excluding the low film thickness sample due to previously mentioned concerns, the Modified Winkler method shows the best agreement with the Hall-Petch equation for analyzing highly plastic thin film hardness on elastic substrates.

Rastering Wear Tests

Several sets of test matrices varying tip geometry, normal load, and number of cycles, were run using the rastering wear mode as described in Chapter 4. This mode collects no quantitative data during the test. A method for quantitative wear measurements was developed in Chapter 5. This testing mode suffers from difficulties due to machine control and wear debris. Figure 7-6 shows SEM micrographs from a test matrix run at a 40 μN normal load while varying tip geometry and number of cycles. The

images in Figure 7-7 and Figure 7-8 show problems that could not be resolved after numerous attempts, discussions, and an extended visit to the equipment manufacturer. The image in Figure 7-7 shows a problem with wear scar extending beyond the prescribed area. This is most likely due to a drift or control problem with the piezo scanner. The image in Figure 7-8 shows a trench that sometimes develops during test runs. No correlation was made due to sample variation, and the phenomenon would occur intermittently on the same sample. In addition to the control problems, Figure 7-8 shows wear debris that was transferred into the wear scar which could confound a wear volume measurement.

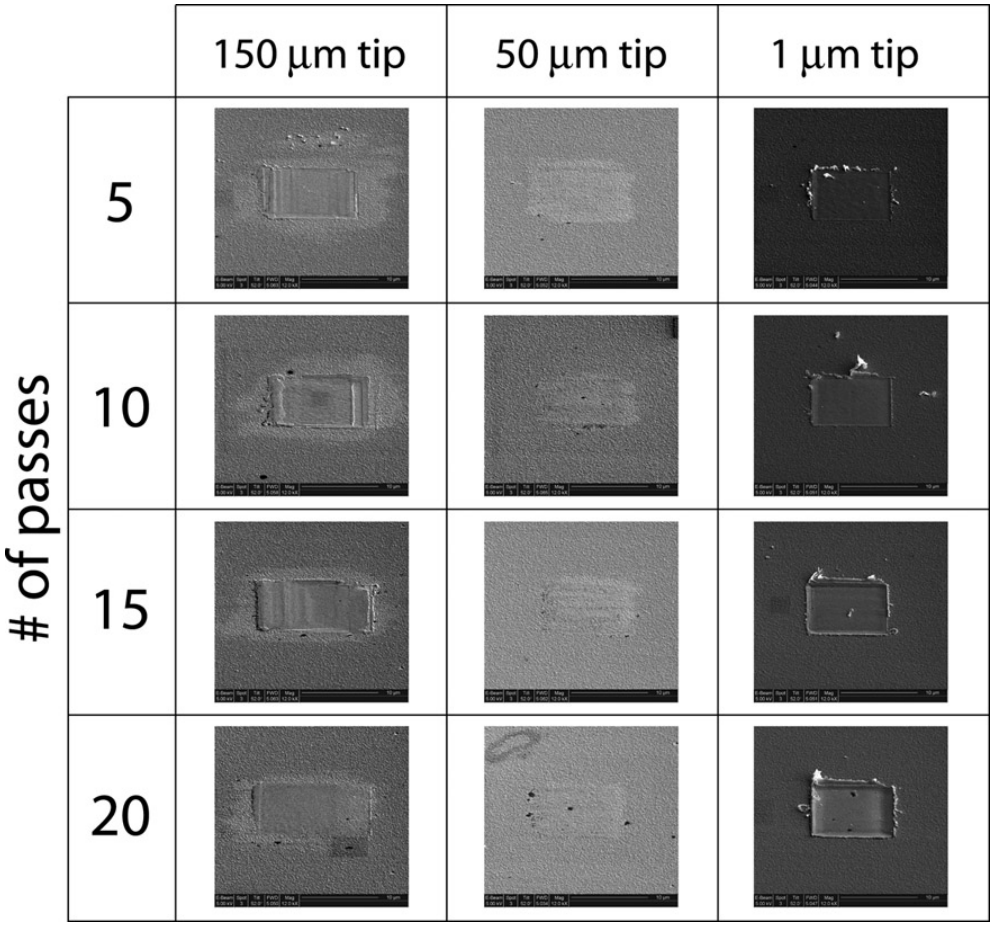

Figure 7-6. SEM micrographs from a rastering wear test matrix with a 40 µN normal load varying tip geometry and number of cycles as indicated.

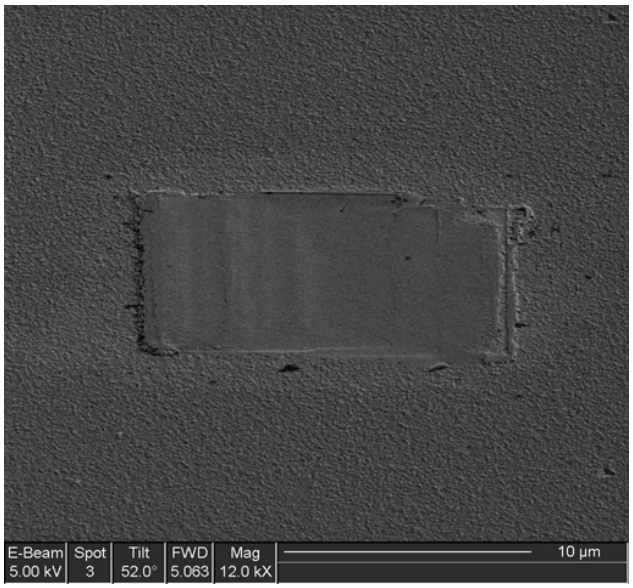

Figure 7-7. SEM micrograph showing a rastering wear anomaly. The wear scar extends outside of the prescribed area especially in the horizontal direction.

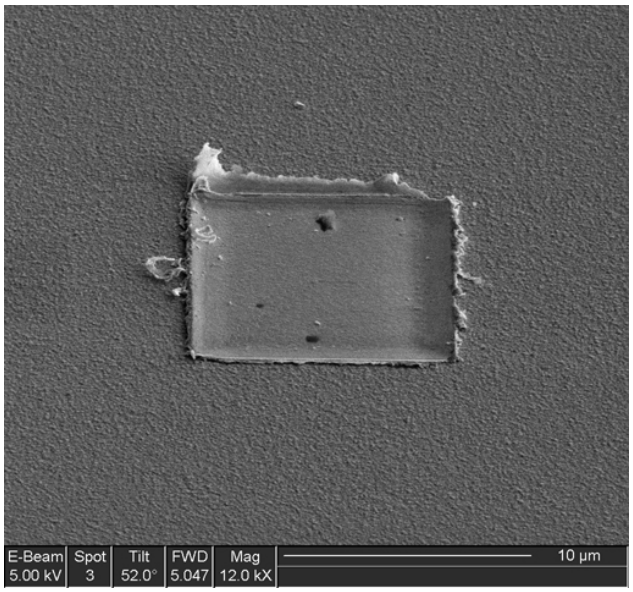

Figure 7-8. SEM micrograph showing a rastering wear anomaly. A trench develops on the right and lower edge of the wear scar. Debris is also transferred to the wear area.

The problems with the rastering wear mode make quantification of tests virtually impossible. At best this method can be used as a qualitative examination method for a relative study. Even in this application, the researcher must be cautious about true results

versus artifacts created by the problems mentioned above. If the rastering problems can be solved, this method along with the wear volume measurement described in Chapter 5 could be useful testing tools.

Reciprocating Wear Tests

Film Failure

Film failure will be defined as the point where the gold film has been removed and the silicon substrate is exposed. The wear track will still contain gold in the contact, and gold will be supporting a portion of the load, but the indenter tip will be in intimate contact with the silicon substrate at the point of failure.

Each wear area was examined upon completion of testing in a FEG SEM to determine if the coating survived the test. When the film has failed, atomic number contrast between the silicon substrate (dark) and the gold film (bright) shows in the micrographs of the wear scar, see Figure 7-9.

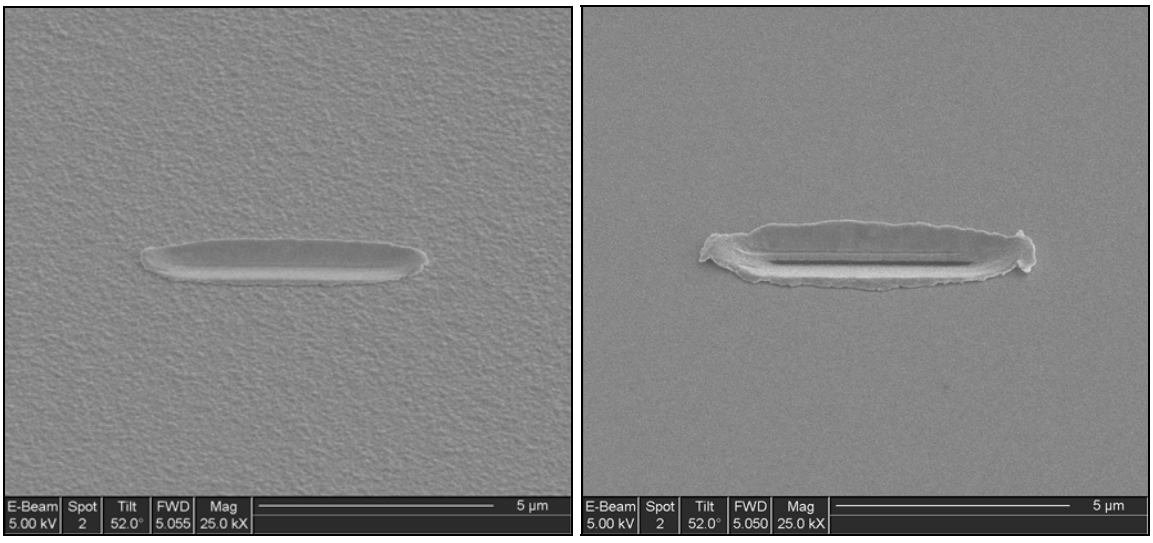

Figure 7-9. SEM micrographs of samples IBS 300 (left) and EBE 200 (right) run for 30 cycles at 500 µN normal loads. Note the dark contrast from the silicon substrate in the center of the wear track on sample EBE 200 due to complete removal of the gold film.

The results in Figure 7-9 will be denoted with an ‘S’ for coatings that survive the number of cycles of the given test, and denoted with an ‘F’ for coatings that show removal of the gold to expose the silicon substrate. One half of the test matrix was run with an evaporated carbon coating on top of the gold coating. Some of these samples exhibited a delamination of the carbon coating which could occur with or without failure of the gold film. Figure 7-10 illustrates each case.

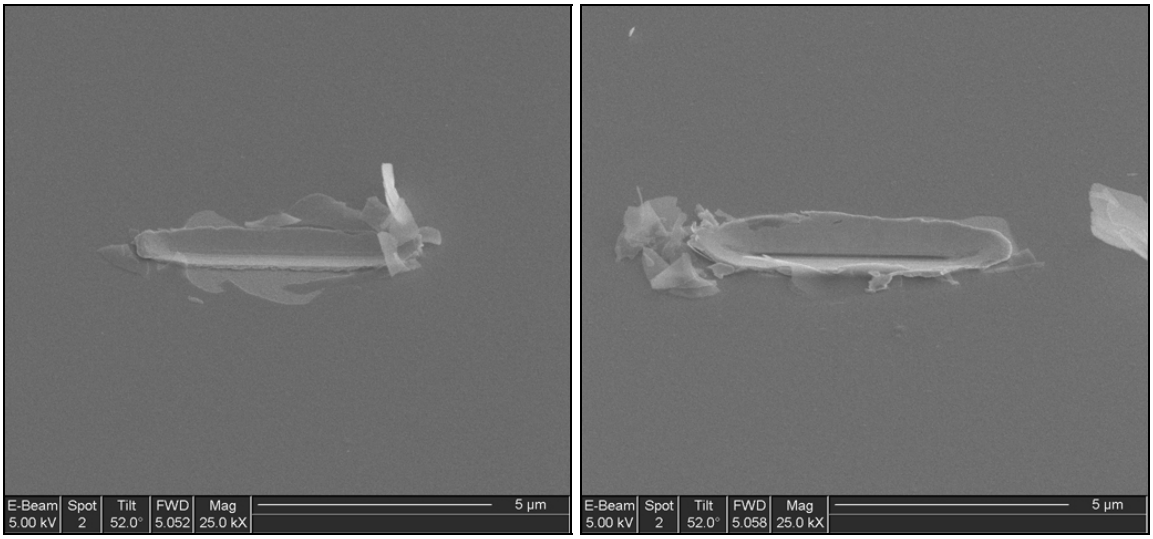

Figure 7-10. SEM micrographs of sample EBE 200 C run for 3 cycles (left) and 30 cycles (right) at 500 µN normal load. On the left, the carbon film has delaminated and the gold is worn but not compromised. On the right, the gold film has been worn through, and the silicon substrate is visible.

Results from Figure 7-10 will be denoted with a ‘D’ for samples that show delamination of the carbon without exposure of silicon below the gold or denoted with an ‘F’ if the silicon is exposed. Each test condition was repeated four times to produce a test matrix with twelve different load and cycle combinations on five different samples both with and without carbon coating on top of the gold coating yielding a total of 480 tests. Every wear scar was imaged to determine whether the coating survived, delaminated, or failed. Micrographs from the repeat tests were very consistent with similar results in at

least three of every set of four. Table 7-3 through Table 7-6 shows results of the micrographs from the entire test matrix. Selected micrographs showing transitions from survived coatings, to delamination, and/or to failure are included in Appendix A.

Gold on silicon without carbon

Five different target thicknesses of gold on silicon were produced by either electron beam evaporation or ion beam sputtering as described in Chapter 2. Table 7-3 summarizes the micrograph results for tests with a 100 μN normal load using the designations described above.

Table 7-3. Results of SEM micrographs from gold on silicon samples with 100 μN normal load. Designations are 'S' for coatings that survived to the number of cycles shown, or 'F' for coatings that have exposed silicon.

cycles	*EBE 20*	*IBS 100*	*EBE 200*	*IBS 300*	*EBE 500*
0.5	F	S	S	S	S
1	F	S	S	S	S
3	F	S	S	S	S
10	F	S	S	S	S
30	F	S	S	S	S
100	F	S	S	S	S
300	F	S	S	S	S

As seen in Table 7-3, all coatings survived up to 300 cycles with the exception of the EBE 20 coating with a target thickness of 20 nm which had failed by the first ½ cycle. Table 7-4 summarizes the microscopy results for tests with a higher normal load of 500 μN. Here again the sample EBE 20 did not survive any number of reciprocations. This is an expected result because as in most applications, higher normal loads result in more material removal. Sample IBS 100 shows that the coating survived the first ½ cycle but the table entry for the one cycle test is 'S/F.'

Table 7-4. Results of SEM micrographs from gold on silicon samples with 500 μN normal load. Designations are 'S' for coatings that survived to the number of cycles shown, or 'F' for coatings that have exposed silicon.

cycles	*EBE 20*	*IBS 100*	*EBE 200*	*IBS 300*	*EBE 500*
0.5	F	S	S	S	S
1	F	S/F	S	S	S
3	F	F	S	S	S
10	F	F	S	S	S
30	F	F	F	S	S
100	F	F	F	S	S
300	F	F	F	S	S

The designation 'S/F' is chosen because the sample shows small exposed areas of silicon sporadically in the track and is the onset of film failure. The gold film is still intact through most of the contact and is expected to exhibit the tribological properties of the diamond indenter tip sliding on a gold film, see Figure 7-11.

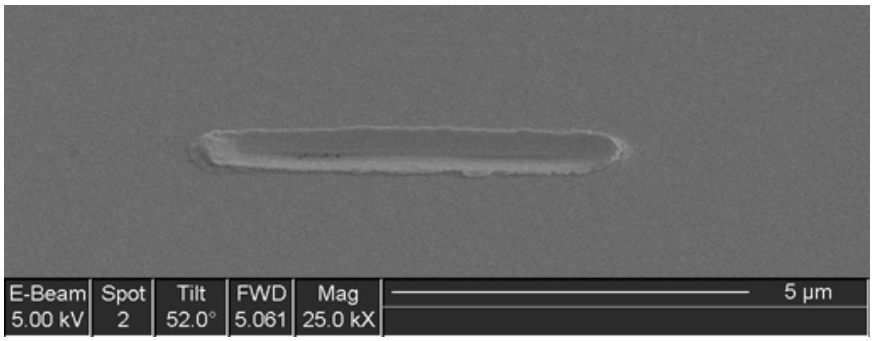

Figure 7-11. SEM micrograph of sample IBS 100 after 1 cycle of sliding with 500 μN normal load. Note the small dark spots in the center at each end of the wear track indicating exposed silicon substrate.

A note of interest from Table 7-4 is that the survival of the gold coating based on number of cycles is not linearly dependent on film thickness. Figure 7-12 is a plot of the targeted film thickness versus the maximum number of cycles observed without coating failure. Since 300 was the maximum number of cycles in the tests, samples IBS 300 and

EBE 500 data points are marked with arrows to show the samples may have survived beyond the indicated data point.

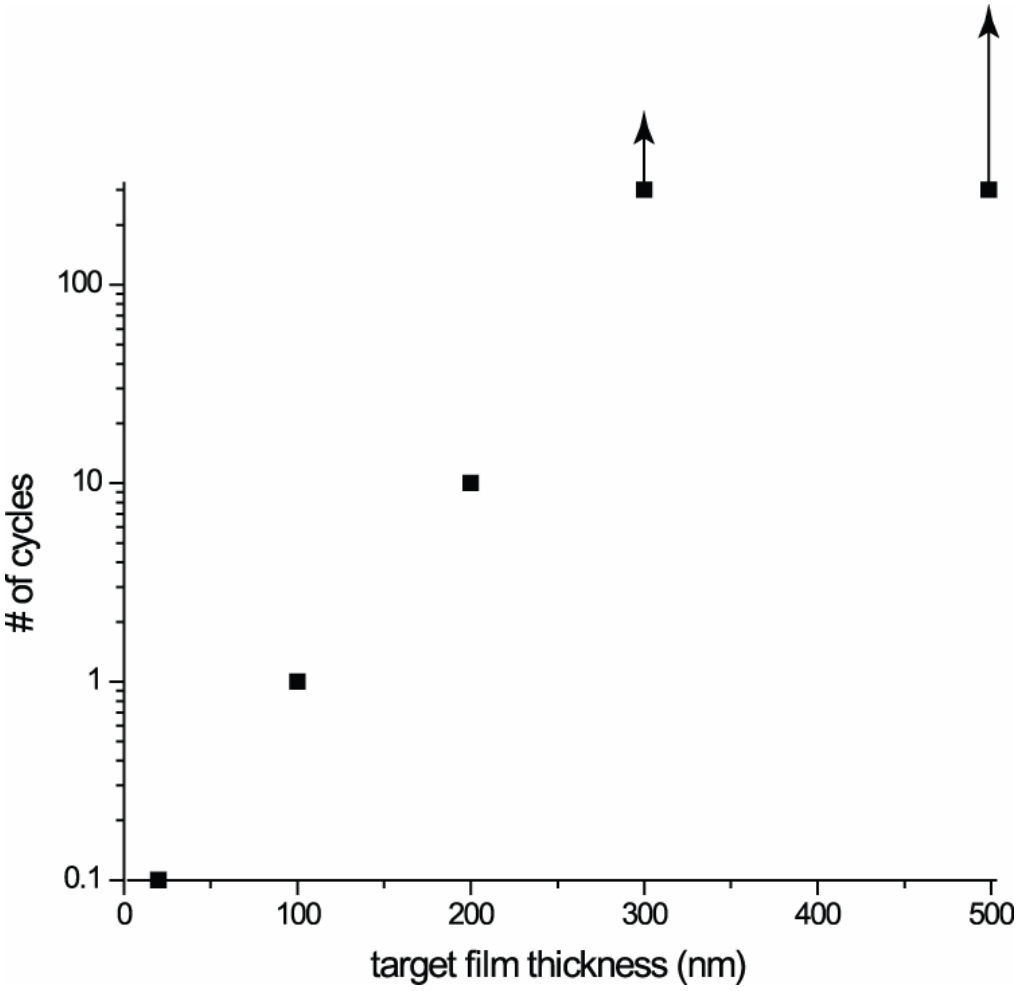

Figure 7-12. Nominal film thickness versus number of cycles prior to film failure. Note that the 300 nm and 500 nm thick films did not show failure at the maximum 300 test cycles. Number of cycles are plotted on log scale.

Carbon on gold on silicon

A layer of amorphous carbon, approximately 60 nm in thickness, was deposited on a set of samples as described in Chapter 2 to explore the effects of an electrically conductive friction modifying layer. The results from the SEM examination of the wear tests with 100 μN normal load are presented in Table 7-5. In this table the designation of 'D' for coatings that show delamination as described above is included.

Table 7-5. Results of SEM micrographs from carbon on gold on silicon samples with 100 μN normal load. Designations are 'S' for coatings that survived to the number of cycles shown, 'D' for coatings that exhibited delamination of the amorphous carbon, or 'F' for coatings that have exposed silicon.

cycles	*EBE 20*	*IBS 100*	*EBE 200*	*IBS 300*	*EBE 500*
0.5	S	S	S	S	S
1	S	S	S	S	S
3	S	S	S	S	S
10	S	S	S	S	S
30	S	S	D	S	S
100	F	S	D	S	S
300	F	S	F	S	F

The effect of amorphous carbon is significant when comparing Table 7-5 with Table 7-3. The sample EBE 20C appears to have survived for at least 30 cycles with the amorphous carbon where without it failed before one complete cycle. With the addition of amorphous carbon, the carbon film has delaminated by 30 cycles on the EBE 200C sample, and gold film failure is seen at 300 cycles.

Table 7-6 shows the results from micrographs taken from a sample matrix run on carbon on gold on silicon. The results are similar to those seen in Table 7-4 with the exception of the IBS 100C sample. With the carbon coating, the life of this sample has been extended beyond 3 cycles.

Table 7-6. Results of SEM micrographs from carbon on gold on silicon samples with 500 μN normal load.

cycles	*EBE 20*	*IBS 100*	*EBE 200*	*IBS 300*	*EBE 500*
0.5	F	S	D	S	D
1	F	S	D	S	D
3	F	D	D	D	D
10	F	F	D	D	D
30	F	F	F	D	D

Electron Microscopy Cross Sections of Wear Scars

A dual beam FIB SEM was used to make cross sections of the wear tracks as described in Chapter 6. While the Hysitron Triboindenter is capable of measuring displacement, the instrument is sensitive to thermal drift during the extended amount of time required to run a reciprocating wear test. Figure 7-13 shows a plot of vertical tip displacement versus lateral tip displacement for a 30-cycle test.

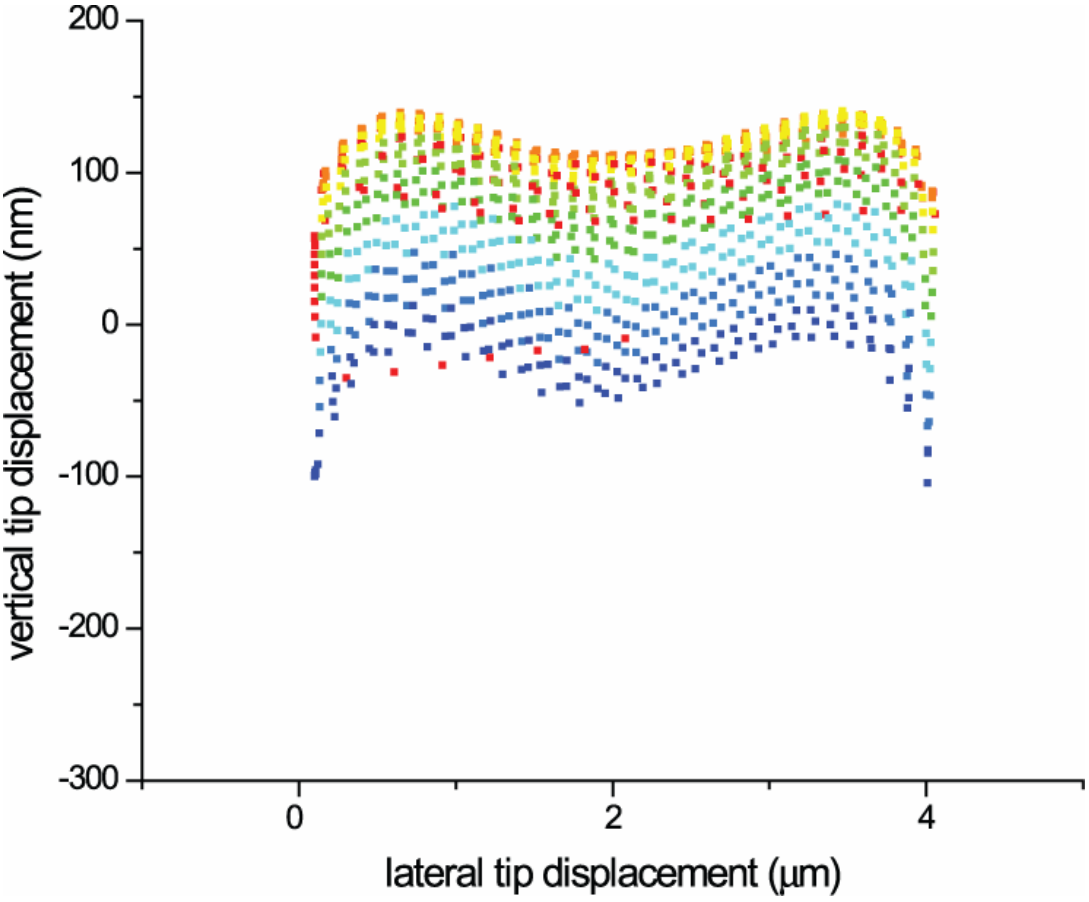

Figure 7-13. Plot of vertical tip displacement versus lateral displacement for a 30-cycle reciprocating test. Points are plotted in red at time=0 and progress in color through the spectrum (ROYGB) as time increases.

The data points are shown in color beginning in red at the start of the test and as time goes on, the color of the points transition through the spectrum to end in blue at the end of the test. The initial vertical displacement of the tip is in the 100 nm range and

increases in displacement initially. Thermal drift eventually overtakes the vertical displacement and the tip appears to be at a negative displacement at the end of the test. This contradicts force measurements and electron microscopy of cross sections. For these reasons, displacement is measured using electron microscopy by taking cross sections from interrupted tests. Figure 7-14 shows a transverse cross section from a wear scar. The image was produced and tilt corrected as described in Chapter 6.

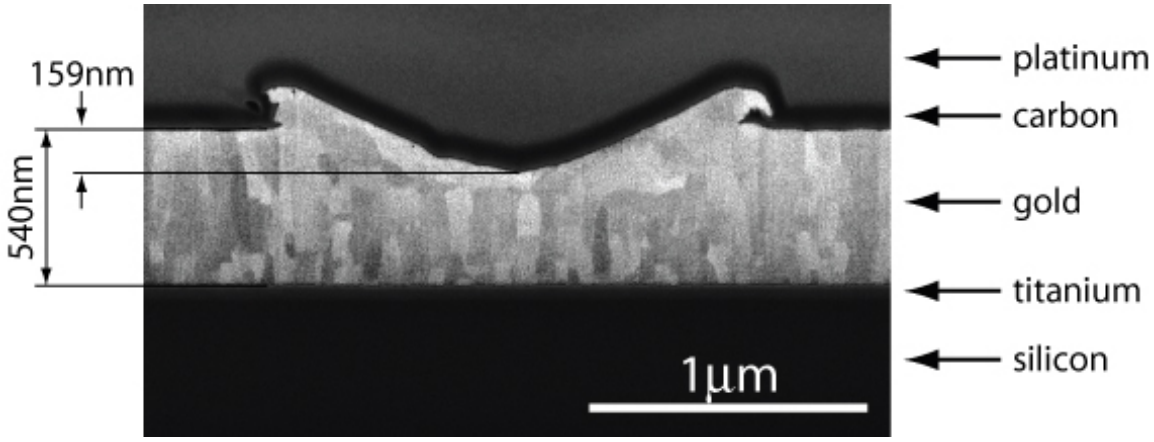

Figure 7-14. FIB/SEM transverse cross section of a wear scar run on sample EBE 500 for 10 cycles with a 500 µN normal load. Measurements of the film thickness and the depth of the wear scar from the original surface are indicated.

In addition to film thickness and wear scar measurements, the cross sectional image shows the morphology of the film damage. Note the curling of the material exuded from the contact area on the right side. Features such as these and sub-surface damage including fracture and delamination could not be investigated with a top-down microscopy technique. The microstructure of the gold film is revealed in this image through channeling contrast. Several researchers have demonstrated and explained FIB secondary electron channeling contrast using the ion beam as the incident source and a secondary electron detector [48-50]. Samples from this study could not be characterized using channeling contrast produced with the ion beam due to extreme damage caused

even at low beam currents. The image in Figure 7-14 is produced by polishing the surface with a low current (30 pA) ion beam and switching the incident beam to the electron beam with a 5 kV accelerating voltage, 30 μm aperture and #2 spot size. This type of image is challenging to produce in conventional SEMs because the technique is sensitive to surface contamination and topography. In the FIB, a nascent polished surface can be easily produced.

The microstructure revealed in Figure 7-14 shows columnar grains typical of a deposition process. Presumably, grains nucleate on the surface with random orientations, but will be overtaken by grains oriented in the fast growth direction. The results from XRD in Chapter 6 show a strong (111) orientation, suggesting this is the preferred growth orientation for gold which is substantiated in the literature [51]. A highly deformed plastic zone is visible below the contact area. A detailed study of plastic zone evolution could be conducted with this imaging technique.

Uncoated samples from the wear matrix with a 500 μN normal load were chosen for measurements using the cross sectional FIB/SEM technique. Figure 7-15 shows a plot of displacement below the original surface versus number of cycles as measured from cross sections. Wear tests were run with incremental number of cycles so data could be collected for various cycles. The numbers of cycles were as follows: 0.5, 1, 3, 10, 30, 100, and 300. If penetration of the film was observed in a cross section, displacement was not plotted because the actual number of cycles at penetration can not be determined. Sample EBE 20 is not plotted because film penetration was apparent after the first half cycle. The figures used to measure the displacement data have been included in Appendix B.

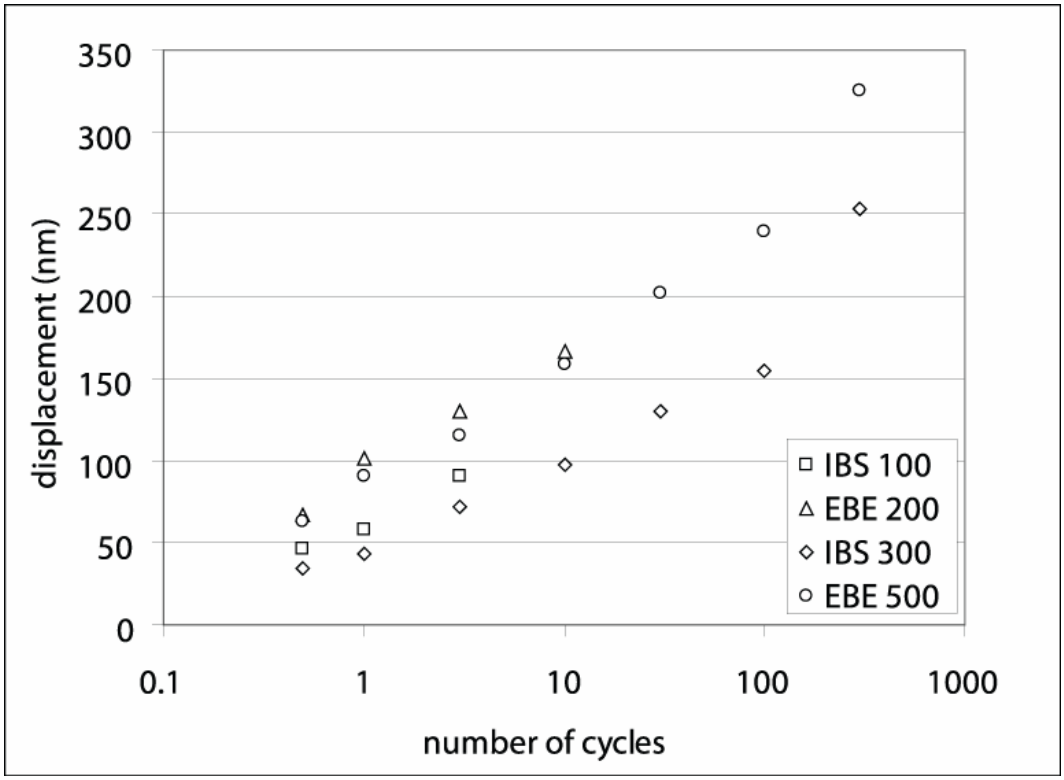

Figure 7-15. Depth of wear scar versus number of cycles for samples run at 500 μN normal load.

It is interesting to note that both electron beam evaporated (EBE) samples behave nearly identical up to the failure of EBE 200. The ion beam sputtered (IBS) samples also behaved similarly with IBS 100 showing slightly more displacement than IBS 300. Considering displacement into the film below the original surface as a measure of wear, the EBE samples showed more wear than both IBS samples and IBS 100 showed slightly more wear than IBS 300.

A plot of fraction of the coating penetrated versus number of cycles is constructed in Figure 7-16. In this plot the displacement is normalized by the coating thickness to give the fraction of penetration. Again, if the coating had failed, the number of cycles at the observed failure was not plotted, and since sample EBE 20 had failed at the first half pass it does not show up in the plot.

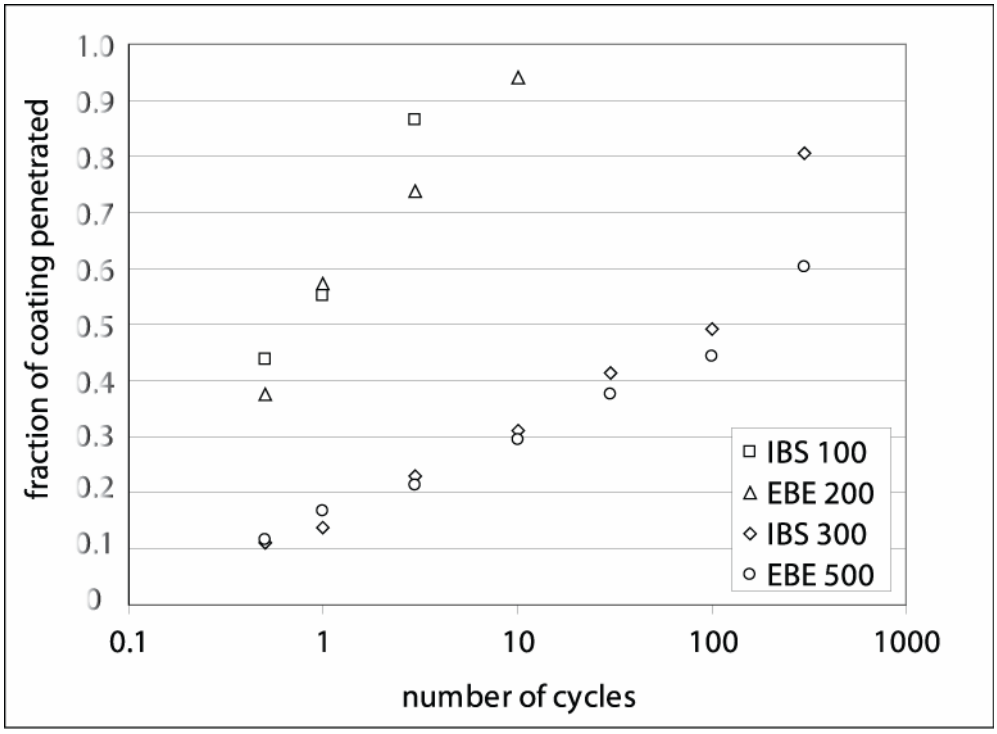

Figure 7-16. Plot showing fraction of coating depth penetrated versus number of cycles for samples run at 500 μN normal load.

Now it appears the two thinner film samples, IBS 100 and EBE 200, behave similarly, as do the two thicker film samples IBS 300 and EBE 500. Figure 7-16 shows good agreement with Table 7-4 between the two characterization methods to determine the point of film failure with the exception of Sample IBS 100, appearing to have failed before 3 cycles in Table 7-4, and after 3 cycles in Figure 7-16. This may be explained by the coating first breaking down sporadically along the wear track and slight variation in cycle number at failure from tests run with repeat conditions. The fraction of penetration appears to be linear when plotted versus the log of the number of cycles to failure which could lead to a coating lifetime prediction based on an extrapolation. The EBE 200 data appears to fall on a line nearly all of the way to failure, however, the last point plotted for IBS 100 and IBS 300 deviated from a line fit through the rest of the points for these

samples. The deviation occurs somewhere between 50% and 80% of the film thickness. More data is needed to determine if this could be a viable method for life prediction.

Friction Measurements

Metallic friction, as described in Chapter 1, is comprised of two components, the force of deformation, and the force to slide one interfacial surface [4]. Reducing the contact pressure below the yield point of the material will result in an elastic contact, and the force of plastic deformation should be eliminated. The contact pressure can be reduced by two methods, increasing the contact area or reducing the normal load. The tests were run using the well characterized diamond indenter previously described and the load resolution is such that a pure elastic contact with this tip geometry is not possible on the Hysitron. To examine the friction from an elastic contact, tests were run on the CSM Microtribometer in addition to the tests run on the Hysitron Triboindenter.

Hysitron Triboindenter friction measurements

Lateral force is collected during the wear tests on the Hysitron Triboindenter, and is normalized with the normal load to determine a friction coefficient. Figure 7-17 shows friction coefficient versus the number of cycles for gold on silicon samples without carbon coating run at 500 μN. Testing on samples EBE 20, IBS 100, and EBE 200 was terminated at 30 cycles because the film had been compromised by this point on all three. Table 7-4 shows that sample EBE 20 had failed by the first half cycle. The friction data from this sample is much lower than for the others. The friction starts out at 1.6 and decreases to 1.0. This low friction coefficient is probably more representative of diamond sliding on silicon than diamond sliding on gold. Sample IBS 100 shows friction above 0.25 for less than 3 cycles of sliding. Both cross sectional microscopy and top down microscopy show the film failure between 1 and 3 cycles for IBS 100. Sample

EBE 200 shows failure between 10 and 30 cycles and its friction coefficient drops below 0.25 after 10 cycles. Sample IBS 300 has not failed at 300 cycles but the cross sectional image shows the coating is close to penetration, see Figure 7-16. The dashed line shown on the plot represents friction values where the gold film has been penetrated and the sliding contact is comprised of a combination of gold and silicon. Below the grey region, diamond sliding on silicon is a major component of the friction coeffiecent. For gold film samples with a 500 μN normal load, a friction coefficient below 0.25 indicates film failure.

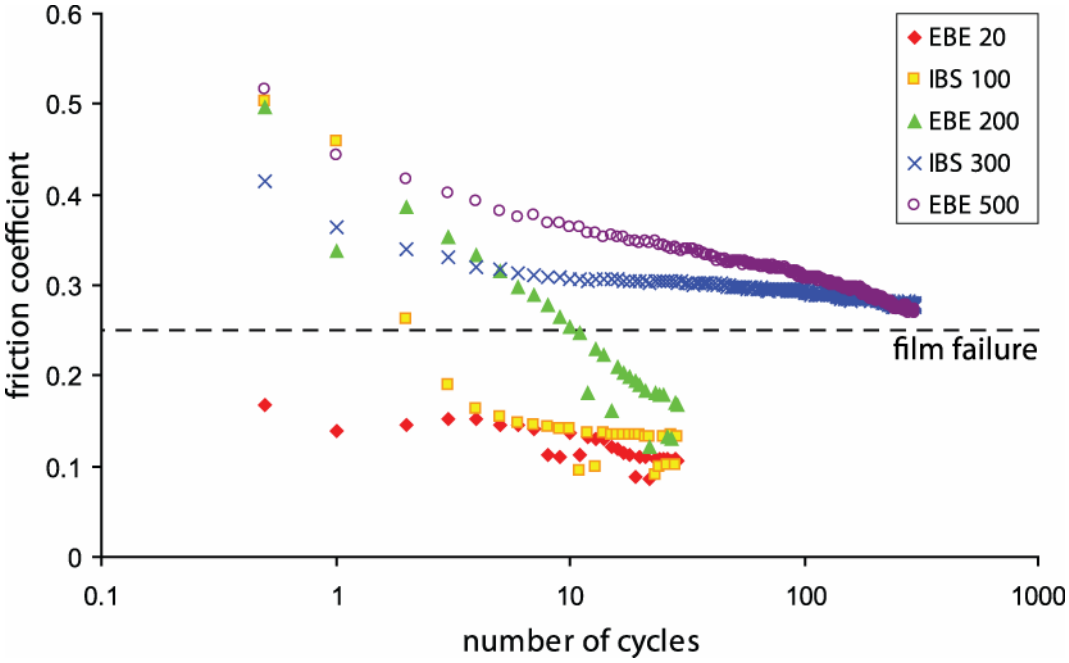

Figure 7-17. Friction coefficient versus number of cycles in log scale for gold on silicon samples without carbon run at 500 μN normal load.

Friction results from the gold on silicon samples without carbon coating run at 100 μN normal load are plotted in Figure 7-18. Again the friction coefficient is much lower for the sample EBE 20 that failed as early as the first half cycle, see Table 7-3. All other samples survived the entire test at 100 μN normal load and their friction coefficient remained above 0.25.

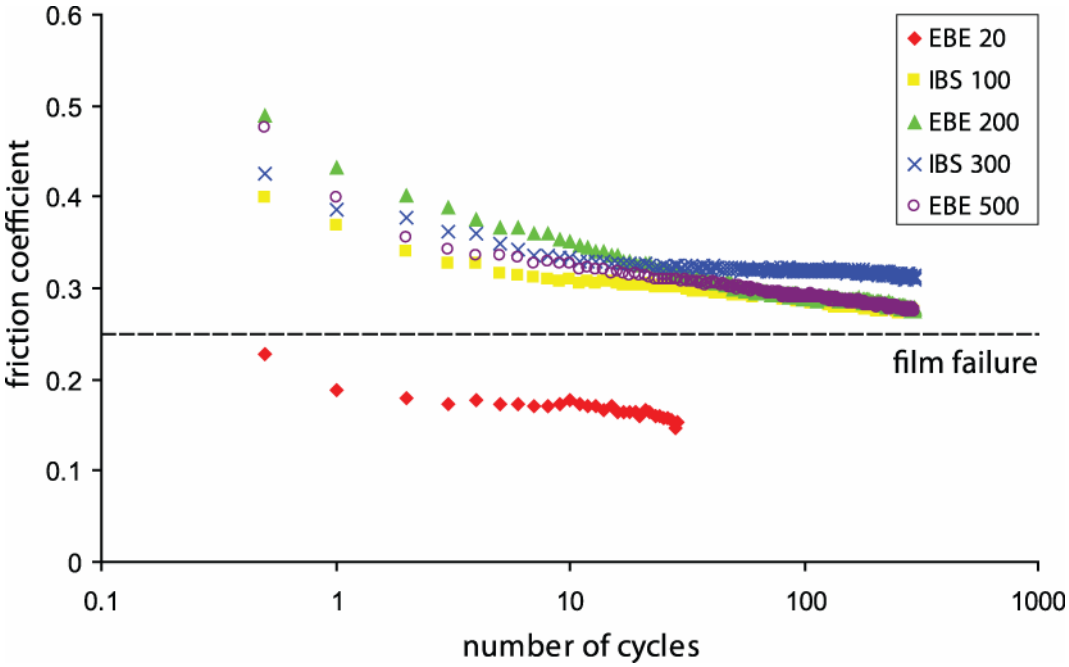

Figure 7-18. Plot of friction coefficient versus number of cycles on a log scale for gold on silicon samples without carbon coating run at 100 uN normal load.

Figure 7-19 shows friction coefficient results for gold on silicon samples with carbon coating run at 500 μN normal load. The dashed line indicates a friction coefficient of 0.25. Again samples exhibit friction coefficients below 0.25 at or near the number of cycles when the gold film is penetrated. Comparing Table 7-6 to Figure 7-19, EBE 20C shows failure immediately and the friction coefficient begins below 0.25. Sample IBS 100C fails between 3 and 10 cycles from the table, and the friction coefficient drops below 0.25 at 5 cycles. Table 7-6 shows sample EBE 200C failed between 10 and 30 cycles, and the friction coefficient drops below 0.25 at 14 cycles. The remaining two samples survived beyond 30 cycles and their friction coefficients remained above 0.25. Friction data was lost for these samples beyond 30 cycles due to an error in the wear cycle load function code. Friction data does not seem to be sensitive to the carbon coating at the 500 μN normal load, and the data does not show a correlation to the carbon delamination event.

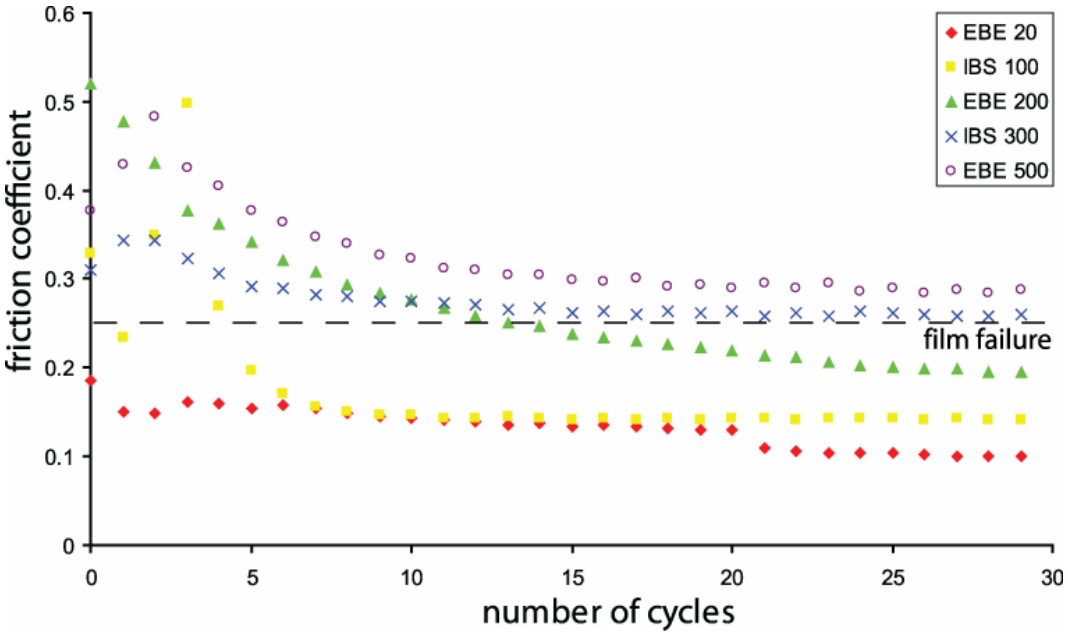

Figure 7-19. Plot of friction coefficient versus number of cycles for gold on silicon samples with carbon coating run at 500 uN normal load. Dashed line indicates a friction coefficient of 0.25.

The friction data for gold on silicon samples coated with carbon run at 100 μN load shows significant differences from the previous results. Table 7-5 shows the carbon coating survived on all samples up to 30 cycles with the exception of a delamination of EBE 200C at the 30-cycle micrograph. The friction data for these tests is plotted in Figure 7-20. The friction coefficient for all samples ranged from 0.12 to 0.17 and the point of delamination on sample EBE 200 was not detected in the friction data. Friction data beyond 30 cycles was lost for these samples due to the same error in the wear cycle load function mentioned previously. The lower normal load of 100 μN allows friction measurements of the diamond indenter tip sliding against the amorphous carbon coating to be measured whereas the 500 μN normal load friction is dominated by properties of the gold.

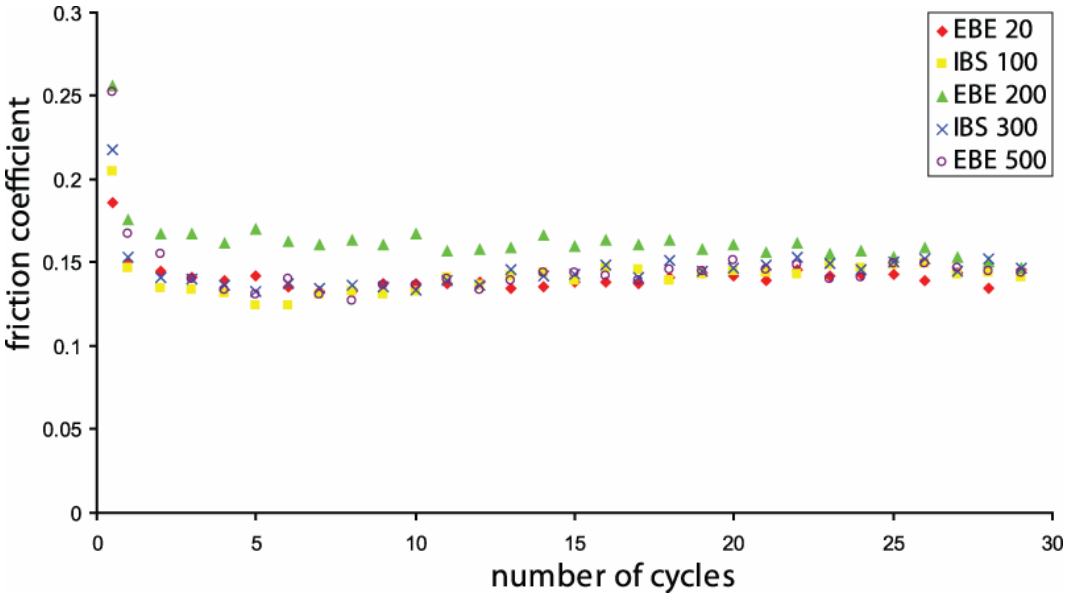

Figure 7-20. Plot of friction coefficient versus number of cycles for gold on silicon samples with carbon coating run at 100 uN normal load.

CSM microtribometer friction coefficient measurements

As mentioned previously, an elastic contact cannot be accomplished with the current tip geometry on the Hysitron Triboindenter. Although a technique has been developed in this study to target low contact pressures in the Hysitron, a CSM Microtribometer was employed as a matter of convenience.

To target a completely elastic contact, the maximum pressure should be below the hardness. Sample EBE 200 was chosen for testing. From the hardness analysis, the lowest calculated hardness for this sample was determined to be 1.4 GPa. If the relationship $H=3\sigma_y$ holds true for this material, the yield strength should be 470 MPa. Coarse grained annealed gold is reported to have a yield strength of 100 MPa - 120 MPa [41, 52]. The onset of plasticity can occur at pressures as low as $1.1\sigma_y$ [37]. With all these considerations, a maximum pressure below 100 MPa was targeted to ensure an elastic contact. Based on a 2 mm diameter pin of Al_2O_3, with a normal load of 1.5 mN determined by a cantilever flexure, in contact with gold, the maximum pressure was

calculated to be 92 MPa using Herztian elastic contact mechanics. Reciprocating tests were run for 1, 3, 7, 10, 30, 70, and 100 cycles and are plotted in Figure 7-21.

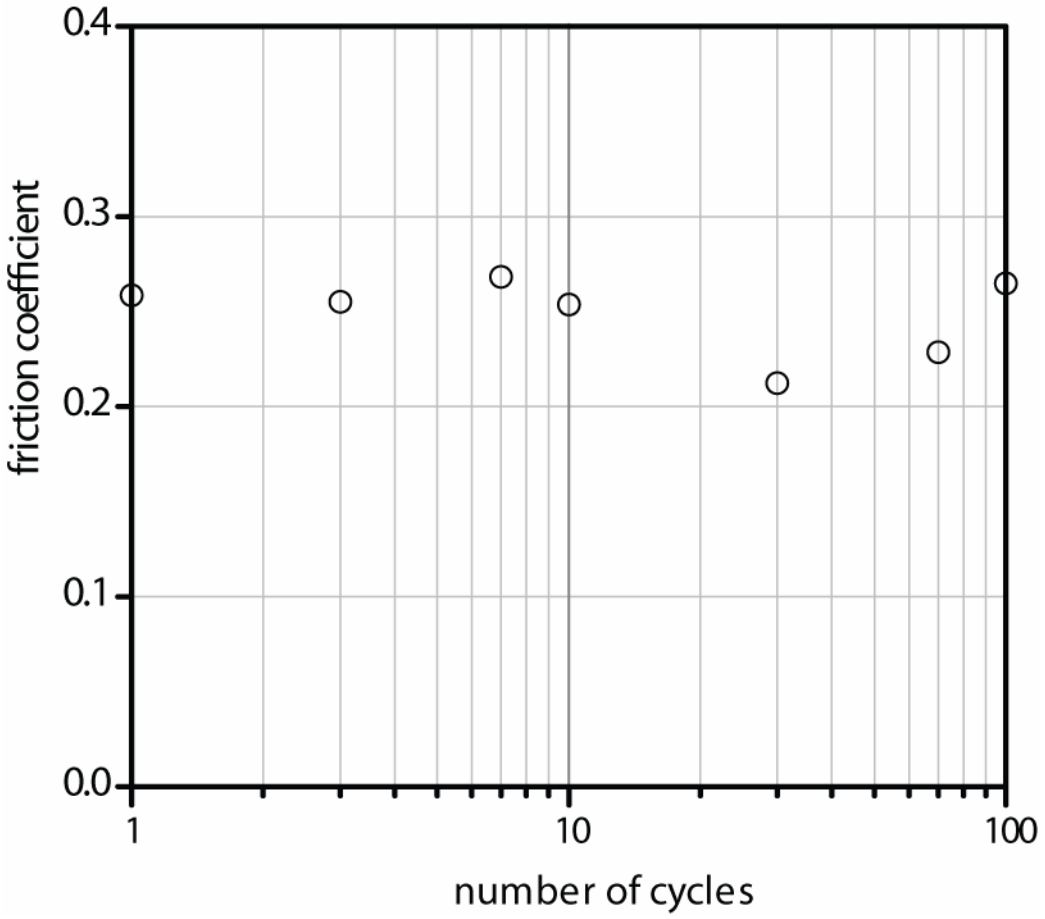

Figure 7-21. Friction coefficient versus number of cycles plotted on log scale for a contact pressure of 92 MPa run on sample EBE 200.

The friction coefficient from Figure 7-21 should contain no plastic deformation component and should be representative of the interfacial sliding term μ from Bowden and Tabor's model [4]. Virtually no deformation was detected in SEM examination of the wear area on this test sample. This result suggests for the samples that failed on the Hysitron, the contact remained plastic, removing material until failure. A combination of work hardening and increased contact area might eventually develop an elastic contact on

thicker samples resulting in a more wear resistant contact, but testing for higher numbers of cycles is required to investigate this possibility.

CHAPTER 8
CONCLUSIONS

Considerations for testing thin films on the nanodisplacement level were examined and addressed. A test matrix was designed to investigate thin film wear testing over a range of film thickness, normal load, and number of repeat cycles. Gold was chosen as a test film for its well characterized properties and applications in MEMS. A variety of sample preparation techniques were employed with best results obtained from commercially processed electron beam evaporated and 'in-house' ion beam sputtered coatings.

Various testing modes and parameters were explored. Reciprocating linear testing was demonstrated in the Hysitron Triboindenter and proved to be the best method for data collection and reproducibility. A method to mount a wide range of tip materials and geometries was developed to test various contacts and pressures.

A systematic approach was designed to locate wear regions throughout testing and characterization. An optics offset calibration method was developed to overcome the limitations of light optical microscopy. Wear test placement was repeatable within 0.5 μm.

A variety of characterization techniques including nanoindentation, x-ray diffraction, ion beam milling, and electron microscopy were employed to analyze sample properties and quantify results. Established indentation models overestimate hardness in materials that exhibit pile-up. An alternative model was formulated and applied to load displacement data. Results of this alternative model show good agreement with the Hall-

Petch relationship for the grain size of the films tested. Wear test lateral load was measured with the Hysitron Triboindenter transducer and showed good repeatability. Displacement data was characterized by direct measurement from SEM micrographs due to drift issues during extended testing times. Friction coefficient showed good agreement with an alternate testing method and proved to be a good indication of film failure.

The methodology developed in this study gives well characterized, reproducible, quantitative data from reciprocating wear tests on the nanodisplacement level. The data set from this study will be extended to predict wear rates and friction coefficients using finite element analysis.

APPENDIX A
SEM IMAGES OF EXPERIMENTAL WEAR MATRIX

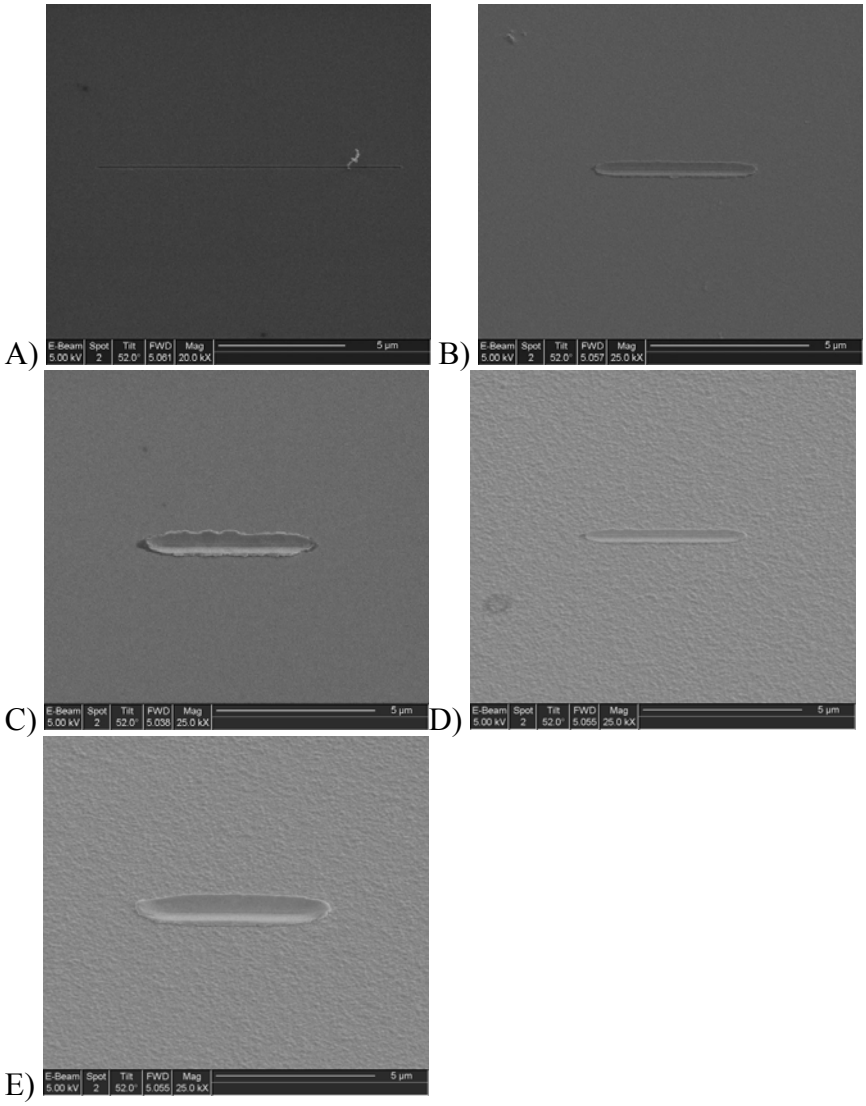

Figure A-1. Images showing the wear scar of gold on silicon at 100 μN load normal load. Conditions showing transitions from Table 7-3 are included. A) EBE 20, half cycle. B) IBS 100, 300 cycle. C) EBE 200, 300 cycle. D) IBS 300, 300 cycle. E) EBE 500, 300 cycle.

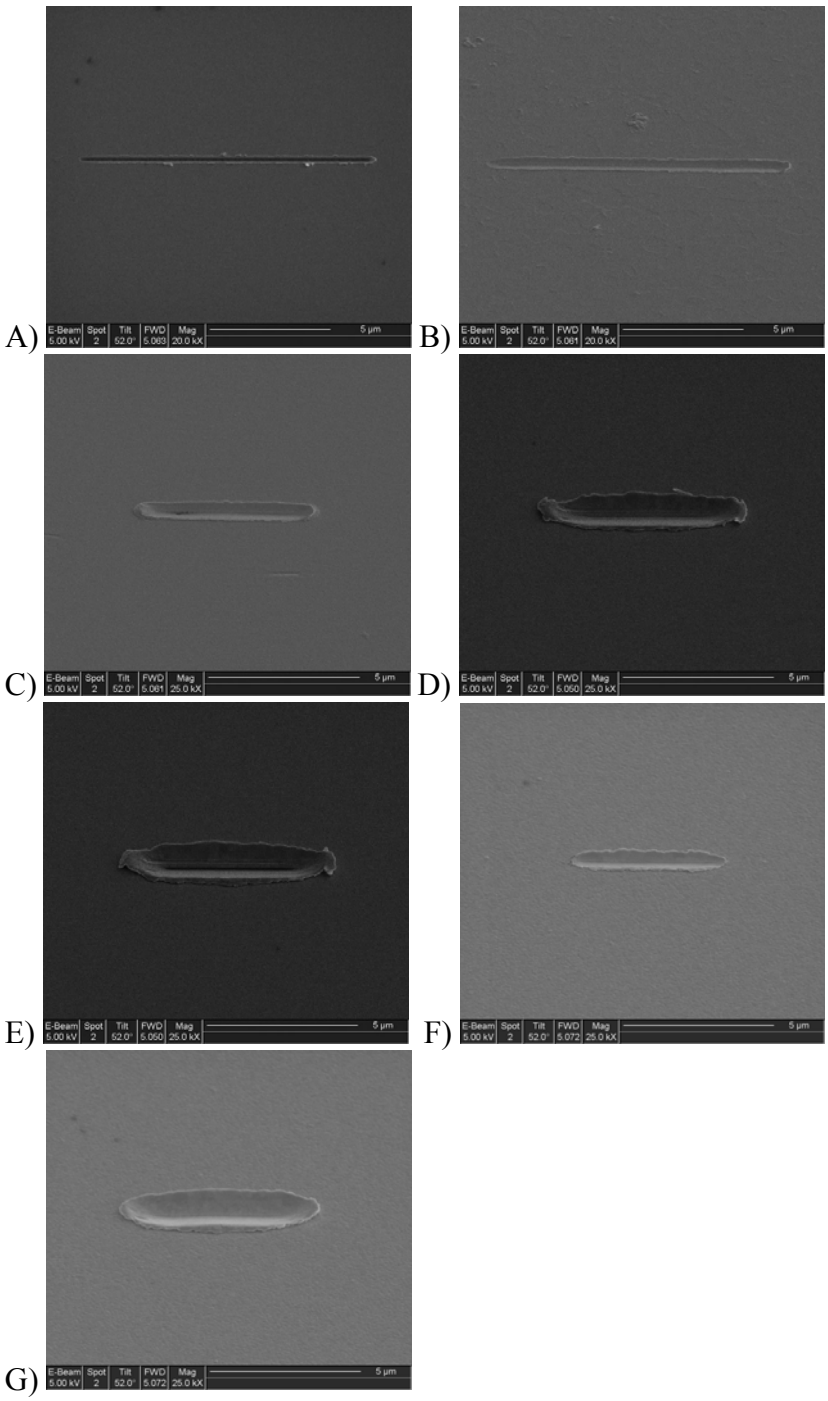

Figure A-2. Images showing the wear scar of gold on silicon at 500 μN load normal load. Conditions showing transitions from Table 7-4 are included. A) EBE 20, half cycle. B) IBS 100, half cycle. C) IBS 100, 1 cycle. D) EBE 200, 10 cycle. E) EBE 200, 30 cycle. F) IBS 300, 300 cycle. G) EBE 500, 300 cycle.

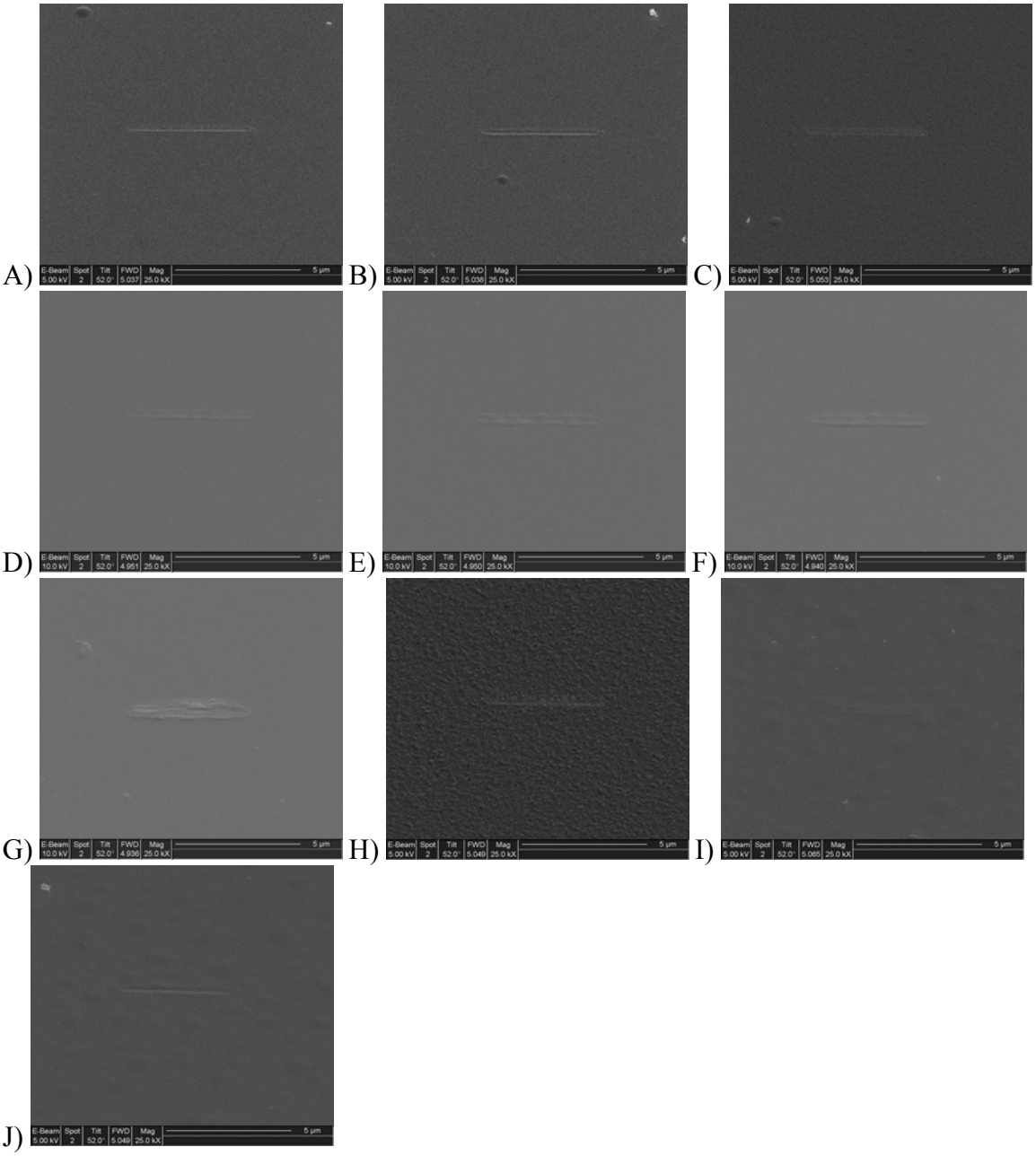

Figure A-3. Images showing the wear scar of carbon on gold on silicon at 100 μN load normal load. Conditions showing transitions from Table 7-5 are included. A) EBE 20, 30 cycle. B) EBE 20, 100 cycle. C) IBS 100, 300 cycle. D) EBE 200, 10 cycle. E) EBE 200, 30 cycle. F) EBE 200, 100 cycle. G) EBE 200, 300 cycle. H) IBS 300, 300 cycle. I) EBE 500, 100 cycle. J) EBE 500, 300 cycle.

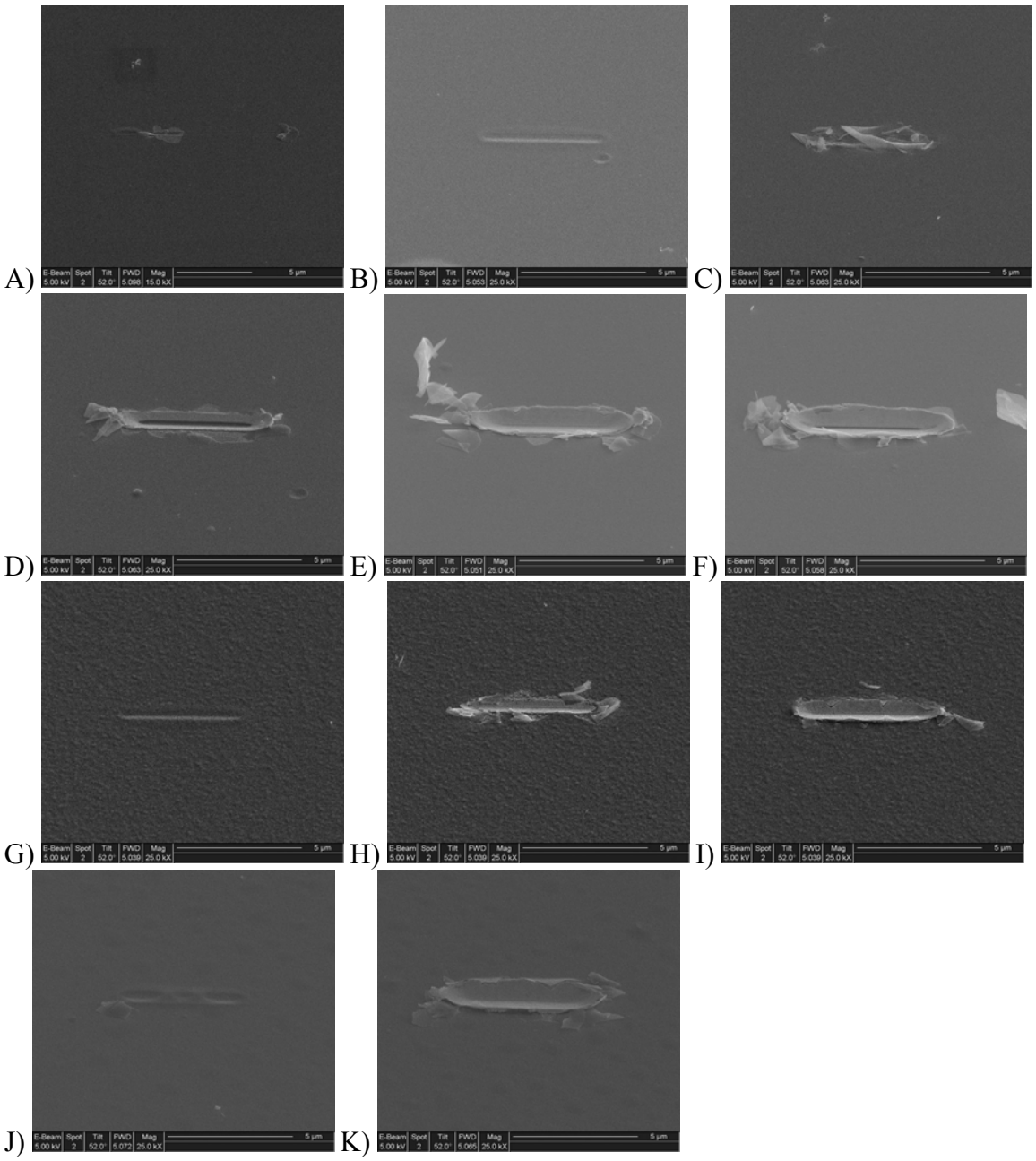

Figure A-4. Images showing the wear scar of carbonon gold on silicon at 500 μN load normal load. Conditions showing transitions from Table 7-6 are included. A) EBE 20, half cycle. B) IBS 100, 1 cycle. C) IBS 100, 3 cycle. D) IBS 100, 10 cycle. E) EBE 200, 10 cycle. F) EBE 200, 30 cycle. G) IBS 300, 1 cycle. H) IBS 300, 3 cycle. I) IBS 300, 30 cycle. J) EBE 500, half cycle. K) EBE 500, 30 cycle.

APPENDIX B
SEM CROSS SECTIONS USED FOR DISPLACEMENT MEASUREMENTS

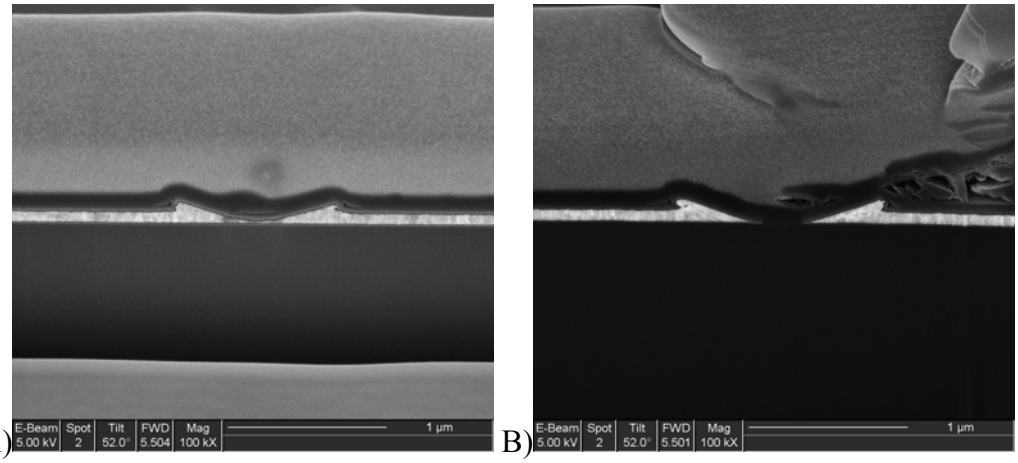

Figure B-1. SEM/FIB cross section of sample IBS 100 at 500 µN normal loads. A)1 cycle. B) 3 cycles.

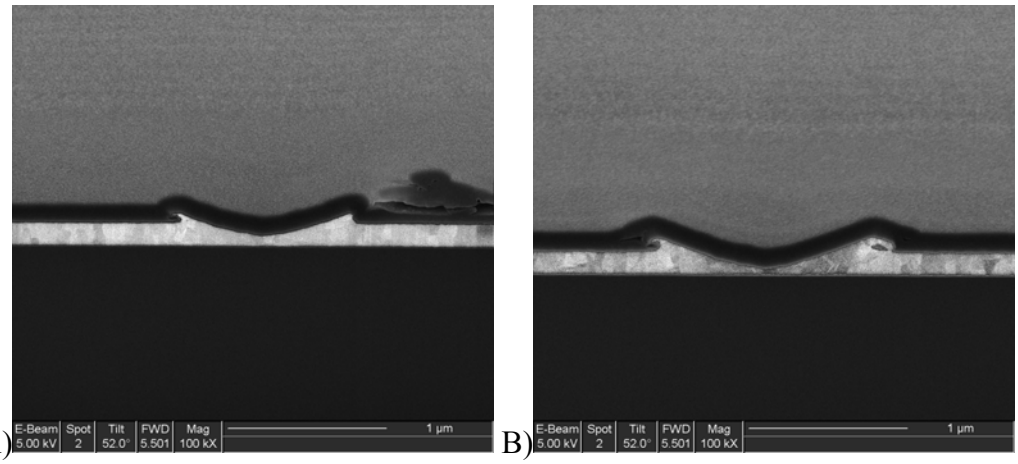

Figure B-2. SEM/FIB cross section of sample EBE 200 at 500 µN normal loads. A)1 cycle. B) 3 cycles.

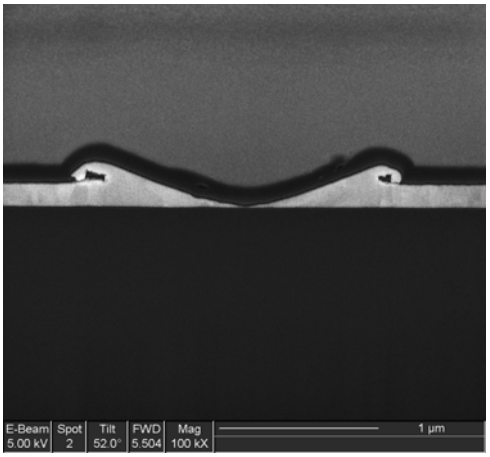

Figure B-3. SEM/FIB cross section of sample EBE 200 at 500 µN normal loads and 10 cycles.

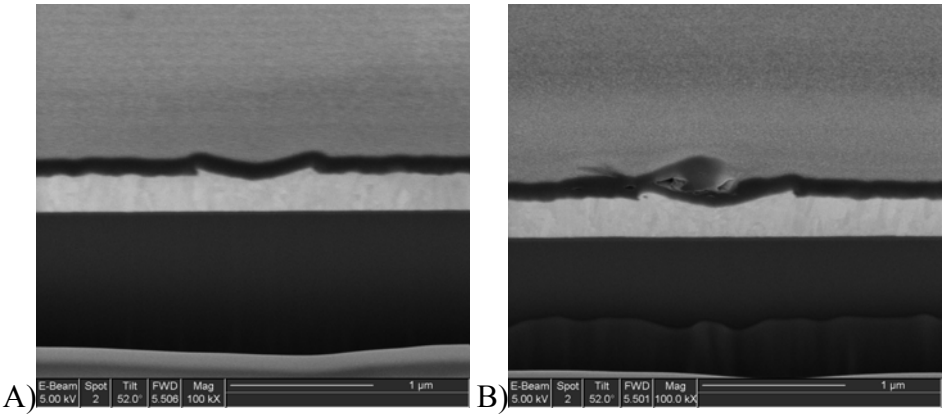

Figure B-4. SEM/FIB cross section of sample IBS 300 at 500 µN normal loads. A)1 cycle. B) 3 cycles.

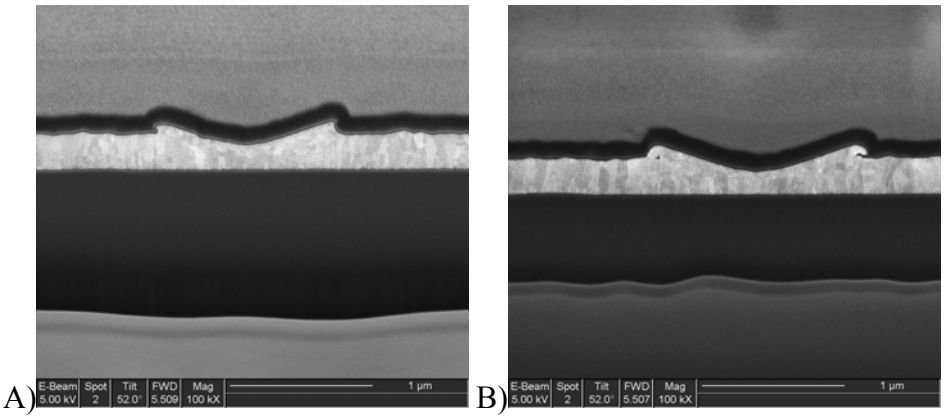

Figure B-5. SEM/FIB cross section of sample IBS 300 at 500 µN normal loads. A) 10 cycle. B) 30 cycles.

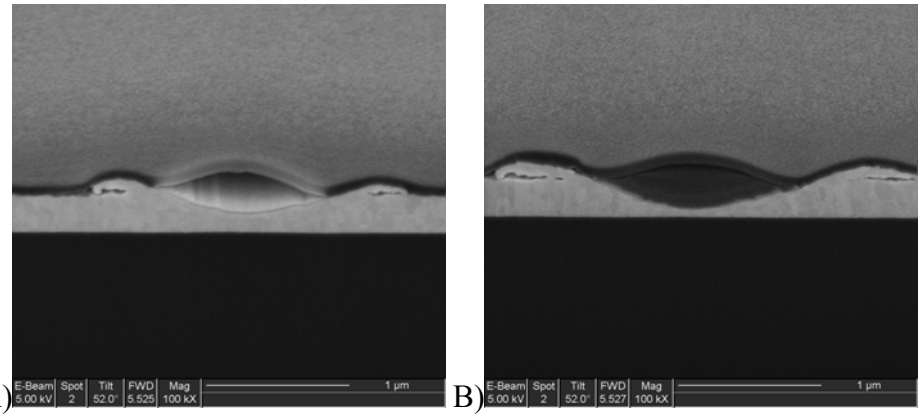

Figure B-6. SEM/FIB cross section of sample IBS 300 at 500 µN normal loads. A) 100 cycle. B) 300 cycle

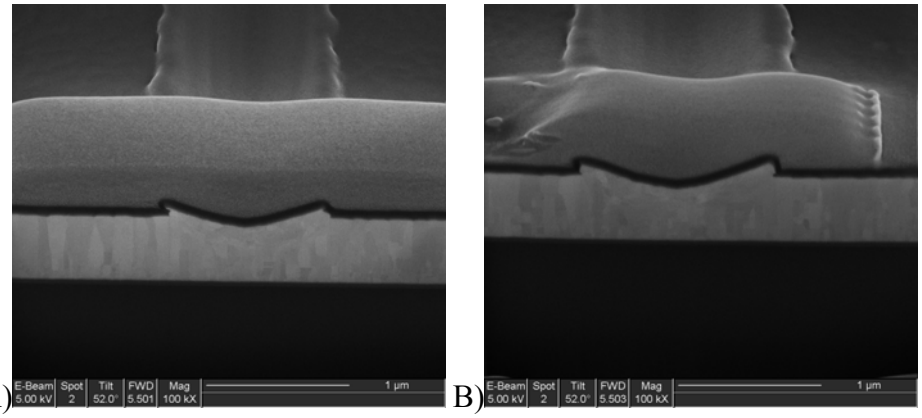

Figure B-7. SEM/FIB cross section of sample EBE 500 at 500 µN normal loads. A) 1 cycle. B) 3 cycle

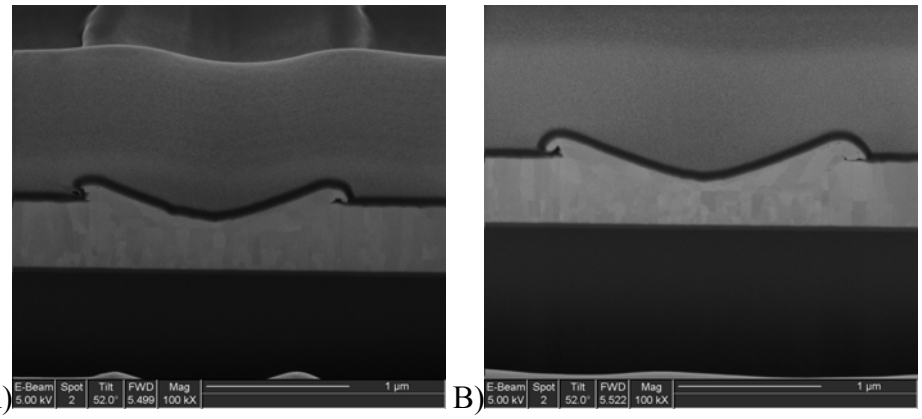

Figure B-8. SEM/FIB cross section of sample EBE 500 at 500 µN normal loads. A) 10 cycle. B) 30 cycle

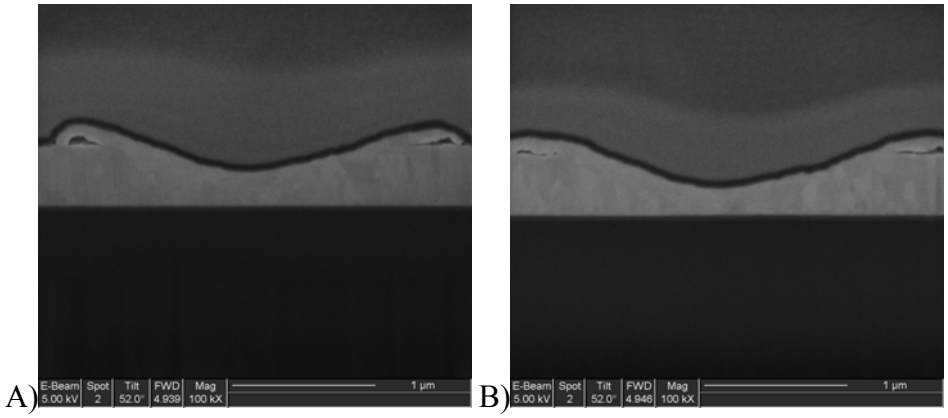

Figure B-9. SEM/FIB cross section of sample EBE 500 at 500 µN normal loads. A) 100 cycle. B) 300 cycle

LIST OF REFERENCES

1. Walraven, J. *Failure mechanisms in mems*. in *International Test Conference (ITC 2003)*. 2003. Charlotte, NC: IEEE Computer Society.

2. Saunders, S. R. J. and H. R. Vetters, *Standardisation of test methods for the mechanical properties of thin coatings.* Thin Solid Films, 1997. **299**(1-2): p. 82.

3. Rabinowicz, E., *Friction and Wear of Materials*. 2nd ed. 1995, New York: John Wiley & Sons, Inc. 315.

4. Bowden, F. P. and D. Tabor, *The Friction and Lubrication of Solids*. Vol. 1. 1950. 391.

5. Slade, P. G., *Electrical Contacts*. 1999, New York: Marcel Dekker. 1073.

6. Antler, M., *Processes of metal transfer and wear.* Wear, 1964. **7**: p. 181–204.

7. Antler, M., *Wear, friction, and electrical noise phenomenon in severe sliding systems.* ASLE Transactions, 1962. **5**: p. 297–307.

8. Antler, M., *Metal transfer and wedge forming mechanism.* Journal of Applied Physics, 1963. **34**(2): p. 438–439.

9. Cocks, M., *Interaction of sliding metal surface.* Journal of Applied Physics, 1962. **33**: p. 2152–2161.

10. Suh, N. P., *The delamination theory of wear.* Wear, 1973. **25**: p. 111–124.

11. Tian, H., N. Saka, and E. Rabinowicz, *Friction and failure of electroplated sliding contacts.* Wear, 1991. **142**(1): p. 57.

12. Bayer, R. G., *A general model for sliding wear in electrical contacts.* Wear, 1993. **162–164**(Part 2): p. 913.

13. Antler, M. and M. Feder, *Friction and wear of electrodeposited palladium contacts: Thin film lubrications with fluids and with gold.* IEEE Trans., 1986. **CHMT-9**(4): p. 485–491.

14. Jang, D.S. and D. E. Kim, *Tribological behavior of ultra-thin soft metallic deposits on hard substrates.* Wear, 1996. **196**(1-2): p. 171–193.

15. Sherbiney, M. A. and J. Halling, *Friction and wear of ion-plated soft metallic films.* Wear, 1977. **45**(2): p. 211–220.

16. Shimura, Y., T. Ito, Y. Taga, and K. Nakajima, *Frictional properties of sputtered tin film.* Wear, 1978. **49**(1): p. 179–193.

17. Spalvins, T. and B. Buzek, *Frictional and morphological characteristics of ion-plated soft metallic films.* Thin Solid Films, 1981. **84**(3): p. 267–272.

18. Bowers, R. C. and W. A. Zisman, *Pressure effects on the friction coefficient of thin-film solid lubricants.* Journal of Applied Physics, 1968. **39**(12): p. 5385–5395.

19. El-Shafei, T. E. S., R. D. Arnell, and J. Halling, *An experimental study of the hertzian contact of surfaces covered by soft metallic films.* ASLE Transactions, 1983. **26**(4): p. 481–486.

20. Finkin, E. F., *A theory for the effects of film thickness and normal load in the friction of thin films.* Transactions of the ASME Journal of Lubrication Technology, 1969(July): p. 551–556.

21. Schiffmann, K. I. and A. Hieke, *Analysis of microwear experiments on thin dlc coatings: Friction, wear and plastic deformation.* Wear, 2003. **254**(5-6): p. 565.

22. Dickrell, P. L., *Tribological behavior and gas-surface interactions of hydrogenated carbon films*. 2005: Gainesville, FL.

23. Fischer-Cripps, A. C., *Nanoindentation*, ed. F.F. Ling. 2002, New York: Springer-Verlag. 197.

24. Doerner, M. and W. D. Nix, *A method for interpreting the data from depth–sensing indentation instruments.* Journal Of Materials Research, 1986. **1**(4): p. 601.

25. Oliver, W. C. and G. M. Pharr, *An improved technique for determining hardness and elastic-modulus using load and displacement sensing indentation experiments.* Journal Of Materials Research, 1992. **7**(6): p. 1564–1583.

26. Sneddon, I. N., *The relation between load and penetration in the axisymmetric boussinesq problem for a punch of arbitrary profile.* International Journal of Engineering Science, 1965. **3**(1): p. 47.

27. Pharr, G. M., W. C. Oliver, and F. R. Brotzen, *On the generality of the relationship among contact stiffness, contact area, and elastic-modulus during indentation.* Journal Of Materials Research, 1992. **7**(3): p. 613–617.

28. Wyrobek, T. J., *Triboindenter User's Manual*, Minneapolis, MN: Hysitron Inc.

29. Stone, D. S., K. B. Yoder, and W. D. Sproul, *Hardness and elastic modulus of tin based on continuous indentation technique and new correlation.* Journal of Vacuum Science and Technology A, 1991. **9**(4): p. 2543–2547.

30. Joslin, D. L. and W. C. Oliver, *A new method for analyzing data from continuous depth-sensing microindentation tests.* Journal Of Materials Research, 1990. **5**(1): p. 123–126.

31. Saha, R. and W. Nix, *Effects of the substrate on the determination of thin film mechanical properties by nanoindentation.* Acta Materialia, 2002. **50**(1): p. 23–38.

32. Saha, R. and W. D. Nix, *Soft films on hard substrates -- nanoindentation of tungsten films on sapphire substrates.* Materials Science and Engineering A, 2001. **319–321**: p. 898.

33. Yoder, K., D. Stone, R. Hoffman, and J. Lin, *Elastic rebound between an indenter and a layered specimen: Part ii. Using contact stiffness to help ensure reliability of nanoindentation measurements.* Journal Of Materials Research, 1998. **13**(11): p. 3214–3220.

34. Reiss, G., J. Vancea, H. Wittmann, J. Zweck, and H. Hoffmann, *Scanning tunneling microscopy on rough surfaces: Tip-shape-limited resolution.* Journal of Applied Physics, 1990. **67**(3): p. 1156–1159.

35. Villarrubia, J. S., *Algorithms for scanned probe microscope image simulation, surface reconstruction, and tip estimation.* Journal of Research of the National Insititute of Standards and Technology, 1997. **102**(4): p. 425–454.

36. Xu, S. and M. F. Arnsdorf, *Calibration of the scanning (atomic) force microscope with gold particles.* Journal of Microscopy, 1994. **173**: p. 199.

37. Dieter, G. E., *Mechanical Metallurgy*. 1986, New York: McGraw-Hill.

38. Hertzberg, R. W., *Deformation and Fracture Mechanics of Engineering Materials*. 1996, New York: J. Wiley & Sons.

39. McSkimin, H. J. and P. Andreatch, Jr., *Elastic moduli of diamond as a function of pressure and temperature.* Journal of Applied Physics, 1972. **43**(7): p. 2944.

40. Cullity, B. D., *Elements of X-ray Diffraction*. 2nd. ed. 1959, Reading, MA: Addison-Wesley Publishing Company, Inc.

41. Brandes, E. A. and G. B. Brook, eds. *Smithell's Metals Reference Book*. 7th ed. 1998, Butterworth-Heinemann: Oxford.

42. Patterson, A. L., *The scherrer formula for x-ray particle size determination.* Physical Review, 1939. **56**: p. 978–982.

43. Williams, J. S., Y. Chen, J. Wong-Leung, A. Kerr, and M. V. Swain, *Ultra-micro-indentation of silicon and compound semiconductors with spherical indenters.* Journal Of Materials Research, 1999. **14**(6): p. 2338–2343.

44. Kelly, A., *Strong Solids*. 1966, Oxford: Oxford University Press.

45. Conrad, H. and K. Jung, *Effect of grain size from mm to nm on the flow stress and plastic deformation kinetics of au at low homologous temperatures.* Materials Science and Engineering: A, 2005. **406**(1-2): p. 78.

46. Nye, J. F., *Physical Properties of Crystals*. 1998, Oxford: Claredon Press.

47. Hebbache, M., *Nanoindentation: Depth dependence of silicon hardness studied within contact theory.* Physical Review B, 2003. **68**(12).

48. Phaneuf, M. W., *Applications of focused ion beam microscopy to materials science specimens.* 1999. **30**(3): p. 277.

49. Reyntjens, S. and C. Kubel, *Scanning/transmission electron microscopy and dual-beam sample preparation for the analysis of crystalline materials.* Proceedings of the 14th International Conference on Crystal Growth and the 12th International Conference on Vapor Growth and Epitaxy, 2005. **275**(1-2): p. e1849.

50. Uchic, M. D., M. A. Groeber, D. M. Dimiduk, and J. P. Simmons, *3d microstructural characterization of nickel superalloys via serial-sectioning using a dual beam fib-sem.* **In Press, Corrected Proof**.

51. Barrett, C. S. and T. B. Massalski, *Structure of Metals*. 3rd ed. 1966, New York: McGraw-Hill.

52. Davis, J. R., P. Allen, S. R. Lampman, and T. B. Zorc, eds. *Asm Handbook Volume 2, Properties and Selection: Nonferrous Alloys and Special-Purpose Materials*. 1998, ASM-International: Materials Park, OH.

BIOGRAPHICAL SKETCH

Gerald Bourne graduated high school in 1982 and worked in the automotive parts industry until 1986. He then began an entry level position in a serigraphic textile company. He learned the trade and opened his own company in 1988. By 1990, competition with foreign manufacturers lead to declining profits and caused him to seek other avenues. He joined a small service company and helped them to expand to a nationwide parts and service supplier. In 1992, he met Wanda Hix and fell in love. They married in the spring of 1993, and their daughter, Gabrielle was born in November. Wanda had the opportunity for a new position in 1995, so they moved to Gainesville in the Fall. Gerald went to Santa Fe Community College and completed his associate's degree in 1996. In 1997, he transferred to the University of Florida. He completed his bachelor's degree in 1999. He accepted the University of Florida Alumni F ellowship in 1999 and completed his master's degree in 2001. He worked at the Major Analytica Instrumentation Center throughout his graduate career as a teaching assistant, microscope technician and class lecturer.